

ANALYSIS, MODELING AND SIMULATION OF RING RESONATORS AND  
THEIR APPLICATIONS TO FILTERS AND OSCILLATORS

A Dissertation

by

LUNG-HWA HSIEH

Submitted to the Office of Graduate Studies of  
Texas A&M University  
in partial fulfillment of the requirements for the degree of

DOCTOR OF PHILOSOPHY

May 2004

Major Subject: Electrical Engineering

ANALYSIS, MODELING AND SIMULATION OF RING RESONATORS AND  
THEIR APPLICATIONS TO FILTERS AND OSCILLATORS

A Dissertation

by

LUNG-HWA HSIEH

Submitted to Texas A&M University  
in partial fulfillment of the requirements  
for the degree of

DOCTOR OF PHILOSOPHY

Approved as to style and content by:

---

Kai Chang  
(Chair of Committee)

---

Jyh-Charn Liu  
(Member)

---

Robert D. Nevels  
(Member)

---

Chin B. Su  
(Member)

---

Chanan Singh  
(Head of Department)

May 2004

Major Subject: Electrical Engineering

## ABSTRACT

Analysis, Modeling and Simulation of Ring Resonators and Their Applications to Filters and Oscillators. (May 2004)

Lung-Hwa Hsieh, B.S., Chung Yuan Christian University;  
M.S., National Taiwan University of Science and Technology  
Chair of Advisory Committee: Dr. Kai Chang

Microstrip ring circuits have been extensively studied in the past three decades. A magnetic-wall model has been commonly used to analyze these circuits. Unlike the conventional magnetic-wall model, a simple transmission-line model, unaffected by boundary conditions, is developed to calculate the frequency modes of ring resonators of any general shape such as annular, square, or meander ring resonators. The new model can be used to extract equivalent lumped element circuits and unloaded  $Q$ s for both closed- and open-loop ring resonators.

Several new bandpass filter structures, such as enhanced coupling, slow-wave, asymmetric-fed with two transmission zeros, and orthogonal direct-fed, have been proposed. These new proposed filters provide advantages of compact size, low insertion loss, and high selectivity. Also, an analytical technique is used to analyze the performance of the filters. The measured results show good agreement with the simulated results.

A compact elliptic-function lowpass filter using microstrip stepped impedance hairpin resonators has been developed. The prototype filters are synthesized from the equivalent circuit model using available element-value tables. The filters are evaluated by experiment and simulation with good agreement. This simple equivalent circuit model provides a useful method to design and understand this type of filters and other relative circuits.

Finally, a tunable feedback ring resonator oscillator using a voltage controlled piezoelectric transducer is introduced. The new oscillator is constructed by a ring

resonator using a pair of orthogonal feed lines as a feedback structure. The ring resonator with two orthogonal feed lines can suppress odd modes and operate at even modes. A voltage controlled piezoelectric transducer is used to vary the resonant frequency of the ring resonator. This tuned oscillator operating at high oscillation frequency can be used in many wireless and sensor systems.

To my family and to the memory of my father

## ACKNOWLEDGMENTS

Thanks to the Lord for the blessing you have given me. Your great mercy and love are always with me. Thank you for giving me the wisdom and the strength to face every challenge in my life, especially for helping me to study in the US.

I would like to express my sincere appreciation to my dear advisor Dr. Kai Chang for his guidance and financial sponsorship with regards to my graduate studies and research. I also give my sincere appreciation to Dr. Robert Nevels, Dr. Chin Su, and Dr. Jyh-Charn Liu for serving as committee members for my Ph. D. pursuing.

I would also like to thank Mr. Chunlei Wang and Mr. Min-Yi Li at Texas A&M University for their professional technical assistance. I would like to thank my good friend, Mr. Chris Rodenbeck, for helping me understand American culture and for correcting my English, including revising papers and providing useful suggestions. In addition, I would like to thank all the members of the Electromagnetic and Microwave Lab who befriended me at TAMU.

I would like to express thanks to the Rogers Corporation, Zeland Company, Boeing Company, and U. S. Air Force for support my research. My appreciation also to Dr. Chin B. Su for support in equipment.

I would like to thank all of my dear friends, Nikki Chou, Eric Wu, Peter Cheng, Jen Lee, Jerry Lin, Timothy Yu, Pastor Lin, Pastor Wei, Pastor Chen, and my church brothers and sisters in U. S. and Taiwan, for their wonderful support. Finally, I would like to give thanks to my wife, Nairong Wang, mother, sisters and brother for their patience, encouragement, and warm comfort during my graduate studies.

## TABLE OF CONTENTS

	Page
ABSTRACT .....	iii
DEDICATION .....	v
ACKNOWLEDGMENTS .....	vi
TABLE OF CONTENTS .....	vii
LIST OF FIGURES.....	x
LIST OF TABLES .....	xv
CHAPTER	
I INTRODUCTION .....	1
A. Objective .....	1
B. Organization of This Dissertation .....	3
II SIMPLE ANALYSIS OF THE FREQUENCY MODES FOR MICROSTRIP RING RESONATORS .....	5
A. Introduction .....	5
B. Frequency Modes for Ring Resonators .....	6
C. An Error in Literature for One-Port Ring Circuit .....	9
D. Dual Mode .....	12
E. Conclusions .....	16
III EQUIVALENT LUMPED ELEMENTS $G$ , $L$ , $C$ AND UNLOADED $Q_s$ OF CLOSED- AND OPEN-LOOP RING RESONATORS .....	17
A. Introduction .....	17
B. Equivalent Lumped Elements and Unloaded $Q_s$ for Closed and Open-Loop Microstrip Ring Resonators .....	18
1) Closed-Loop Ring Resonators .....	18
2) Open-Loop Ring Resonators .....	24
C. Calculated and Measured Unloaded $Q_s$ and Equivalent Lumped Elements for Ring Resonators .....	28
1) Calculated Method .....	28
2) Measured Method .....	31
D. Calculated and Experimental Results.....	32
E. Conclusions .....	35
IV DUAL-MODE BANDPASS FILTERS USING RING RESONATORS WITH ENHANCED-COUPPLING TUNING STUBS .....	36
A. Introduction .....	36

CHAPTER	Page
B. Dual-mode Bandpass Filter Using a Single Ring Resonator .....	37
C. Dual-mode Bandpass Filter Using Multiple Cascaded Ring Resonators .....	45
1) Dual-mode Bandpass Filter Using Two Cascaded Ring Resonators .....	45
2) Dual-mode Bandpass Filter Using Three Cascaded Ring Resonators .....	48
D. Conclusions .....	50
V SLOW-WAVE BANDPASS FILTERS USING RING OR STEPPED IMPEDANCE HAIRPIN RESONATORS .....	51
A. Introduction .....	51
B. Analysis of the Slow-Wave Periodic Structure .....	52
C. Slow-Wave Bandpass Filters Using Square Ring Resonators .....	55
D. Slow-Wave Bandpass Filters Using Stepped Impedance Hairpin Resonators .....	61
E. Conclusions .....	64
VI TUNABLE MICROSTRIP BANDPASS FILTERS WITH TWO TRANSMISSION ZEROS .....	66
A. Introduction .....	66
B. Analysis of Filters with Asymmetric and Symmetric Tapping Feed Lines .....	67
C. Compact Size Filters .....	72
1) Filters Using Two Open-Loop Ring Resonators .....	72
2) Filters Using Four Cascaded Open-Loop Ring Resonators .....	76
3) Filters Tuning by a Piezoelectric Transducer .....	77
D. Conclusions .....	79
VII COMPACT, LOW INSERTION LOSS, SHARP REJECTION AND WIDEBAND MICROSTRIP BANDPASS FILTERS .....	81
A. Introduction .....	81
B. Bandstop and Bandpass Filters Using a Single Ring with One or Two Tuning Stubs .....	82
1) Bandstop Characteristic .....	82
2) One Tuning Stub .....	85
3) Two Tuning Stubs .....	88
C. Wideband Microstrip Bandpass Filters with Dual Mode Effects .....	90
D. Conclusions .....	96
VIII COMPACT ELLIPTIC-FUNCTION LOWPASS FILTERS .....	97
A. Introduction .....	97
B. Equivalent Circuit Model for the Step Impedance Hairpin .....	98



CHAPTER	Page
C. Compact Elliptic-Function Lowpass Filters .....	102
1) Lowpass Filter Using One Stepped Impedance Hairpin Resonator .....	102
2) Lowpass Filter Using Multiple Cascaded Stepped Impedance Hairpin Resonators .....	107
3) Broad Stopband Lowpass Filters .....	111
D. Conclusions .....	113
IX PIEZOELECTRIC TRANSDUCER TUNED FEEDBACK MICROSTRIP RING RESONATOR OSCILLATORS .....	115
A. Introduction .....	115
B. Ring Resonator with Orthogonal Feed Lines .....	116
C. Feedback Ring Resonator Oscillators .....	119
D. Tunable Feedback Ring Resonator Oscillators Using a Piezoelectric Transducer .....	123
E. Conclusions .....	126
X SUMMARY .....	127
REFERENCES .....	129
APPENDIX I .....	140
APPENDIX II .....	141
VITA .....	142

## LIST OF FIGURES

FIGURE	Page
1 The configurations of one-port (a) square and (b) annular ring resonators. ....	6
2 Standing waves on each section of the square ring resonator. ....	9
3 Simulated electrical current standing waves for (a) one- and (b) two-port ring resonators at $n = 1$ mode. ....	10
4 Configurations of one-port ring resonators for mean circumferences of (a) $\lambda_g / 2$ and (b) $\lambda_g$ . ....	11
5 Measured results for one-port ring resonators with modes $n = 1$ to 5. ....	12
6 The simulated electrical currents of the square ring resonator with a perturbed stub at $\Phi = 45^\circ$ for (a) the low splitting resonant frequency of $n = 1$ mode (b) high splitting resonant frequency of mode $n = 1$ , and (c) mode $n = 2$ . ....	14
7 The measured results for modes $n = 1$ and 2 of the square ring resonator with a perturbed stub at $\Phi = 45^\circ$ . ....	15
8 A closed-loop microstrip ring resonator. ....	19
9 The input impedance of (a) one-port network and (b) two-port network of the closed-loop ring resonator. ....	20
10 Equivalent elements $G_c$ , $C_c$ , and $L_c$ of the closed-loop ring resonator. ....	23
11 Transmission-line model of the closed-loop square ring resonator. ....	24
12 Transmission-line model of (a) the open-loop ring resonator and (b) its equivalent elements $G_o$ , $L_o$ , and $C_o$ . ....	25
13 Transmission-line model of the U-shaped open-loop ring resonator. ....	27
14 Layouts of the (a) annular (b) square (c) open-loop with the curvature effect and (d) U-shaped open-loop ring resonators. ....	33
15 New bandpass filter (a) layout and (b) L-shape coupling arm. ....	38
16 Measured (a) $S_{21}$ and (b) $S_{11}$ by adjusting the length of the tuning stub $L$ with a fixed gap size ( $s = 0.8$ mm). ....	39
17 Measured (a) $S_{21}$ and (b) $S_{11}$ by varying the gap size $s$ with a fixed length of the tuning stubs ( $L = 13.5$ mm). ....	40
18 A square ring resonator for the unloaded $Q$ measurement. ....	41

FIGURE	Page
19 Simulate and measured results for the case of $L = 13.5$ mm and $s = 0.8$ mm. ....	44
20 Layout of the filter using two resonators with $L$ -shape coupling arms. ....	45
21 Back-to-back $L$ -shape resonator (a) layout and (b) equivalent circuit. The lengths $L_a$ and $L_b$ include the open end effects. ....	46
22. Measured $S_{21}$ for the back-to-back $L$ -shape resonator. ....	47
23 Simulated and measured results for the filter using two resonators with $L$ -shape coupling arms. ....	48
24 Layout of the filter using three resonators with $L$ -shape coupling arms. ....	49
25 Simulated and measured results for the filter using three resonators with $L$ -shape coupling arms. ....	49
26 Slow-wave periodic structure (a) conventional type and (b) with loading $Z_L$ at open end. ....	53
27 Lossless (a) parallel and (b) series resonant circuits. ....	54
28 Slow-wave bandpass filter using one ring resonator with one coupling gap (a) layout and (b) simplified equivalent circuit. ....	55
29 Line-to-ring coupling structure (a) top view (b) side view and (c) equivalent circuit. ....	56
30 Variation in input impedance $ Z_{in3} $ for different lengths of $l_b$ showing (a) parallel and series resonances and (b) an expanded view for the series resonances. ....	58
31 Measured and calculated frequency response for the slow-wave bandpass filter using one square ring resonator. ....	59
32 Slow-wave bandpass filter using three ring resonators (a) layout and (b) simplified equivalent circuit. ....	60
33 Measured and calculated frequency response for slow-wave bandpass filter using three square ring resonators. ....	61
34 Slow-wave bandpass filter using one stepped impedance hairpin resonator (a) layout and (b) simplified equivalent circuit. ....	62
35 Slow-wave bandpass filter using six stepped impedance hairpin resonators (a) layout and (b) simplified equivalent circuit. ....	63
36 Measured and calculated frequency response for slow-wave bandpass filter using six stepped impedance hairpin resonators. ....	64

FIGURE	Page
37 Configuration of the filter using two hairpin resonators with asymmetric tapping feed lines. ....	68
38 Measured results for different tapping positions with coupling gap $s_1 = 0.35$ mm. ....	70
39 Configuration of the filter using two hairpin resonators with symmetric tapping feed lines. ....	71
40 Measured and calculated results for the filter using symmetric tapping feed lines with coupling gap $s_1 = 0.35$ mm. ....	72
41 Layout of the filter using two open-loop ring resonators with asymmetric tapping feed lines. ....	72
42 Measured results for different tapping positions with coupling gap $s_1 = 0.35$ mm. ....	74
43 Measured results of the open-loop ring resonators for the case of tapping positions of $l_1 = 11.24$ mm and $l_2 = 17.61$ mm. ....	75
44 Configuration of the filter using four cascaded open-loop ring resonators. ....	76
45 Measured and simulated results of the filter using four cascaded open-loop ring resonators. ....	77
46 Configuration of the tunable bandpass filter (a) top view and (b) 3D view. ....	78
47 Measured results of the tunable bandpass filter with a perturber of $\epsilon_r = 10.8$ and $h = 50$ mil. ....	79
48 A ring resonator using direct-connected orthogonal feeders. ....	82
49 Simulated electric current at the resonant frequency for the ring and open stub bandstop circuits. ....	83
50 Simulated results for the bandstop filters. ....	83
51 Equivalent circuit of the ring using direct-connected orthogonal feed lines. ....	84
52 Calculated and measured results of the ring using direct-connected orthogonal feed lines. ....	85
53 Configuration of the ring with a tuning stub of $l_t = 5.03$ mm and $w_2 = 0.3$ mm at $\Phi = 90^\circ$ or $0^\circ$ . ....	86
54 Equivalent circuit of the ring using a tuning stub at $\Phi = 90^\circ$ . ....	87

FIGURE	Page
55	Calculated results of the ring with various lengths of the tuning stub at $\Phi = 90^\circ$ . ..... 87
56	Calculated and measured results of the ring using a tuning stub at $\Phi = 90^\circ$ . ..... 88
57	Layout of the ring using two tuning stubs at $\Phi = 90^\circ$ and $0^\circ$ . ..... 88
58	Calculated results of the ring with various lengths of the tuning stub at $\Phi = 90^\circ$ and $0^\circ$ . ..... 89
59	Calculated and measured results of the ring with two tuning stubs of $l_t = \lambda g/4 = 5.026$ mm at $\Phi = 90^\circ$ and $0^\circ$ . ..... 90
60	The dual-mode filter (a) layout, (b) equivalence of the perturbed stub and (c) overall equivalent circuit. .... 91
61	Calculated and measured results of the dual-mode ring filter. The crosses (x) show the two transmission zero locations. .... 93
62	Configuration of the cascaded dual-mode ring resonator. .... 94
63	Calculated and measured results of the cascaded dual-mode ring resonator filter. .... 95
64	Group delay of the cascaded dual-mode ring resonator filter. .... 95
65	A stepped impedance hairpin resonator. .... 98
66	Equivalent circuit of (a) single transmission line, (b) symmetric coupled lines, and (c) stepped impedance hairpin resonator. .... 99
67	The lowpass filter using one hairpin resonator (a) layout and (b) equivalent circuit. .... 102
68	Simulated frequency responses of the filter using one hairpin resonator. .... 104
69	Measured and simulated (a) frequency response and (b) $S_{21}$ within the 3-dB bandwidth for the filter using one hairpin resonator. .... 105
70	The lowpass filter using cascaded hairpin resonators (a) layout, (b) asymmetric coupled lines, and (c) equivalent circuit of the asymmetric coupled lines. .... 106
71	Equivalent circuit of the lowpass filter using cascaded hairpin resonators. .... 107
72	Simulated frequency responses of the filter using four cascaded hairpin resonators. .... 109

FIGURE	Page
73 Measured and simulated (a) frequency response and (b) $S_{21}$ within the 3-dB bandwidth for the filter using cascaded hairpin resonators. ....	110
74 Layout of the lowpass filter with additional attenuation poles. ....	112
75 Measured and simulated (a) frequency response and (b) $S_{21}$ within the 3-dB bandwidth for the filter with additional attenuation poles. ....	113
76 Configuration of the ring resonator fed by two orthogonal feed lines. ....	117
77 Configuration of the ring resonator using enhanced orthogonal feed lines. ....	118
78 Simulated and measured results for the ring resonator using enhanced orthogonal feed lines. ....	118
79 A feedback ring resonator oscillator. ....	119
80 Two-port negative-resistance oscillator (a) layout and (b) measured and simulated results. ....	120
81 Measured DC-to-RF efficiency and oscillation frequency versus $V_{gs}$ with $V_{ds} = 1.5$ V. ....	121
82 Measured DC-to-RF efficiency and oscillation frequency versus $V_{ds}$ with $V_{gs} = -0.4$ V. ....	122
83 Output power for the feedback ring resonator oscillator operated at the second harmonic of the ring resonator. ....	123
84 Configuration of the tunable oscillator using a PET (a) top view and (b) 3D view. ....	124
85 Measured tuning range of 510 MHz for the tunable oscillator using a PET. ....	125
86 Tuning oscillation frequencies and output power levels versus PET tuning voltages. ....	125

## LIST OF TABLES

TABLE	Page
I Unloaded $Q$ s for the parameters: $\epsilon_r = 2.33$ , $h = 10$ mil, $t = 0.7$ mil, $w = 0.567$ mm for a 60-ohms line, $\Delta = 1.397\mu\text{m}$ and $\lambda_g = 108.398$ mm. ....	33
II Equivalent elements for the parameters: $\epsilon_r = 2.33$ , $h = 10$ mil, $t = 0.7$ mil, $w = 0.567$ mm for a 60-ohms line, $\Delta = 1.397\mu\text{m}$ and $\lambda_g = 108.398\text{mm}$ . ....	34
III Unloaded $Q$ s for the parameters: $\epsilon_r = 10.2$ , $h = 10$ mil, $t = 0.7$ mil, $w = 0.589$ mm for a 30-ohms line, $\Delta = 1.397\mu\text{m}$ and $\lambda_g = 55.295$ mm. ....	34
IV Equivalent elements for the parameters: $\epsilon_r = 10.2$ , $h = 10$ mil, $t = 0.7$ mil, $w = 0.589$ mm for a 30-ohms line, $\Delta = 1.397\mu\text{m}$ and $\lambda_g = 55.295$ mm. ....	35
V Single mode ring resonator. ....	42
VI Dual mode ring resonator. ....	43
VII Filter performance. ....	50
VIII Measured and calculated results of the hairpin resonators for different tapping positions. ....	70
IX Measured results of the open-loop ring resonators for different tapping positions. ....	73
X L-C values of the filter using one hairpin resonator. ....	103
XI L-C values of the filter using four hairpin resonators. ....	108

## CHAPTER I

### INTRODUCTION

#### *A. Objective*

The objectives of this dissertation are to introduce the analyses and modelings of the ring resonators and to apply them to the applications of filters and oscillators.

For the past three decades, the microstrip ring resonator has been widely utilized to measure the effective dielectric constant dispersion, and discontinuity parameters and to determine optimum substrate thickness [1-4]. Beyond measurement applications, the microstrip ring resonator has also been used in filters, oscillators, mixers, and antennas [5] because of its advantages of compact size, easy fabrication, and narrow passband bandwidth. Recently, interesting compact filters using microstrip ring or loop resonators for cellular and other communication systems were reported [6-8].

The field theory for the ring resonator was first introduced by Wolff and Knoppik [2]. They used the magnetic-wall model to describe the curvature effect on the resonant frequency of the ring resonator. Furthermore, based on this model, Wu and Rosenbaum found the mode chart [9] or frequency modes [5] of the ring resonator obtained from the eigen-function of Maxwell's equations with the boundary conditions of the ring. Specifically, they found the mode frequencies satisfying  $2\pi r = n\lambda_g$ , with  $n = 1, 2, 3, \dots$ , where  $r$  is the mean radius of the ring resonator,  $n$  is the mode number and  $\lambda_g$  is the guided-wavelength. Although the mode chart of the magnetic wall model has been studied extensively, it provides only a limited description of the effects of the circuit parameters and dimensions [5]. A further study on a ring resonator using the transmission-line model was developed later [10]. The transmission-line model used a

---

This dissertation follows the style and format of *IEEE Transactions on Microwave Theory and Techniques*.



T-network in terms of equivalent impedances to analyze a ring circuit. However, this model showed a complex expression for the ring circuit. Another distributed-circuit model using cascaded transmission-line segments for a ring was reported [11]. The model can easily incorporate any discontinuities and solid-state devices along the ring. Although this model could predict the behavior of a ring resonator well, it could not provide a straightforward circuit view such as equivalent lumped elements  $G$ ,  $L$  and  $C$  for the ring circuit. On the other hand, so far, only the annular ring resonator has the theory derivation for its frequency modes. For the square or meander ring resonator [5,12], it is difficult to find the frequency modes using magnetic-wall model because of its complex boundary conditions. Thus, in [5], the square ring resonator was treated as a special case of an annular ring resonator, but it is not a rigorous approach. Also, the magnetic-wall model cannot be used to explain the dual-mode behavior for the ring resonator with complex boundary conditions.

Due to the sharp cut-off frequency response, most of the established bandpass filters were built by dual-mode ring resonators, which were originally introduced by Wolff [13]. The dual-mode consists of two degenerate modes, which are excited by asymmetrical feed lines, added notches, or stubs on the ring resonator [5,13,14,15,16]. The coupling between the two degenerate modes is used to construct a bandpass filter. By proper arrangement of feed lines, notches, or stubs, the filter can achieve Chebyshev, elliptic or quasi-elliptic characteristics with sharp rejection. Recently, one interesting excitation method using asymmetrical feed lines with lumped capacitors at input and output ports to design a bandpass filter was proposed [17]. A conventional end-to-side coupling ring resonator suffers from high insertion loss, which is due to circuit's conductor, dielectric, radiation losses and an inadequate coupling between feeders and the ring resonator. The size of the coupling gap between ring resonator and feed lines affects the strength of coupling and the resonant frequency [5]. For instance, for a narrow coupling gap size, the ring resonator has a tight coupling and can provide a low insertion loss but the resonant frequency will be influenced greatly and for a wide gap size, the resonator has a high insertion loss and the resonant frequency is slightly

affected. In order to improve insertion loss, some structures and active filters have been reported [18-23]. In this dissertation, several new structures have been developed to enhance the performance of ring resonators and filters. These include ring resonators using enhanced L-shape coupling, slow-wave filters, direct-connected ring resonators with orthogonal feed lines, ... In addition, some novel configurations have been demonstrated to incorporate active devices incorporated into the ring resonator to provide gain to compensate for the loss and to build oscillators [19-20].

### *B. Organization of This Dissertation*

This dissertation is organized in ten Chapters. Chapter II presents the frequency modes of the microstrip ring resonators of any general shape by using a simple transmission line analysis [24]. Also, a literature error has been found and discussed. Chapter III introduces an equivalent lumped elements  $G$ ,  $L$ ,  $C$  and unloaded  $Q$ s of closed- and open-loop ring resonators that provides an easy method to design ring circuits [25]. In Chapter IV, a new bandpass filter is shown. The filter using ring resonators with enhanced-coupling tuning stubs has high selectivity and low insertion loss characteristics. Chapter V shows a new slow-wave bandpass filter with a low insertion loss that constructed by a transmission line with periodically loaded ring or stepped impedance hairpin resonators. Chapter VI discusses the filter with two transmission zeros that gives a sharp cut-off frequency response next to the passband. In addition, a piezoelectric transducer is used to tune the passband of the filter. The characteristics of the PET [26,27] are also described in this chapter [28]. In Chapter VII, a compact, low insertion loss, sharp rejection and wideband microstrip bandpass filter is presented [29,30]. The filter is designed for satellite communication applications, which require wide passband, sharp stopband rejection and wide stopband. Chapter VIII shows a compact elliptic-function lowpass filter microstrip stepped impedance hairpin resonators [31,32]. This compact lowpass filter with low insertion loss and a wide stopband is useful in many wireless communication systems. Chapter IX presents a high

efficiency piezoelectric transducer tuned feedback microstrip ring resonator oscillator operating at high resonant frequencies [33]. The last chapter summaries all studies.

## CHAPTER II

SIMPLE ANALYSIS OF THE FREQUENCY MODES FOR MICROSTRIP  
RING RESONATORS\**A. Introduction*

The field theory for the ring resonator was first introduced by Wolff and Knoppik [2]. They used the magnetic-wall model to describe the curvature effect on the resonant frequency of the ring resonator. Furthermore, based on this model, Wu and Rosenbaum found the mode chart [9] or frequency modes [10] of the ring resonator obtained from the eigen-function of Maxwell's equations with the boundary conditions of the ring. Specifically, they found the mode frequencies satisfying  $2\pi r = n\lambda_g$ , with  $n = 1, 2, 3, \dots$ , where  $r$  is the mean radius of the ring resonator,  $n$  is the mode number and  $\lambda_g$  is the guided-wavelength. So far, only the annular ring resonator has the theory derivation for its frequency modes. For the square ring resonator, it is difficult to use the magnetic-wall model to obtain the frequency modes of the square ring resonator because of its complex boundary conditions. Thus, in [10], the square ring resonator with complex boundary conditions was treated as a special case of an annular ring resonator, but it is not a rigorous approach. Also, the magnetic-wall model does not explain the dual-mode behavior very well, especially for ring resonators with complex boundary conditions.

In this chapter, a simple transmission-line model is used to calculate frequency modes of ring resonators of any general shape. Also, it points out a literature error for the frequency modes of the one-port ring resonator. Moreover, it provides a better explanation for dual-mode behavior than the magnetic-wall model.

---

\*Reprinted with permission from "Simple analysis of the frequency modes for microstrip ring resonators of any general shape and the correction of an error in literature" by Lung-Hwa Hsieh and Kai Chang, 2003. *Microwave and Optical Technology Letters*, vol. 3, pp. 209-213. © 2004 by the Wiley.

### B. Frequency Modes for Ring Resonators

Fig. 1 shows the configurations of the one-port square and annular ring resonators. For a ring of any general shape, the total length  $l$  may be divided into  $l_1$  and  $l_2$  sections.

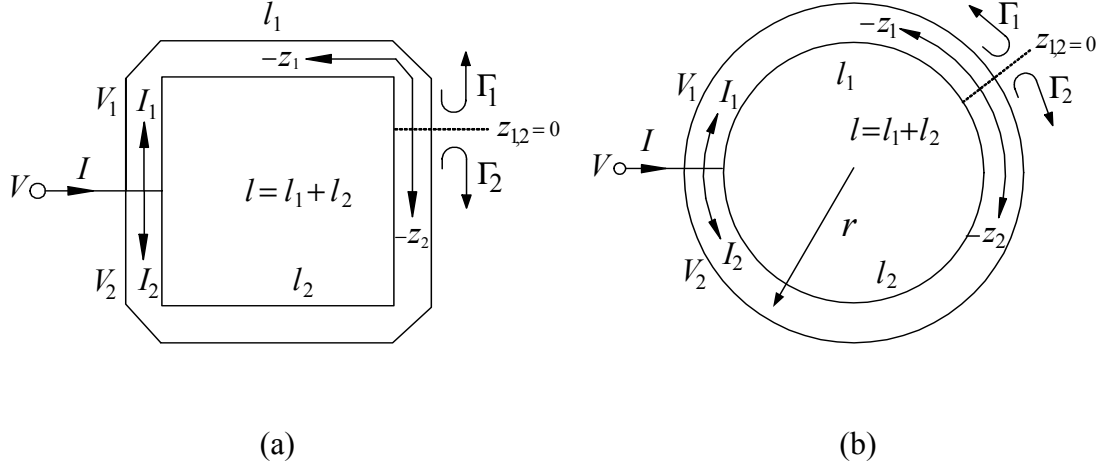


Fig. 1. The configurations of one-port (a) square and (b) annular ring resonators.

In the case of the square ring, each section is considered to be a transmission line.  $z_1$  and  $z_2$  are the coordinates corresponding to sections  $l_1$  and  $l_2$ , respectively. The ring is fed by the source voltage  $V$  at somewhere with  $z_{1,2} < 0$ . The positions of the zero point of  $z_{1,2}$  and the voltage  $V$  are arbitrarily chosen on the ring. For a lossless transmission line, the voltages and currents for the two sections are given as follows:

$$V_{1,2}(z_{1,2}) = V_o^+ (e^{-j\beta z_{1,2}} + \Gamma_{1,2}(0) e^{j\beta z_{1,2}}) \quad (1a)$$

$$I_{1,2}(z_{1,2}) = \frac{V_o^+}{Z_o} (e^{-j\beta z_{1,2}} - \Gamma_{1,2}(0) e^{j\beta z_{1,2}}) \quad (1b)$$

where  $V_o^+ e^{-j\beta z_{1,2}}$  is the incident wave propagating in the  $+z_{1,2}$  direction,  $V_o^+ \Gamma_{1,2}(0) e^{j\beta z_{1,2}}$  is the reflected wave propagating in the  $-z_{1,2}$  direction,  $\beta$  is the propagation constant,

$\Gamma_{1,2}(0)$  is the reflection coefficient at  $z_{1,2} = 0$ , and  $z_o$  is the characteristic impedance of the ring.

When a resonance occurs, standing waves set up on the ring. The shortest length of the ring resonator that supports these standing waves can be obtained from the positions of the maximum values of these standing waves. These positions can be calculated from the derivatives of the voltages and currents in (1). The derivatives of the voltages are

$$\frac{\partial V_{1,2}(z_{1,2})}{\partial z_{1,2}} = -j\beta V_o^+ (e^{-j\beta z_{1,2}} - \Gamma_{1,2}(0) e^{j\beta z_{1,2}}). \quad (2)$$

Letting  $\left. \frac{\partial V_{1,2}(z_{1,2})}{\partial z_{1,2}} \right|_{z_{1,2}=0} = 0$ , the reflection coefficients can be found as

$$\Gamma_{1,2}(0) = 1. \quad (3)$$

Substituting  $\Gamma_{1,2}(0) = 1$  into (1), the voltages and currents can be rewritten as

$$V_{1,2}(z_{1,2}) = 2V_o^+ \cos(\beta z_{1,2}) \quad (4a)$$

$$I_{1,2}(z_{1,2}) = -\frac{j2V_o^+}{Z_o} \sin(\beta z_{1,2}). \quad (4b)$$

Therefore, the absolute values of the maximum voltages on the ring can be found as

$$\left| V_{1,2}(z_{1,2}) \right|_{\max} = 2V_o^+ \text{ for } z_{1,2} = m \frac{\lambda_g}{2}, \quad m = 0, -1, -2, -3, \dots \quad (5)$$

In addition, the currents  $I_{1,2}$  at the positions of  $z_{1,2} = m \frac{\lambda_g}{2}$  are

$$I_{1,2}(z_{1,2}) \Big|_{z_{1,2} = m \frac{\lambda_g}{2}} = 0. \quad (6)$$

Also, the absolute values of the maximum currents can be found as

$$|I_{1,2}(z_{1,2})|_{\max} = \frac{2V_o^+}{Z_o} \text{ for } z_{1,2} = \frac{(2m-1)}{4} \lambda_g, \quad m = 0, -1, -2, -3, \dots \quad (7)$$

and the voltages  $V_{1,2}$  at the positions of  $z_{1,2} = \frac{(2m-1)}{4} \lambda_g$  are

$$V_{1,2}(z_{1,2}) \Big|_{z_{1,2} = \frac{(2m-1)}{4} \lambda_g} = 0. \quad (8)$$

Fig. 2 shows the absolute values of voltage and current standing waves on each section  $l_1$  and  $l_2$  of the square ring resonator. Inspecting Fig. 2, the standing waves repeat for multiples of  $\lambda_g/2$  on the each section of the ring. Thus, to support standing waves, the shortest length of each section on the ring has to be  $\lambda_g/2$ , which can be treated as the fundamental mode of the ring. For higher order modes,

$$l_{1,2} = n \frac{\lambda_g}{2} \text{ for } n = 1, 2, 3, \dots \quad (9)$$

where  $n$  is the mode number. Therefore, the total length of the square ring resonator is

$$l = l_1 + l_2 = n \lambda_g \quad (10)$$

or in terms of the annular ring resonator with a mean radius  $r$  as shown in Fig. 1(b),

$$l = n\lambda_g = 2\pi r. \quad (11)$$

Equation (10) shows a general expression for frequency modes and may be applied to any configuration of microstrip ring resonators including those shown in [11,6].

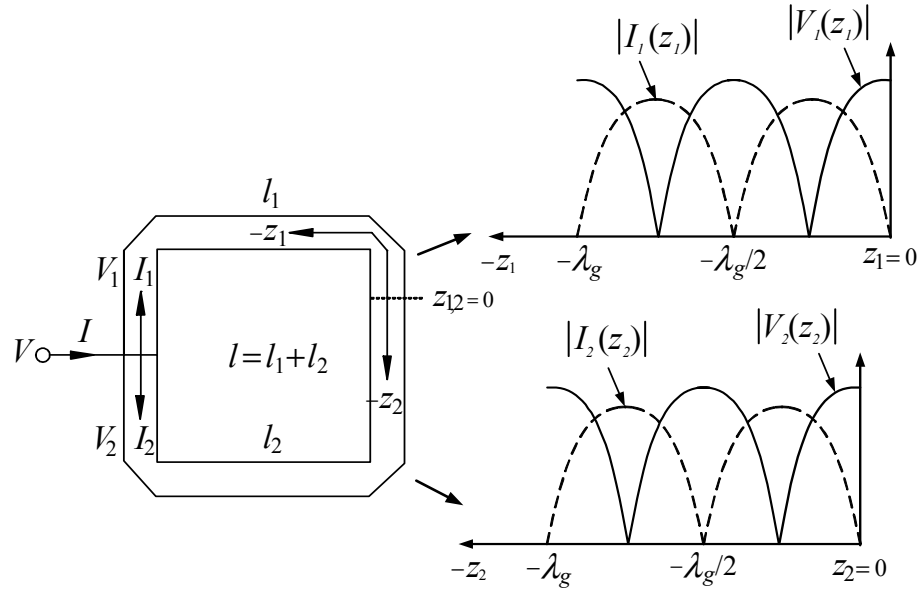


Fig. 2. Standing waves on each section of the square ring resonator.

### C. An Error in Literature for One-Port Ring Circuit

In [10,34], one- and two-port ring resonators show different frequency modes. For one-port ring resonator as shown in Fig. 3(a), the frequency modes are given as

$$2\pi r = n \frac{\lambda_g}{2}, \quad n = 1, 2, 3, \dots \quad (12a)$$

$$f_o = \frac{nc}{4\pi r \sqrt{\epsilon_{eff}}} \quad (12b)$$



where  $\epsilon_{eff}$  is the effective dielectric constant,  $f_o$  is the resonant frequencies, and  $c$  is the speed of light in free space.

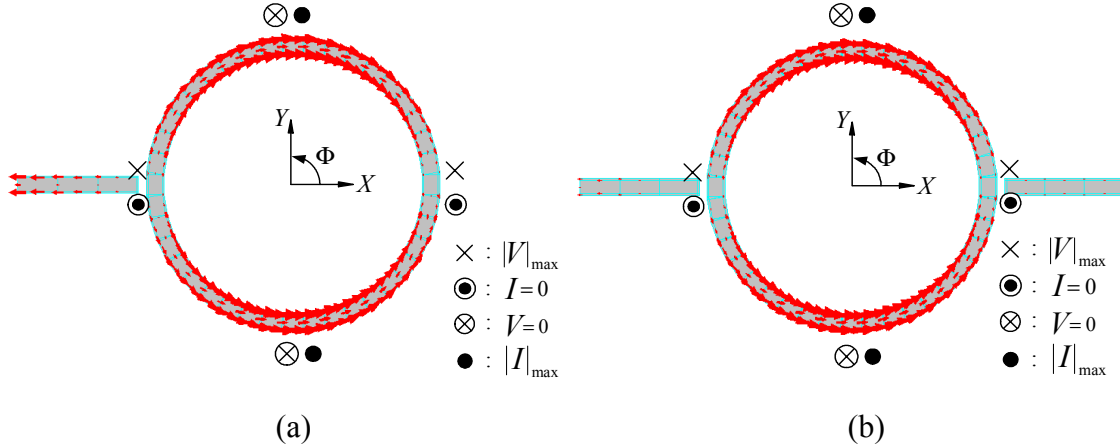


Fig. 3. Simulated electrical current standing waves for (a) one- and (b) two-port ring resonators at  $n = 1$  mode.

For the two-port ring resonator as shown in Fig. 3(b), the frequency modes are

$$2\pi r = n\lambda_g, \quad n = 1, 2, 3, \dots \quad (13a)$$

$$f_o = \frac{nc}{2\pi r \sqrt{\epsilon_{eff}}} \quad (13b)$$

However, in section *B*, the one-port ring resonator has the same frequency modes given in (11) as those of the two-port ring resonator given in (13a). The results can also be investigated by EM simulation performed by the IE3D electromagnetic simulator based on the method of moment [35]. The ring resonators in Fig.3 are designed at fundamental mode at 2GHz with dielectric constant  $\epsilon_r = 10.2$  and thickness  $h = 50$  mil. As seen from the simulation results in Fig. 3, both exhibit the same electrical current flows, which are current standing waves. Therefore, both one- and two-port ring resonators

have the same frequency modes as given in (11) or (13a). Furthermore, to experimentally verify the frequency modes of the one-port ring resonator, two one-port ring resonators are designed at fundamental mode of 2GHz based on (12a) and (13a), respectively. They are fabricated on RT/Duriod 60102.2 with dielectric constant  $\epsilon_r = 10.2$  and thickness  $h = 50\text{mil}$  and demonstrated in Figs. 4(a) and (b), respectively.

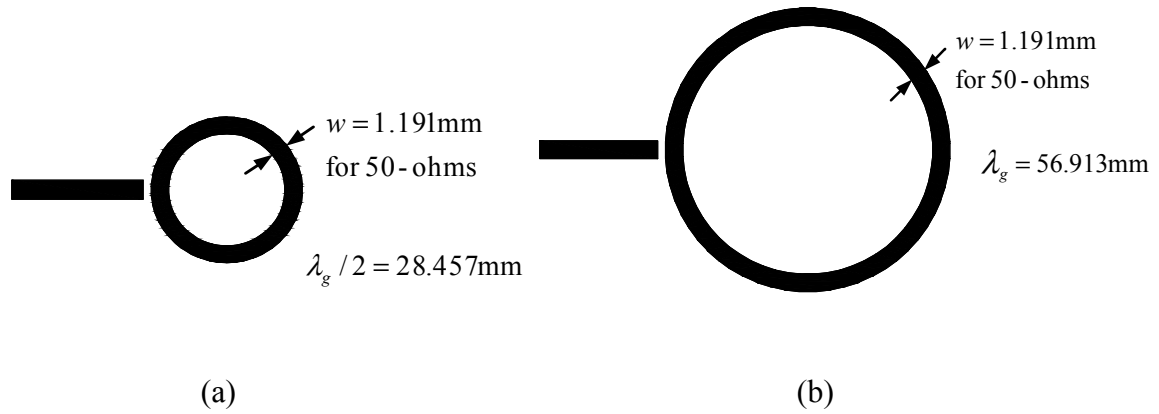


Fig. 4. Configurations of one-port ring resonators for mean circumferences of (a)  $\lambda_g / 2$  and (b)  $\lambda_g$ .

As seen the measured results in Fig. 5, the one-port ring resonator (Fig. 4(b)) designed by the frequency mode of (13a) illustrates five resonant frequencies from the fundamental mode of 2GHz to the mode  $n = 5$ . However, the one-port ring resonator (Fig. 4(a)) designed by the frequency mode of (12a) only shows two modes,  $n = 2$  and 4. With  $n = 2, 4, 6, \dots$  in (12a), Equation (12a) is identical to (13a). Therefore, from the measured results, it also confirms that the one-port ring resonator has the same frequency modes as the two-port ring resonator. This observation shows the statement on frequency modes in [10,34] regarding one-port ring resonator is not correct. Equation (13a) should be used for both one- and two-port ring circuit designs.

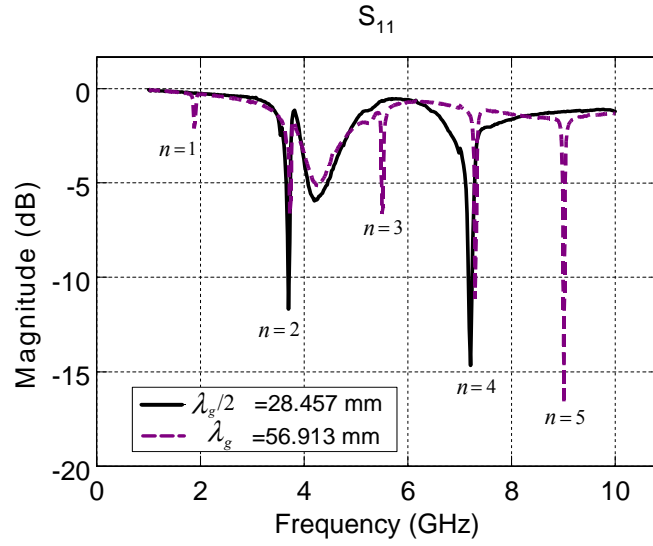


Fig. 5. Measured results for one-port ring resonators with modes  $n = 1$  to 5.

#### D. Dual Mode

The dual mode concept was originally introduced by Wolff [13]. The dual mode is composed of two degenerate modes or splitting resonant frequencies that may be excited by perturbing stubs, notches, or asymmetrical feed lines. The dual mode follows from the solution of Maxwell's equations for the magnetic-wall model of the ring resonator:

$$E_z = [AJ_n(kr) + BN_n(kr)]\cos(n\Phi) \quad (14a)$$

$$H_r = \frac{n}{j\omega\mu_0 r} [AJ_n(kr) + BN_n(kr)]\sin(n\Phi) \quad (14b)$$

$$H_\Phi = \frac{k}{j\omega\mu_0} [AJ'_n(kr) + BN'_n(kr)]\cos(n\Phi) \quad (14c)$$

$$\text{and } E_z = [AJ_n(kr) + BN_n(kr)]\sin(n\Phi) \quad (15a)$$

$$H_r = \frac{n}{j\omega\mu_0 r} [AJ_n(kr) + BN_n(kr)]\cos(n\Phi) \quad (15b)$$

$$H_\Phi = \frac{k}{j\omega\mu_0} [AJ'_n(kr) + BN'_n(kr)]\sin(n\Phi) \quad (15c)$$

where  $J_n(kr)$  and  $N_n(kr)$  are the Bessel functions of the first and second kinds of order  $n$ . The wave number is  $k = \sqrt{\epsilon_{eff}\epsilon_o\mu_o}$  where  $\epsilon_o$  and  $\mu_o$  are the permittivity and permeability in free space. The dual mode explanation of the magnetic-wall model is given as followings. If a ring resonator without any perturbations is excited by symmetrical feed lines, only one of the degenerate modes is generated. Both modes traveling clockwise and counter-clockwise on the ring resonator are orthogonal to each other without any coupling. Also, if the ring resonator is perturbed, two degenerated modes are excited and couple to each other.

In [10], however, the ring resonator with a perturbing stub or notch at  $\Phi = 45^\circ, 135^\circ, 225^\circ$ , or  $315^\circ$  generates the dual mode only for  $n \in \text{odd}$  modes. Inspecting (15) and (16), they cannot explain why the dual mode only happens for  $n \in \text{odd}$  modes instead of even modes when the ring resonator has a perturbing stub or notch at  $\Phi = 45^\circ, 135^\circ, 225^\circ$ , or  $315^\circ$ . Also, the magnetic-wall model cannot explain the dual mode of the ring resonator with complicate boundary conditions. This dual mode phenomenon may be explained more simply and more generally using the transmission-line model of section *B*, which describes the ring resonator as two identical  $\lambda_g/2$  resonators connected in parallel. As seen in Fig. 3, two identical current standing waves are established on the ring resonator in parallel. If the ring itself does not have any perturbation and is excited by symmetrical feed lines, two identical resonators are excited and produce the same frequency response, which overlap each other. However, if one of the  $\lambda_g/2$  resonators is perturbed out of balance with the other, two different frequency modes are excited and couple to each other. To investigate the dual mode behavior, a perturbed square ring resonator is simulated in Fig. 6. The perturbed square ring designed at fundamental mode of 2 GHz is fabricated on a RT/Duroid 6010.2  $\epsilon_r = 10.2$  substrate with a thickness  $h = 25$  mil.

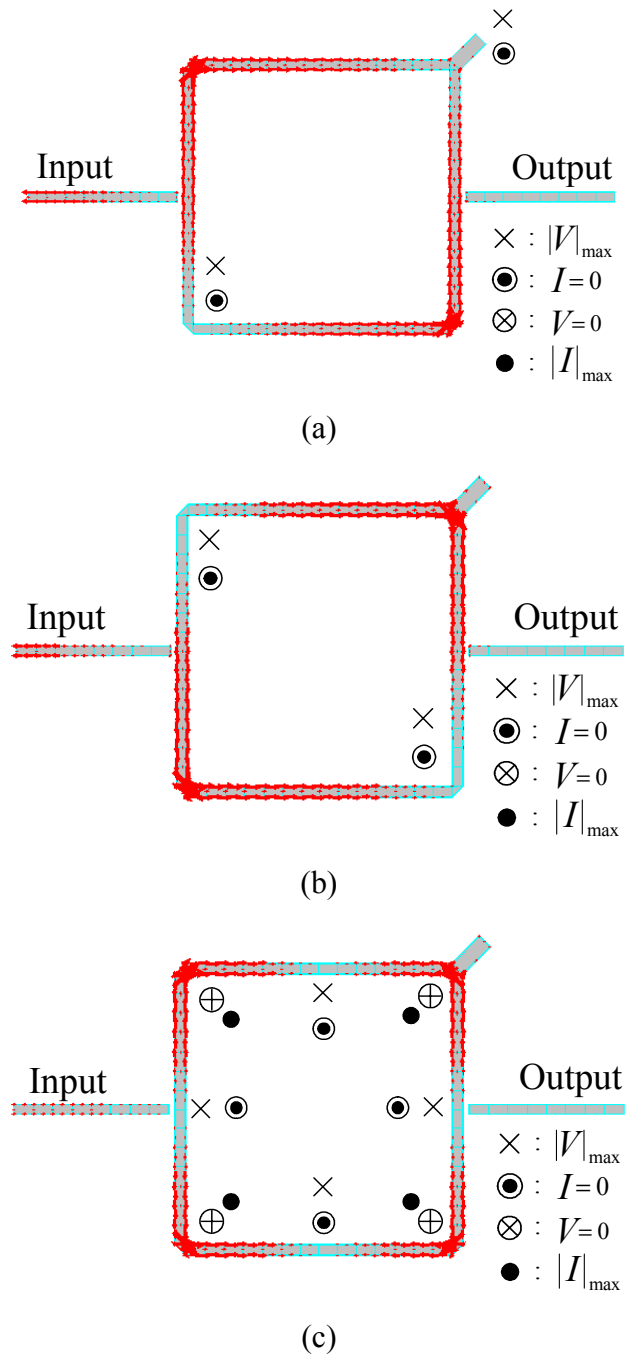


Fig. 6. The simulated electrical currents of the square ring resonator with a perturbed stub at  $\Phi = 45^\circ$  for (a) the low splitting resonant frequency of  $n = 1$  mode (b) high splitting resonant frequency of mode  $n = 1$ , and (c) mode  $n = 2$ .

Fig. 6 shows the simulated electric currents on the square ring resonator with a perturbing stub at  $\Phi = 45^\circ$  for the  $n = 1$  and the  $n = 2$  modes. For the  $n = 1$  mode, one of  $\lambda_g/2$  resonators is perturbed so that the two  $\lambda_g/2$  resonators do not balance each other. Thus, two splitting different resonant frequencies are generated. Figs. 6(a) and (b) show the simulated electrical currents for the splitting resonant frequencies. Fig. 7 illustrates the measured  $S_{21}$  confirming the splitting frequencies for the  $n = 1$  mode around 2 GHz. Furthermore, for the  $n = 2$  mode, Fig. 6(c) shows the perturbing stub located at the position of zero voltage which is a short circuit. Therefore, the perturbed stub does not disturb the resonator and both  $\lambda_g/2$  resonators balance each other without frequency splitting. Measured results in Fig. 7 has confirmed that the resonant frequency at the  $n = 2$  mode of 4 GHz is not affected by the perturbation.

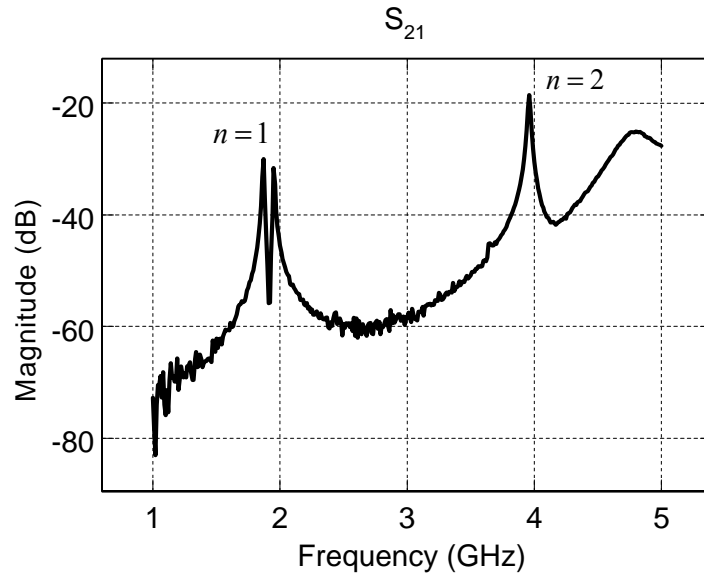


Fig. 7. The measured results for modes  $n = 1$  and 2 of the square ring resonator with a perturbed stub at  $\Phi = 45^\circ$ .

### *E. Conclusions*

A simple transmission-line model has been used to calculate the frequency modes of microstrip ring resonators of any shape such as annular, square, and meander. A literature error for frequency modes of the one-port ring resonator is proved by theory, electromagnetic simulation, and measured results. Furthermore, the transmission-line model gives a better explanation for dual mode behavior than the magnetic-wall model, especially for a ring resonator with complex boundary conditions. Experiments and simulations show good agreement with theory.

## CHAPTER III

EQUIVALENT LUMPED ELEMENTS  $G$ ,  $L$ ,  $C$  AND UNLOADED  $Q$ S OF  
CLOSED- AND OPEN-LOOP RING RESONATORS\**A. Introduction*

For the past three decades, the microstrip ring resonator has been widely utilized to measure the effective dielectric constant, dispersion, and discontinuity parameters and to determine optimum substrate thickness [1-4]. Beyond measurement applications, the microstrip ring resonator has also been used in filters, oscillators, mixers, and antennas [5] because of its advantages of compact size, easy fabrication, narrow passband bandwidth, and low radiation loss. Recently, interesting compact filters using microstrip ring or loop resonators for cellular and other mobile communication systems were reported [6-7].

The basic operation of the ring resonator based on the magnetic wall model was originally introduced by Wolff and Knoppik [2]. In addition, a simple mode chart of the ring was developed to describe the relation between the physical ring radius and resonant mode and frequency [9]. Although the mode chart of the magnetic wall model has been studied extensively, it provides only a limited description of the effects of the circuit parameters and dimensions [5]. A further study on a ring resonator using the transmission-line model was proposed [10]. The transmission-line model used a T-network in terms of equivalent impedances to analyze a ring circuit. However, this model showed a complex expression for the ring circuit. Another distributed-circuit model using cascaded transmission-line segments for a ring was reported [11]. The

---

\*Reprinted with permission from (complete publication information) "Equivalent lumped elements  $G$ ,  $L$ ,  $C$  and unloaded  $Q$ s of closed- and open-loop ring resonators" by Lung-Hwa Hsieh and Kai Chang, 2002. *IEEE Trans. Microwave Theory Tech.*, vol. 50, pp. 453- 460. © 2004 by the IEEE.



model can easily incorporate any discontinuities and solid-state devices along the ring. Although this model could predict the behavior of a ring resonator well, it could not provide a straightforward circuit view such as equivalent lumped elements  $G$ ,  $L$  and  $C$  for the ring circuit.

In this chapter, a simple equivalent lumped element  $G$ ,  $L$ , and  $C$  circuit for closed- and open-loop ring resonators through transmission-line analysis is developed. By using the equivalent lumped elements, the unloaded  $Q$  of the closed- and open-loop rings are obtained. Two different dielectric substrates with different types of rings are used to verify the unloaded  $Q$  calculation and equivalent circuit representation.

### *B. Equivalent Lumped Elements and Unloaded $Q$ s for Closed and Open-Loop Microstrip Ring Resonators*

#### *1) Closed-Loop Ring Resonators*

Fig. 8 shows the geometry of a closed-loop microstrip ring resonator. The simple equations of the ring are given by

$$2\pi r = n\lambda_g \quad (16a)$$

$$f_o = \frac{nc}{2\pi r \sqrt{\epsilon_{reff}}} \quad (16b)$$

where  $\lambda_g$  is the guided-wavelength,  $r$  is the mean radius of the ring,  $n$  is the mode number,  $f_o$  is the resonant frequency,  $c$  is the speed of light in free space, and  $\epsilon_{reff}$  is static effective relative dielectric constant. Observing this structure, if the width of the ring is narrow, then the ring might have the same dispersion characteristics as a transmission line resonator [36]. Therefore, the ring resonator can be a closed loop transmission line and analyzed by transmission-line model [5].

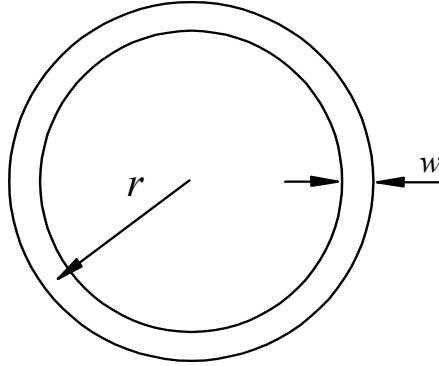


Fig. 8. A closed-loop microstrip ring resonator.

Fig. 9(a) illustrates the one-port network of the ring and its equivalent circuit. Inspecting Fig. 9(a), the equivalent input impedance of the ring is not easily derived from the one-port network. Another approach using the two-port network is shown in Fig. 9(b) with an open circuit at port 2 ( $i_2 = 0$ ) to model the one-port network and find the equivalent input impedance through  $ABCD$  and  $Y$  parameters matrixes operations [37]. As seen in Fig. 9(b), the mean circumference  $l = \lambda_g = 2\pi r$  for the fundamental mode  $n=1$  is divided by input and output ports on arbitrary positions of the ring with two sections  $l_1$  and  $l_2$ . The two sections form a parallel circuit. For this parallel circuit, a transmission-line  $ABCD$  matrix is utilized to find each section parameters. The  $ABCD$  matrix of the individual transmission line lengths  $l_1$  and  $l_2$  is given as follows:

$$\begin{bmatrix} A & B \\ C & D \end{bmatrix}_{1,2} = \begin{bmatrix} \cosh(\gamma l_{1,2}) & Z_o \sinh(\gamma l_{1,2}) \\ Y_o \sinh(\gamma l_{1,2}) & \cosh(\gamma l_{1,2}) \end{bmatrix}, \quad \gamma = \alpha + j\beta \quad (17)$$

where subscript 1 and 2 are corresponding to the transmission lines  $l_1$  and  $l_2$ , respectively,  $Z_o = 1/Y_o$  is the characteristic impedance of the microstrip ring resonator,

$\gamma$  is the complex propagation constant,  $\alpha$  is the attenuation constant, and  $\beta$  is the phase constant.

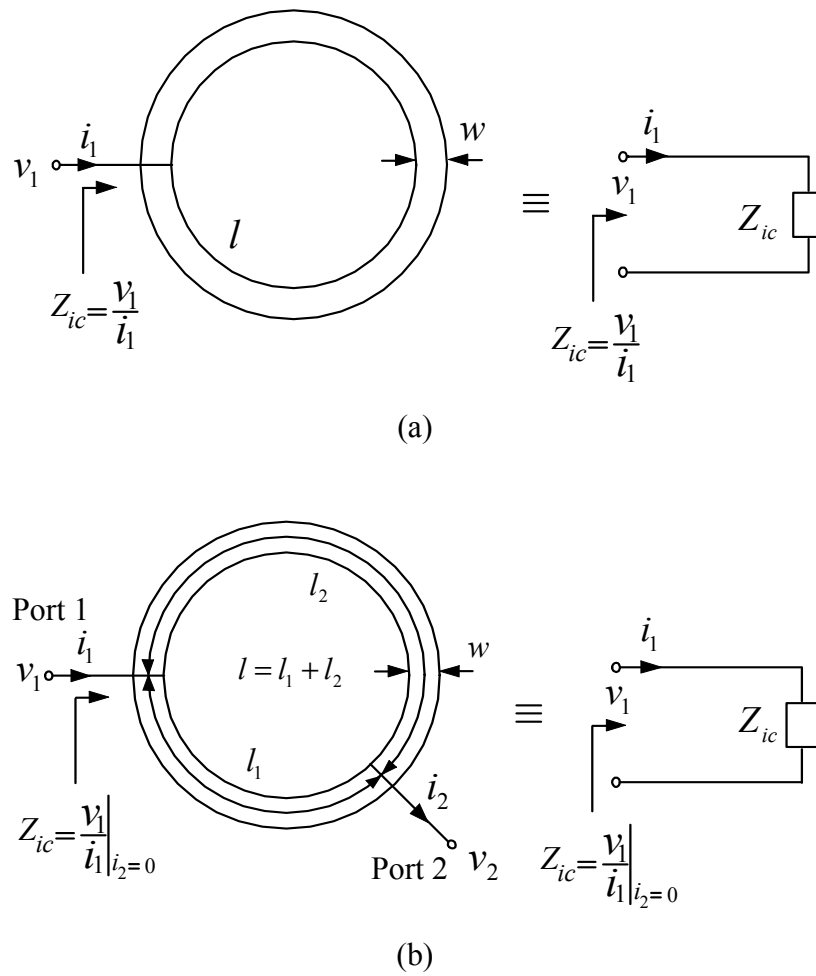


Fig. 9. The input impedance of (a) one-port network and (b) two-port network of the closed-loop ring resonator.

The overall  $Y$  parameters converted from  $ABCD$  matrix in (17) for the parallel circuit are given by

$$\begin{bmatrix} Y_{11} & Y_{12} \\ Y_{21} & Y_{22} \end{bmatrix} = \begin{bmatrix} Y_o[\coth(\gamma_1) + \coth(\gamma_2)] & -Y_o[\operatorname{csch}(l_1) + \operatorname{csch}(\gamma_2)] \\ -Y_o[\operatorname{csch}(\gamma_1) + \operatorname{csch}(\gamma_2)] & Y_o[\coth(l_1) + \coth(\gamma_2)] \end{bmatrix}. \quad (18)$$

By setting  $i_2$  to zero, the input impedance  $Z_{ic}$  of the closed-loop ring in Fig. 9(b) can be found as follows:

$$Z_{ic} = \left. \frac{v_1}{i_1} \right|_{i_2=0} = \frac{Z_o}{2} \frac{\sinh(\gamma)}{\cosh(\gamma) - 1}. \quad (19)$$

Letting  $l_g = l/2 = \lambda_g/2$ , Equation (19) can be rewritten as

$$Z_{ic} = \frac{Z_o}{2} \frac{1 + j \tanh(\alpha l_g) \tan(\beta l_g)}{\tanh(\alpha l_g) + j \tan(\beta l_g)}. \quad (20)$$

In most practical cases, transmission lines have small loss so that the attenuation term can be assumed that  $\alpha l_g \ll 1$  and then  $\tanh(\alpha l_g) \approx \alpha l_g$ . Considering the  $\beta l_g$  term and letting the angular frequency  $\omega = \omega_o + \Delta\omega$ , where  $\omega_o$  is the resonant angular frequency and  $\Delta\omega$  is small,

$$\beta l_g = \frac{\omega_o l_g}{v_p} + \frac{\Delta\omega l_g}{v_p} \quad (21)$$

where  $v_p$  is the phase velocity of the transmission line. When a resonance occurs,

$\omega = \omega_o$  and  $l_g = \lambda_g/2 = \frac{\pi v_p}{\omega_o}$ . Thus, Equation (21) can be rewritten as

$$\beta l_g = \pi + \frac{\pi \Delta \omega}{\omega_o} \quad (22a)$$

and

$$\tanh(\beta l_g) \approx \frac{\pi \Delta \omega}{\omega_o} . \quad (22b)$$

Using these results, the input impedance  $Z_{ic}$  can be approximated as

$$Z_{ic} \cong \frac{Z_o}{2} \frac{1 + j \alpha l_g \frac{\pi \Delta \omega}{\omega_o}}{\alpha l_g + j \frac{\pi \Delta \omega}{\omega_o}} . \quad (23)$$

Since  $\alpha l_g \frac{\pi \Delta \omega}{\omega_o} \ll 1$  ,  $Z_{ic}$  can be rewritten as

$$Z_{ic} \cong \frac{(Z_o / 2 \alpha l_g)}{1 + j \frac{\pi \Delta \omega}{\alpha l_g \omega_o}} . \quad (24)$$

For a general parallel  $GLC$  circuit, the input impedance is [38]

$$Z_i = \frac{1}{G + 2j\Delta\omega C} . \quad (25)$$

Comparing (24) with (25), the input impedance of the closed-loop ring resonator has the same form as that of a parallel  $GLC$  circuit. Therefore, the conductance of the equivalent circuit of the ring is

$$G_c = \frac{2\alpha l_g}{Z_o} = \frac{\alpha \lambda_g}{Z_o} \quad (26a)$$

and the capacitance of the equivalent circuit of the ring is

$$C_c = \frac{\pi}{Z_o \omega_o}. \quad (26b)$$

The inductance of the equivalent circuit of the ring can be derived from  $\omega_o = 1/\sqrt{L_c C_c}$  and is given by

$$L_c = \frac{1}{\omega_o^2 C_c} \quad (26c)$$

where  $G_c$ ,  $C_c$ , and  $L_c$  stand for the equivalent conductance, capacitance, and inductance of the closed-loop ring resonator. Fig. 10 shows the equivalent lumped element circuit of the ring in terms of  $G_c$ ,  $C_c$ , and  $L_c$ . Moreover, the unloaded  $Q$  of the ring resonator can be found from equation (26) and the unloaded  $Q$  is

$$Q_{uc} = \frac{\omega_o C_c}{G_c} = \frac{\pi}{\alpha \lambda_g}. \quad (27)$$

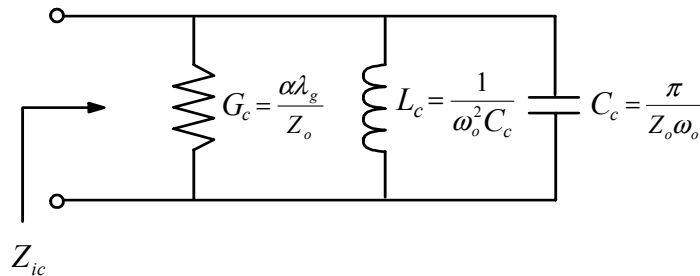


Fig. 10. Equivalent elements  $G_c$ ,  $C_c$ , and  $L_c$  of the closed-loop ring resonator.

For a square ring resonator as shown in Fig. 11, the equivalent  $G_c$ ,  $C_c$ ,  $L_c$  and unloaded  $Q$  can be derived by the same procedures as above. Through the derivations, it can be found that the equivalent  $G_c$ ,  $C_c$ ,  $L_c$  and unloaded  $Q$  of the square ring resonator is the same as that of the annular ring resonator in Fig. 9.

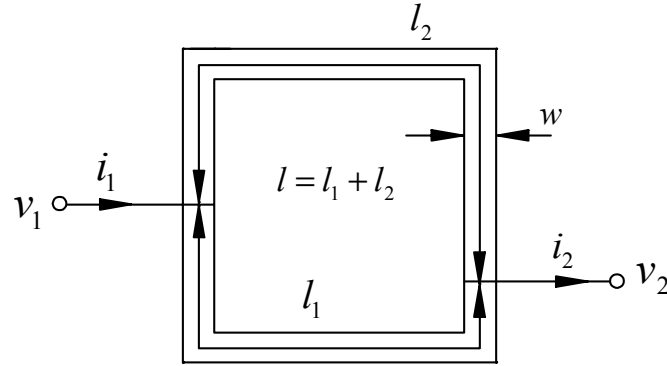


Fig. 11. Transmission-line model of the closed-loop square ring resonator.

## 2) Open-Loop Ring Resonators

Fig. 12(a) illustrates the configuration of an open-circuited  $\lambda_g/2$  microstrip ring resonator. As seen in Fig. 12(a),  $l_3$  is the physical length of the ring,  $C_g$  is the gap capacitance, and  $C_f$  is the fringe capacitance caused by fringe field at the both ends of the ring. The fringe capacitance can be replaced by an equivalent length  $\Delta l$  [39]. Considering the open-end effect, the equivalent length of the ring is  $l_3 + 2\Delta l = \lambda_g/2 = l_g$  for the fundamental mode.

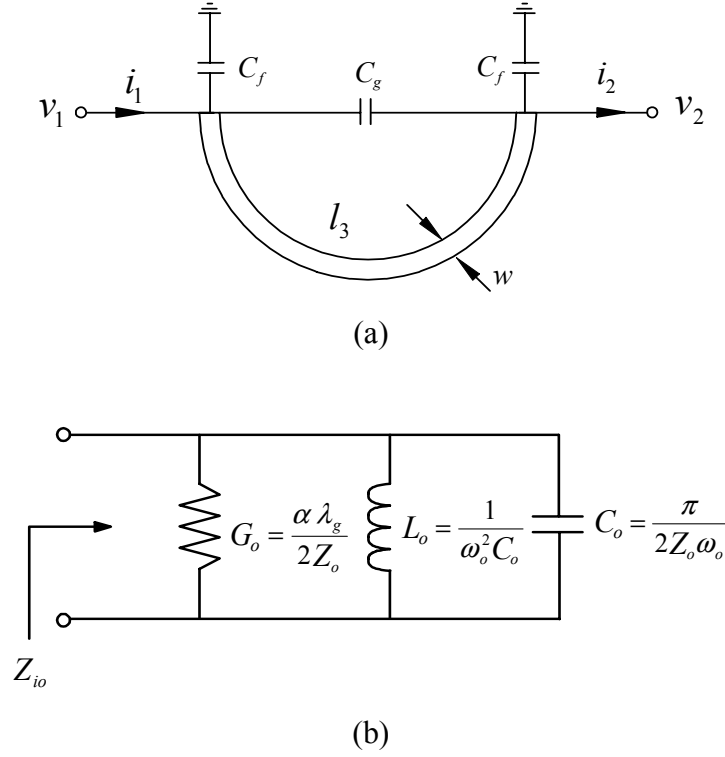


Fig. 12. Transmission-line model of (a) the open-loop ring resonator and (b) its equivalent elements  $G_o$ ,  $L_o$ , and  $C_o$ .

In Fig. 12(a), the parallel circuit split by input and output ports is composed of the gap capacitor  $C_g$  and the ring resonator. Furthermore, the  $ABCD$  matrix of the individual element of  $C_g$  and the ring can be expressed as follows:

$$\begin{bmatrix} A & B \\ C & D \end{bmatrix}_{C_g} = \begin{bmatrix} 1 & 1/Y_g \\ 0 & 1 \end{bmatrix} \quad (28)$$

$$\begin{bmatrix} A & B \\ C & D \end{bmatrix}_{open} = \begin{bmatrix} \cosh(\gamma l_g) & Z_o \sinh(\gamma l_g) \\ Y_o \sinh(\gamma l_g) & \cosh(\gamma l_g) \end{bmatrix} \quad (29)$$

where subscripts  $C_g$  and  $open$  are for the gap capacitor and the open-loop ring resonator, respectively,  $Y_g = j\omega C_g$  is the admittance of  $C_g$ ,  $Z_o = 1/Y_o$  is the characteristic



impedance of the ring. The overall  $Y$  parameters converted from  $ABCD$  matrix in (28) and (29) for the parallel ring circuit are given by

$$\begin{bmatrix} Y_{11} & Y_{12} \\ Y_{21} & Y_{22} \end{bmatrix} = \begin{bmatrix} Y_g + Y_o \coth(\gamma l_g) & -Y_g - Y_o \csc h(\gamma l_g) \\ -Y_g - Y_o \csc h(\gamma l_g) & Y_g + Y_o \coth(\gamma l_g) \end{bmatrix}. \quad (30)$$

Observing the two-port network shown in Fig. 12(a), the input impedance of the ring can be calculated by setting output current  $i_2$  to zero. In this condition, the input impedance  $Z_{io}$  can be written as

$$Z_{io} = \left. \frac{v_1}{i_1} \right|_{i_2=0} = \frac{Y_o \cosh(\mathcal{M}_g) + Y_g \sinh(\mathcal{M}_g)}{Y_o^2 \sinh(\mathcal{M}_g) + 2Y_o Y_g [\cosh(\mathcal{M}_g) - 1]}. \quad (31)$$

If the gap size between two open ends of the ring is large, then the effect of the gap capacitor  $C_g$  for the ring can be ignored [40]. This implies  $Y_g \approx 0$ . Therefore, the input impedance  $Z_{io}$  of the open-loop ring can be approximated as

$$Z_{io} \cong Z_o \frac{1 + j \tanh(\alpha l_g) \tan(\beta l_g)}{\tanh(\alpha l_g) + j \tan(\beta l_g)}. \quad (32)$$

Also, using the same assumptions and derivations for  $\alpha l_g$  and  $\beta l_g$  as in part 1 of this section, the input impedance can be obtained by

$$Z_{io} = \frac{(Z_o / \alpha l_g)}{1 + j \frac{\pi \Delta \omega}{\alpha l_g \omega_o}}. \quad (33)$$

Comparing (33) with (25), the input impedance of the ring has the same form as that of a parallel *GLC* circuit. Thus, the conductance, capacitance and inductance of the equivalent circuit of the ring are

$$G_o = \frac{\alpha \lambda_g}{2Z_o}, \quad C_o = \frac{\pi}{2Z_o \omega_o}, \quad \text{and} \quad L_o = \frac{1}{\omega_o^2 C_o}. \quad (34)$$

The equivalent circuit in terms of  $G_o$ ,  $C_o$ , and  $L_o$  is shown in Fig. 12(b). Moreover, the unloaded  $Q$  of the ring is given by

$$Q_{uo} = \frac{\omega_o C_o}{G_o} = \frac{\pi}{\alpha \lambda_g}. \quad (35)$$

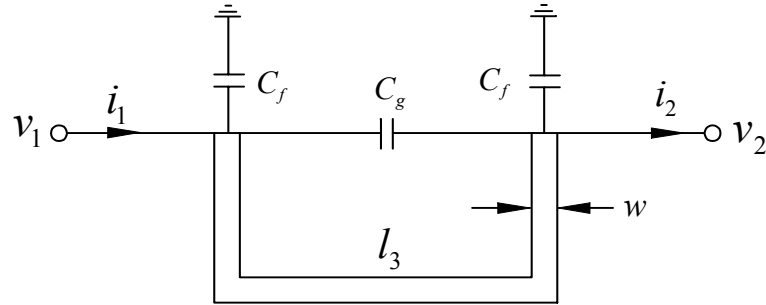


Fig. 13. Transmission-line model of the U-shaped open-loop ring resonator.

Fig. 13 illustrates an U-shaped open-loop ring. Also, following the same derivations used in this section, the equivalent lumped elements  $G_o$ ,  $C_o$ ,  $L_o$  and unloaded  $Q$  of the U-shaped ring resonator can be found to be identical to those of the open-loop ring resonator with the curvature effect. Inspecting the equivalent conductances, capacitances, and inductances of the closed- and open-loop ring resonators from (26) and

(34), the relations of the equivalent lumped elements  $GLC$  between these two rings can be found as follows:

$$G_c = 2G_o \text{ for the same attenuation constant,} \quad (36a)$$

$$C_c = 2C_o, \text{ and } L_c = L_o / 2. \quad (36b)$$

In addition, observing (27) and (35), the unloaded  $Q$  of the closed- and open-loop ring resonators are equal, namely

$$Q_{uc} = Q_{uo} \text{ for the same attenuation constant.} \quad (37)$$

Equations (36a) and (37) sustain for the same losses condition of the closed- and the open-loop ring resonator. In practice, the total losses for the closed- and the open-loop ring resonator are not the same. In addition to the dielectric and conductor losses, the open-loop ring resonator has a radiation loss caused by the open ends [41]. Thus, total losses of the open-loop ring are larger than that of the closed-loop ring. Under this condition, (36a) and (37) should be rewritten as follows:

$$Q_{uc} > Q_{uo} \text{ and } G_c < 2G_o. \quad (38)$$

### *C. Calculated and Measured Unloaded $Q$ s and Equivalent Lumped Elements for Ring Resonators*

#### *1) Calculated Method*

The attenuation constant of a microstrip line is given as follow: [42]

$$\alpha = \alpha_d + \alpha_c \quad (39)$$

where  $\alpha_d$  and  $\alpha_c$  are dielectric and conductor attenuation constants, respectively. The dielectric attenuation constant is given by

$$\alpha_d = 27.3 \frac{\epsilon_r}{\epsilon_r - 1} \frac{\epsilon_{reff} - 1}{\sqrt{\epsilon_{reff}}} \frac{\tan \delta}{\lambda_o} \quad (40)$$

where  $\epsilon_r$  is the relative dielectric constant,  $\tan \delta$  is the loss tangent, and  $\lambda_o$  is the wavelength in free space. If operation frequency is larger than dispersion frequency [37]

$$f_d (GHz) = 0.3 \sqrt{\frac{Z_o}{h \sqrt{\epsilon_r - 1}}} \quad (41)$$

where  $h$  is the substrate thickness in centimeters, then (40) has to include the effects of dispersion [43] as follows:

$$\alpha_d = 27.3 \frac{\epsilon_r}{\epsilon_r - 1} \frac{\epsilon_{reff}(f) - 1}{\sqrt{\epsilon_{reff}(f)}} \frac{\tan \delta}{\lambda_o}. \quad (42)$$

The conductor attenuation constant  $\alpha_c$  can be approximately expressed as [42]

$$w/h \leq 1/2\pi$$

$$\alpha_c = \frac{8.68R_{s1}}{2\pi z_o h} \left[ 1 - \left( \frac{w_{eff}}{4h} \right)^2 \right] \left[ 1 + \frac{h}{w_{eff}} + \frac{h}{\pi w_{eff}} \left( \ln \frac{4\pi w}{t} + \frac{t}{w} \right) \right] \text{ dB/unit length} \quad (43a)$$

$$1/2\pi \leq w/h \leq 2$$

$$\alpha_c = \frac{8.68R_{s1}}{2\pi z_o h} \left[ 1 - \left( \frac{w_{eff}}{4h} \right)^2 \right] \left[ 1 + \frac{h}{w_{eff}} + \frac{h}{\pi w_{eff}} \left( \ln \frac{2h}{t} - \frac{t}{h} \right) \right] \text{ dB/unit length} \quad (43b)$$

$$w/h \geq 2$$

$$\alpha_c = \frac{8.68R_{s1}}{z_o h} \left\{ \frac{w_{eff}}{h} + \frac{2}{\pi} \ln \left[ 2\pi e \left( \frac{w_{eff}}{2h} + 0.94 \right) \right] \right\}^{-2} \left[ \frac{w_{eff}}{h} + \frac{w_{eff}/\pi h}{\frac{w_{eff}}{2h} + 0.94} \right] \times$$

$$\left[ 1 + \frac{h}{w_{eff}} + \frac{h}{\pi w_{eff}} \left( \ln \frac{2h}{t} - \frac{t}{h} \right) \right] \text{ dB/unit length} \quad (43c)$$

with  $R_{s1} = R_s \left\{ 1 + \frac{2}{\pi} \tan^{-1} \left[ 1.4 \left( \frac{\Delta}{\delta_s} \right)^2 \right] \right\}$  and  $R_s = \sqrt{\frac{\pi f \mu_o}{\sigma}}$  [44] where  $R_{s1}$  is the surface-roughness resistance of the conductor,  $R_s$  is the surface resistance of the conductor,  $\Delta$  is the surface roughness,  $\delta_s = 1/(R_s \sigma)$  is the skin depth,  $\sigma$  is the conductivity of the microstrip line,  $f$  is the frequency,  $\mu_o$  is the permeability of free-space,  $t$  is the microstrip thickness, and  $w$  is the width of the microstrip line. The effective width  $w_{eff}$  can be found in [45]. The unloaded  $Q$  of the closed-loop ring can be calculated by

$$\frac{1}{Q_{uc}} = \frac{1}{Q_d} + \frac{1}{Q_c} \quad (44)$$

where  $Q_d = \frac{\pi}{\alpha_d \lambda_g}$  is the  $Q$ -factor caused by the dielectric loss of the ring and  $Q_c = \frac{\pi}{\alpha_c \lambda_g}$  is the  $Q$ -factor caused by the conductor loss of the ring. The attenuation constant of the closed-loop ring is

$$\alpha_{ca} = \alpha_d + \alpha_c \text{ Np/unit length for the fundamental mode.} \quad (45)$$

The radiation loss caused by open ends of the open-loop ring resonator in terms of radiation quality factor is [41]

$$Q_r = \frac{Z_o}{480\pi(h/\lambda_o)^2 F} \quad (46)$$

where  $F = \frac{\epsilon_{\text{reff}}(f)+1}{\epsilon_{\text{reff}}(f)} - \frac{[\epsilon_{\text{reff}}(f)-1]^2}{2[\epsilon_{\text{reff}}(f)]^{3/2}} \ln \left[ \frac{\sqrt{\epsilon_{\text{reff}}(f)+1}}{\sqrt{\epsilon_{\text{reff}}(f)-1}} \right]$ . The unloaded  $Q$  of the open-loop ring can be given by

$$\frac{1}{Q_{uo}} = \frac{1}{Q_d} + \frac{1}{Q_c} + \frac{1}{Q_r}. \quad (47)$$

The attenuation constant of the open-loop ring resonator can be derived from (35). That is

$$\alpha_{oa} = \frac{\pi}{Q_{uo} \lambda_g} \text{ Np/unit length for the fundamental mode.} \quad (48)$$

By using the attenuation constants in (45) and (48), the calculated equivalent lumped elements for closed- and open-loop rings can be obtained from (26) and (34).

## 2) Measured Method

The measured unloaded  $Q$  of a microstrip resonator can be obtained by [5]

$$Q_{u,meas} = \frac{Q_{L,meas}}{1 - 10^{-L_{meas}/20}} \quad (49)$$

where the subscript *meas* stands for measured data,  $Q_{L,meas}$  is the loaded  $Q$  and  $L_{meas}$  is the measured insertion loss in dB of the resonator at resonance. The loaded  $Q$  is defined as

$$Q_{L,meas} = \frac{f_{o,meas}}{BW_{3dB,meas}} \quad (50)$$

where  $f_{o,meas}$  is the measured resonant frequency and  $BW_{3dB,meas}$  is the measured 3 dB-bandwidth of a resonator. Also, using (27) and (35), the measured attenuation constant for closed- and open-loop rings can be given by

$$\alpha_{ca,meas} = \frac{\pi}{Q_{cu,meas} \lambda_g} \text{ Np/unit length for the fundamental mode.} \quad (51a)$$

and 
$$\alpha_{oa,meas} = \frac{\pi}{Q_{ou,meas} \lambda_g} \text{ Np/unit length for the fundamental mode.} \quad (51b)$$

Thus, the equivalent lumped elements  $G$ ,  $L$ , and  $C$  of the closed- and open-loop rings can be found as follows:

$$G_{c,meas} = \frac{\alpha_{ca,meas} \lambda_g}{Z_o}, \quad C_{c,meas} = \frac{\pi}{Z_o \omega_{o,meas}}, \quad L_{c,meas} = \frac{1}{\omega_{o,meas}^2 C_{c,meas}}. \quad (52a)$$

$$G_{o,meas} = \frac{\alpha_{oa,meas} \lambda_g}{2Z_o}, \quad C_{o,meas} = \frac{\pi}{2Z_o \omega_{o,meas}}, \quad L_{o,meas} = \frac{1}{\omega_{o,meas}^2 C_{o,meas}}. \quad (52b)$$

#### D. Calculated and Experimental Results

To verify the calculations presented in section C, four configurations of the closed- and open-loop ring resonators were designed at the fundamental mode of 2 GHz. The circuits, shown in Fig. 14, were fabricated for two different dielectric constants: RT/Duriod 5870 with  $\epsilon_r = 2.33$ ,  $h = 10$  mil and  $t = 0.7$  mil and RT/Duriod 6010.2 with  $\epsilon_r = 10.2$ ,  $h = 10$  mil and  $t = 0.7$  mil.

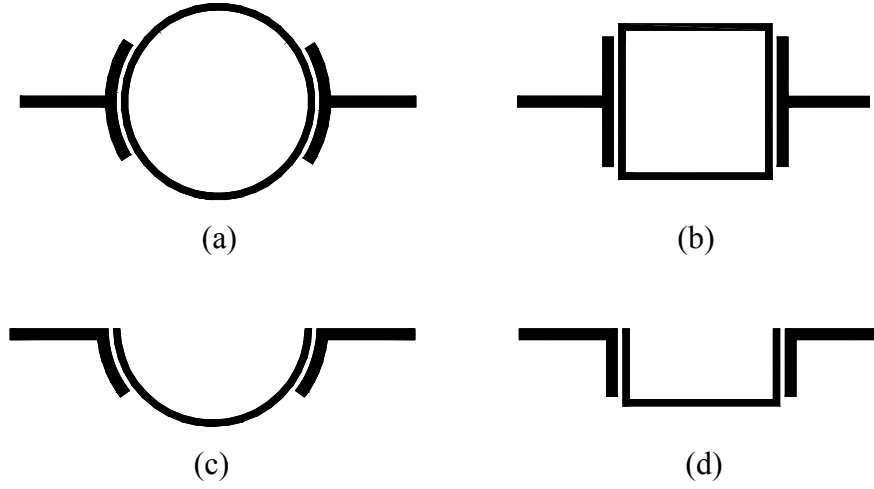


Fig. 14. Layouts of the (a) annular (b) square (c) open-loop with the curvature effect and (d) U-shaped open-loop ring resonators.

Table I Unloaded  $Q$ s for the parameters:  $\epsilon_r = 2.33$ ,  $h = 10$  mil,  $t = 0.7$  mil,  $w = 0.567$  mm for a 60-ohms line,  $\Delta = 1.397\mu\text{m}$  and  $\lambda_g = 108.398$  mm

Resonators	Annular Ring	Semi-Annular Ring	Square Ring	Semi-Square Ring
Designed Frequency (GHz)	2	2	2	2
Measured Frequency (GHz)	1.963	1.964	1.977	1.983
Measured Insertion Loss	32.66	31.33	32.3	33.12
Measured $BW_{3dB, meas}$ (MHz)	19	19.5	19	19.5
Measured Loaded $Q$	103.32	100.72	104.05	101.69
Measured Unloaded $Q$	105.78	103.53	106.64	103.98
Calculated Unloaded $Q$	103.35	102.41	103.35	102.41



Table II Equivalent elements for the parameters:  $\epsilon_r = 2.33$ ,  $h = 10$  mil,  $t = 0.7$  mil,  $w = 0.567$  mm for a 60-ohms line,  $\Delta = 1.397\mu\text{m}$  and  $\lambda_g = 108.398\text{mm}$

Resonators	Annular Ring	Semi-Annular Ring	Square Ring	Semi-Square Ring
Calculated $\alpha$ (dB/mm)	$2.45 \times 10^{-3}$	$2.43 \times 10^{-3}$	$2.45 \times 10^{-3}$	$2.43 \times 10^{-3}$
Calculated Conductance $G$ (mS)	0.508	0.256	0.508	0.256
Calculated Capacitor $C$ (pF)	4.17	2.08	4.17	2.08
Calculated Inductor $L$ (nH)	1.52	3.04	1.52	3.04
Measured $\alpha_{meas}$ (dB/mm)	$2.38 \times 10^{-3}$	$2.43 \times 10^{-3}$	$2.36 \times 10^{-3}$	$2.42 \times 10^{-3}$
Measured Conductance $G$ (mS)	0.495	0.253	0.49	0.252
Measured Capacitor $C$ (pF)	4.25	2.12	4.22	2.1
Measured Inductor $L$ (nH)	1.55	3.1	1.54	3.07

As seen in Tables I through IV, the measured unloaded  $Q$ s and lumped elements of the closed- and open-loop rings show good agreement with each other. In comparison of the measured results with calculated ones, the differences are caused by measurement uncertainties and accuracies of the calculated equations. The largest difference between the measured and calculated unloaded  $Q$  showing in Table III for the closed-loop square ring resonator is 5.7%. Furthermore, considering the radiation effect of the open-loop ring resonator fabricated by  $\epsilon_r = 2.33$  with  $h = 10\text{mil}$ , an EM simulator is used to investigate. The simulator is based on an integral equation and method of moment [35].

Table III Unloaded  $Q$ s for the parameters:  $\epsilon_r = 10.2$ ,  $h = 10$  mil,  $t = 0.7$  mil,  $w = 0.589$  mm for a 30-ohms line,  $\Delta = 1.397\mu\text{m}$  and  $\lambda_g = 55.295$  mm

Resonators	Annular Ring	Semi-Annular Ring	Square Ring	Semi-Square Ring
Designed Frequency (GHz)	2	2	2	2
Measured Frequency (GHz)	1.974	1.968	2.03	2.03
Measured Insertion Loss	35.83	35.48	35.48	33.4
Measured $BW_{3dB, meas}$ (MHz)	20.5	21	20.5	21
Measured Loaded $Q$	96.29	95.36	97.71	95.38
Measured Unloaded $Q$	97.87	96.99	99.38	97.46
Calculated Unloaded $Q$	93.65	93.21	93.65	93.21

Table IV Equivalent elements for the parameters:  $\epsilon_r = 10.2$ ,  $h = 10$  mil,  $t = 0.7$  mil,  $w = 0.589$  mm for a 30-ohms line,  $\Delta = 1.397\mu\text{m}$  and  $\lambda_g = 55.295$  mm

Resonators	Annular Ring	Semi-Annular Ring	Square Ring	Semi-Square Ring
Calculated $\alpha$ (dB/mm)	$5.29 \times 10^{-3}$	$5.27 \times 10^{-3}$	$5.29 \times 10^{-3}$	$5.27 \times 10^{-3}$
Calculated Conductance $G$ (mS)	1.12	0.56	1.12	0.56
Calculated Capacitor $C$ (pF)	8.33	4.17	8.33	4.17
Calculated Inductor $L$ (nH)	0.76	1.52	0.76	1.52
Measured $\alpha_{meas}$ (dB/mm)	$5.04 \times 10^{-3}$	$5.09 \times 10^{-3}$	$4.97 \times 10^{-3}$	$5.06 \times 10^{-3}$
Measured Conductance $G$ (mS)	1.06	0.54	1.05	0.54
Measured Capacitor $C$ (pF)	8.44	4.23	8.21	4.11
Measured Inductor $L$ (nH)	0.77	1.54	0.75	1.5

### E. Conclusions

An equivalent lumped-element circuit representation for the closed- and open-loop ring resonators was developed by a transmission-line analysis. Using the calculated  $G$ ,  $L$ ,  $C$  element values, the unloaded  $Q$ s for both the closed- and open-loop ring resonators were obtained. Two different dielectric constant substrates were used to verify the unloaded  $Q$ s and the equivalent lumped elements. The measured results show good agreement with the theory. These novel expressions using the equivalent lumped elements  $G$ ,  $L$ ,  $C$  and unloaded  $Q$  for the ring resonators can provide a simple way to design ring circuits.

## CHAPTER IV

DUAL-MODE BANDPASS FILTERS USING RING RESONATORS WITH  
ENHANCED-COUPPLING TUNING STUBS\**A. Introduction*

The microstrip ring resonator has been widely used to evaluate phase velocity, dispersion and effective dielectric constant of microstrip lines. The main attractive features of ring resonator are not only limited to its compact size, low cost and easy fabrication but also presents narrow passband bandwidth and low radiation loss. Many applications, such as bandpass filters, oscillators, mixers, and antennas using ring resonators have been reported [5]. Moreover, most of the established bandpass filters were built by dual-mode ring resonators, which were originally introduced by Wolff [13]. The dual-mode consists of two degenerate modes, which are excited by asymmetrical feed lines, added notches, or stubs on the ring resonator [5,13,14]. The coupling between the two degenerate modes is used to construct a bandpass filter. By proper arrangement of feed lines, notches, or stubs, the filter can achieve Chebyshev, elliptic or quasi-elliptic characteristics. Recently, one interesting excitation method using asymmetrical feed lines with lumped capacitors at input and output ports to design a bandpass filter was proposed [17].

Low insertion loss, high return loss, and high rejection band are the desired characteristics of a good filter. However, a conventional end-to-side coupling ring resonator suffers from high insertion loss, which is due to circuit's conductor, dielectric, radiation losses and an inadequate coupling between feeders and the ring resonator. The

---

\*Reprinted with permission from (complete publication information) "Dual-mode quasi-elliptic-function bandpass filters using ring resonators with enhanced-coupling tuning stubs" by Lung-Hwa Hsieh and Kai Chang, 2002. *IEEE Trans. Microwave Theory Tech.*, vol. 50, pp. 1340- 1345. © 2004 by the IEEE.

size of the coupling gap between ring resonator and feed lines affects the strength of coupling and the resonant frequency [5]. For instance, for a narrow coupling gap size, the ring resonator has a tight coupling and can provide a low insertion loss but the resonant frequency will be influenced greatly and for a wide gap size, the resonator has a high insertion loss and the resonant frequency is slightly affected. In order to improve the insertion loss, some structures have been published to enhance the coupling strength of ring resonators [18-21]. Several recent developments of the ring resonator using high temperature superconductor (HTS) thin film and micromachined circuit technologies have been presented [46-48]. This approach has the main advantage of very low conductor loss and therefore, a low insertion loss is expected. In addition, some configurations are suggested to use active devices combined into the ring resonator to provide gain to compensate for the loss [22,23]. In this chapter, novel quasi-elliptic-function bandpass filters using microstrip ring resonators with low insertion loss have been developed. A *L*-shape coupling arm was introduced to enhance the coupling and to generate perturbation for dual mode excitation. The effects of the coupling gap and stub length have been studied. Filters using one, two, and three ring resonators are demonstrated and compared. These new types of bandpass filters have been verified by simulation and measurement. Both simulated and measured results exhibit a good agreement.

#### *B. Dual-mode Bandpass Filter Using a Single Ring Resonator*

The basic structure of the proposed dual-mode filter is shown in Fig. 15(a). The square ring resonator is fed by a pair of orthogonal feed lines and each feed line is connected to a *L*-shape coupling arm. Fig. 15(b) displays the scheme of the coupling arm that consists of a coupling stub and a tuning stub. The tuning stub is attached to the end of the coupling stub. As seen from the circuit layout, the tuning stub extends the coupling stub to increase the coupling periphery. In addition, the asymmetrical structure perturbs the field of the ring resonator and excites two degenerate modes [13]. Without the tuning stubs, there is no perturbation on the ring resonator and only a single mode is

excited [6]. Comparing the new filter with conventional ones [5], which use perturbing notches or stubs inside the ring resonator, the conventional filters only provide dual-mode characteristics without the benefits of enhanced coupling strength and performance optimization.

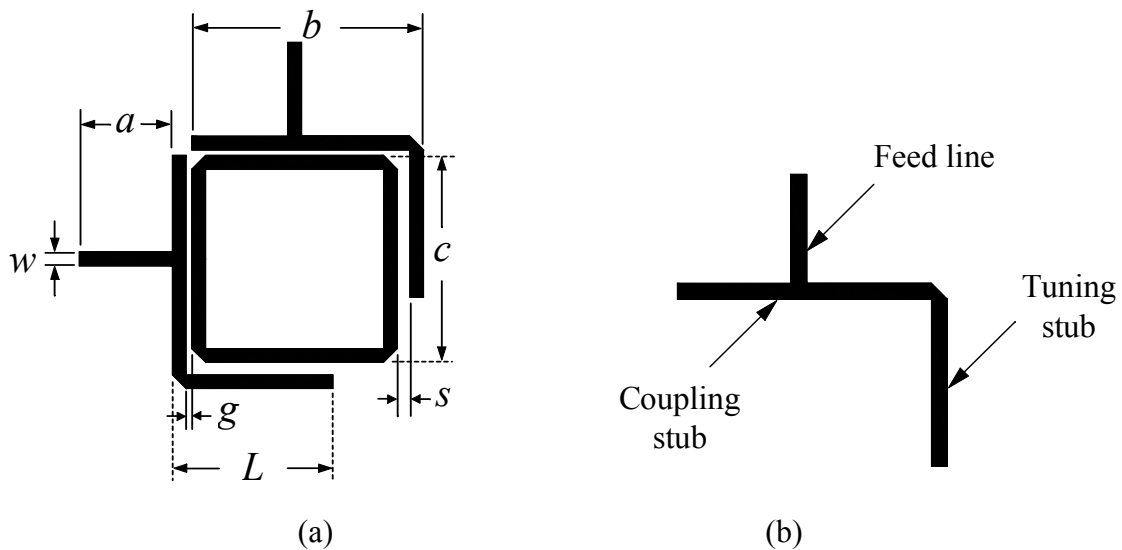
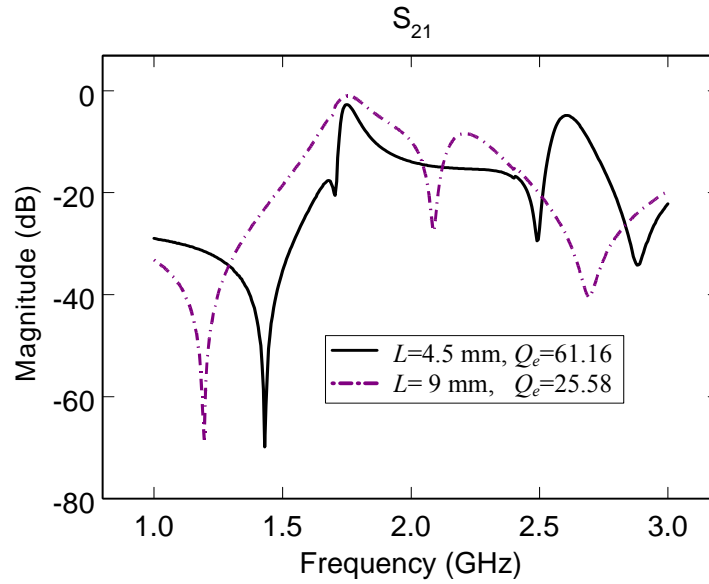


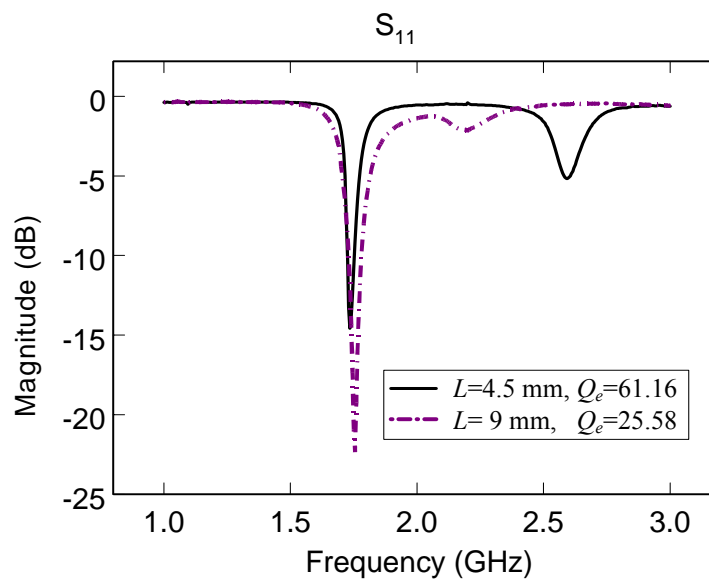
Fig. 15. New bandpass filter (a) layout and (b)  $L$ -shape coupling arm.

The new filter was designed for the center frequency of 1.75 GHz and fabricated on a 50-mil thickness RT/Duroid 6010.2 substrate with a relative dielectric constant  $\epsilon_r = 10.2$ . The length of the tuning stubs is  $L$  and the gap size between the tuning stubs and the ring resonator is  $s$ . The length of the feed lines is  $a = 8$  mm; the width of the microstrip line is  $w = 1.191$  mm for a 50-ohm line; the length of the coupling stubs is  $b = 18.839 + s$  mm; the gap size between the ring resonator and coupling stubs is  $g = 0.2$  mm; the length of one side of the square ring resonator is  $c = 17.648$  mm. The dimension of the ring was designed for first mode operation at the passband center frequency. The coupling gap  $g$  was selected in consideration of strong coupling and etching tolerance.

The simulation was completed using IE3D electromagnetic simulator, which gives full-wave solution using integral equations and the method of moment [35].



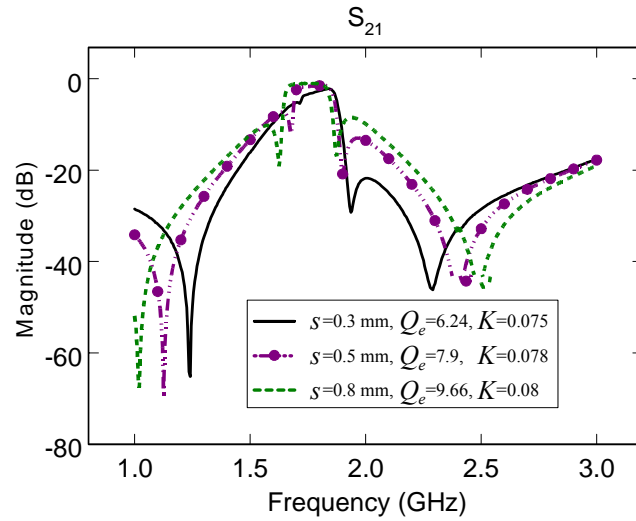
(a)



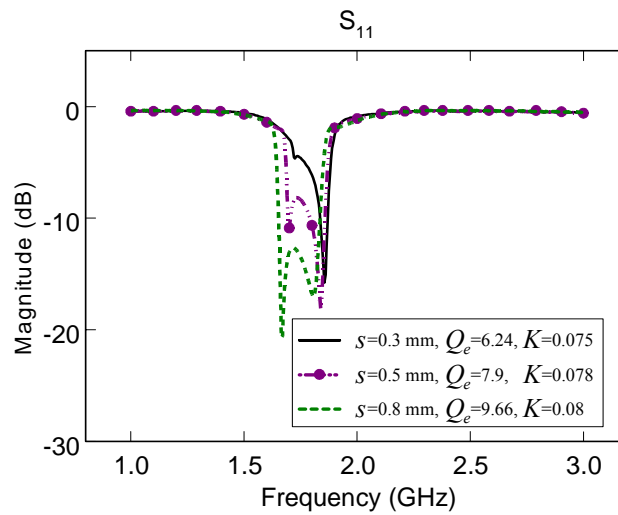
(b)

Fig. 16. Measured (a)  $S_{21}$  and (b)  $S_{11}$  by adjusting the length of the tuning stub  $L$  with a fixed gap size ( $s = 0.8$  mm).

By adjusting the length  $L$  and gap size  $s$  of the tuning stubs adequately, the coupling strength and the frequency response can be optimized. Single mode excitation (Fig. 16) or dual mode excitation (Fig. 17) can be resulted by varying  $s$  and  $L$ .



(a)



(b)

Fig. 17. Measured (a)  $S_{21}$  and (b)  $S_{11}$  by varying the gap size  $s$  with a fixed length of the tuning stubs ( $L = 13.5$  mm).

Figs. 16 and 17 show the measured results for five cases from changing the length  $L$  of tuning stubs with a fixed gap size ( $s = 0.8$  mm) and varying the gap size  $s$  with a fixed length ( $L = 13.5$ mm).

Observing the measured results in Fig. 16, two cases for  $L = 4.5$  and 9 mm with a fixed gap size only excite a single mode. The coupling between the  $L$  arms and the ring can be expressed by external  $Q$  ( $Q_e$ ) as follow: [49]:

$$Q_L = \frac{1}{\frac{2}{Q_e} + \frac{1}{Q_u}} = \frac{f_o}{(\Delta f)_{3dB}} \quad (53)$$

where  $Q_L$  is the loaded  $Q$ ,  $Q_u$  is the unloaded  $Q$  of the ring resonator,  $f_o$  is the resonant frequency, and  $(\Delta f)_{3dB}$  is the 3-dB bandwidth. The unloaded  $Q$  ( $Q_u = 137$ ) for the square ring resonator can be obtained from the measurement using the circuit shown in Fig. 18.

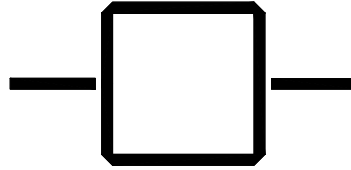


Fig. 18. A square ring resonator for the unloaded  $Q$  measurement.

From (53),  $Q_e$  is given by

$$Q_e = \frac{2Q_u Q_L}{Q_u - Q_L}. \quad (54)$$

The performance for these two single-mode ring resonators is shown in Table V.



Table V Single mode ring resonator

	Case1: $L = 4.5$ mm $s = 0.8$ mm	Case 2: $L = 9$ mm $s = 0.8$ mm
Resonant Frequency $f_o$	1.75 GHz	1.755 GHz
Insertion Loss IL	2.69 dB	0.97 dB
3 - dB Bandwidth	70 MHz	150 MHz
Loaded $Q$	25	11.7
External $Q$	61.16	25.58

On the other hand, the three cases shown in Fig. 17 by varying gap size  $s$  with a fixed length  $L = 13.5$  mm generate dual-mode characteristics. The coupling coefficient between two degenerate modes is given by [48]

$$K = \frac{f_{p2}^2 - f_{p1}^2}{f_{p2}^2 + f_{p1}^2} \quad (55)$$

where  $f_{p1}$  and  $f_{p2}$  are the resonant frequencies. In addition, the midband insertion loss  $L_A$  corresponding to  $Q_u$ ,  $Q_e$  and  $K$  can be expressed as [49]

$$L_A = 20 \log \left[ \frac{(1 + Q_e/Q_u)^2}{2KQ_e} + \frac{KQ_e}{2} \right] \text{ dB}. \quad (56)$$

The external  $Q$  can be obtained from (56) through measured  $L_A$ ,  $K$ , and  $Q_u$ . Moreover, the coupling coefficient between two degenerate modes shows three different coupling conditions. Let  $K_o = 1/Q_e + 1/Q_u$ . If the coupling coefficient satisfies  $K > K_o$ , then the coupling between two degenerate modes is overcoupled. In this overcoupled condition, the ring resonator has a hump response with a high insertion loss in the middle of the passband [19]. If  $K = K_o$ , the coupling is critically coupled. Finally, if  $K < K_o$ , the

coupling is undercoupled. For both critically coupled and undercoupled coupling conditions, there is no hump response. Also, when the coupling becomes more undercoupled, the insertion loss in the passband increases [49]. The performance for the dual-mode ring resonators is displayed in Table VI.

Observing the single-mode ring in Table V, it shows that a higher external  $Q$  produces higher insertion loss and narrower bandwidth. On the other hand, for the dual-mode ring resonator in Table VI, its insertion loss and bandwidth depend on the external  $Q$ , coupling coefficient  $K$ , and coupling conditions. For an undercoupled condition, the more undercoupled, the more the insertion loss and the narrower the bandwidth. To obtain a low insertion-loss and wide-band pass band characteristic, the single-mode ring resonator should have a low external  $Q$ , which implies more coupling periphery between the feeders and the ring resonator. Also, the dual-mode ring resonator can achieve the same performance by selecting a proper external  $Q$  and coupling coefficient  $K$  for an undercoupled coupling close to an overcoupled coupling.

Table VI Dual mode ring resonator

	Case 1: $L= 13.5$ mm $s= 0.3$ mm	Case 2: $L= 13.5$ mm $s= 0.5$ mm	Case 3: $L= 13.5$ mm $s= 0.8$ mm
Resonant Frequencies( $f_{p1}, f_{p2}$ )	(1.72,1.855) GHz	(1.7,1.84) GHz	(1.67,1.81) GHz
Coupling Coefficient $K$	0.075	0.078	0.08
External $Q$	6.24	7.9	9.66
Midband Insertion Loss IL	2.9 dB	1.63 dB	1.04 dB
3- dB Bandwidth	160 MHz	175 MHz	192.5 MHz
Coupling Condition	undercoupled	undercoupled	undercoupled

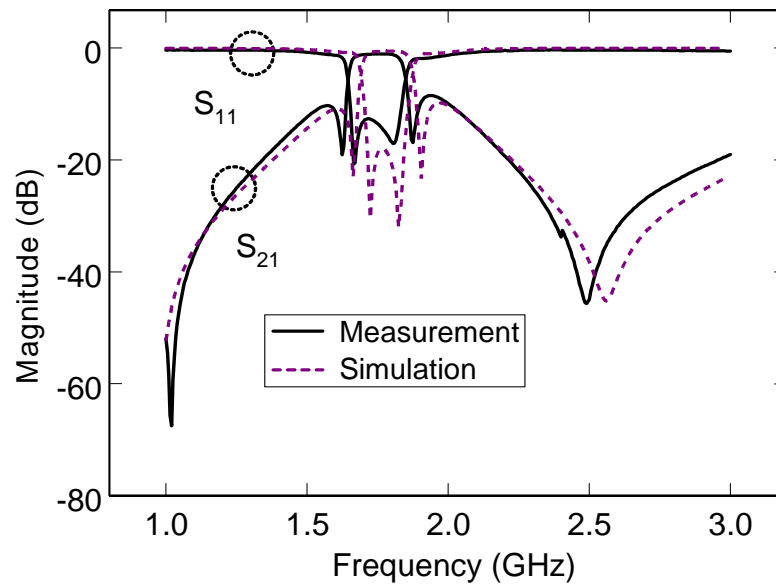


Fig. 19. Simulate and measured results for the case of  $L = 13.5$  mm and  $s = 0.8$  mm.

Fig. 19 shows the simulated and measured results for the optimized quasi-elliptic bandpass filter. It can be found that an orthogonal-feed dual-mode ring resonator produces a quasi-elliptic characteristic [14,50,51]. As seen in Fig. 15, without the tuning stubs  $L$ , the fields of the ring are unaffected and the filter exhibits a stopband at the fundamental resonant frequency [5]. With the tuning stubs, the fields of the ring are perturbed and excited a dual mode. Also, two additional transmission zeros are generated. Both transmission zeros locate on either side of the passband [5,50]. This frequency response is treated as a quasi-elliptic characteristic. In comparison of this new filter in Fig. 15 with the conventional filter, which is constructed by one-element hairpin [52], edge-coupled, and interdigital microstrips [49], the new filter can provide a quasi-elliptic characteristic with a wide bandwidth while the conventional filter can only have a Chebyshev characteristic with a narrow bandwidth.

C. *Dual-mode Bandpass Filter Using Multiple Cascaded Ring Resonators Dual-mode*

1) *Dual-mode Bandpass Filter Using Two Cascaded Ring Resonator*

Cascaded multiple ring resonators have advantages in acquiring a much narrower and shaper rejection band than the single ring resonator and many bandpass filters using multiple ring resonators are fabricated by HTS [46-48].

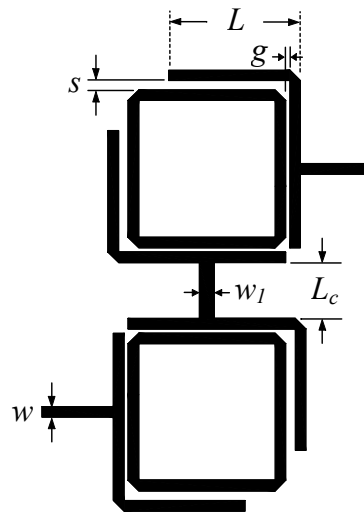


Fig. 20. Layout of the filter using two resonators with  $L$ -shape coupling arms.

Fig. 20 illustrates the circuit composed of two ring resonators. This bandpass filter was built based on the  $L = 13.5$  mm and  $s = 0.8$  mm case of the single ring resonator of Fig. 20. Each filter section has identical dimensions as the single ring resonator. A short transmission line  $L_c$  of 6.2 mm with a width  $w_1 = 1.691$ mm connects to the coupling stubs to link the two ring resonators. The energy transfers from one ring resonator through the coupling and tuning stubs (or a  $L$ -shape arm) and the short transmission line to another ring resonator. Observing the configuration for the  $L$ -shape and the short transmission line  $L_c$  in Fig. 20, it not only perturbs the ring resonator but also can be treated as a resonator.

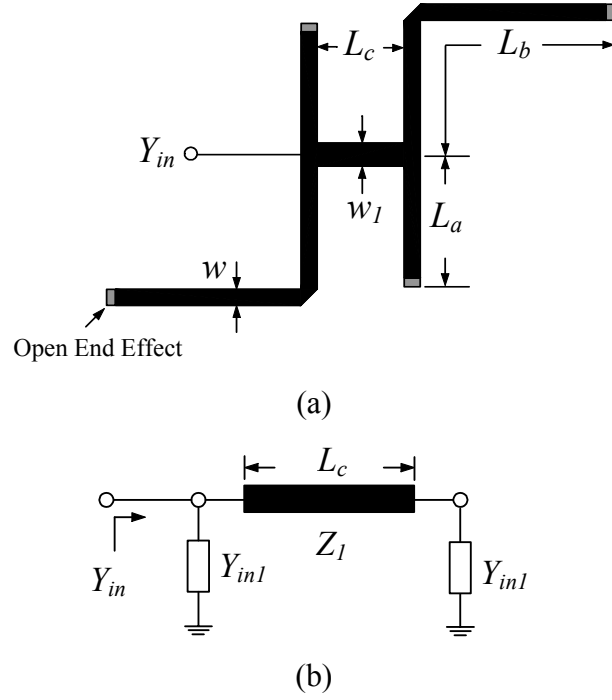


Fig. 21. Back-to-back  $L$ -shape resonator (a) layout and (b) equivalent circuit. The lengths  $L_a$  and  $L_b$  include the open end effects.

Considering this type resonator in Fig. 21(a), it consists a transmission line  $L_c$  and two parallel-connected open stubs. Its equivalent circuit is shown in Fig. 21(b). The input admittance  $Y_{in}$  is given by

$$Y_{in} = Y_{in1} + Y_1 \left[ \frac{Y_{in1} + jY_1 \tan(\beta L_c)}{Y_1 + jY_{in1} \tan(\beta L_c)} \right] \quad (57)$$

where  $Y_{in1} = jY_o[\tan(\beta L_a) + \tan(\beta L_b)]$ ,  $Y_1 = 1/Z_l$ ,  $Y_o = 1/Z_o$ , and  $\beta$  is the phase constant.  $Y_1$  is the characteristic admittance of the transmission line  $L_c$ , and  $Y_o$  is the characteristic admittances of the transmission lines  $L_a$ , and  $L_b$ . Letting  $Y_{in} = 0$ , the resonant frequencies of the resonator can be predicted. In Fig. 21, the resonant frequencies of the resonator are calculated as  $f_{o1} = 1.067$ ,  $f_{o2} = 1.654$  and  $f_{o3} = 2.424$  GHz within 1-3 GHz. To verify the resonant frequencies, an end-to-side coupling circuit is built as shown in

Fig. 22. Also, the measured resonant frequencies can be found as  $f_{mo1} = 1.08$ ,  $f_{mo2} = 1.655$ , and  $f_{mo3} = 2.43$  GHz, which show a good agreement with calculated results.

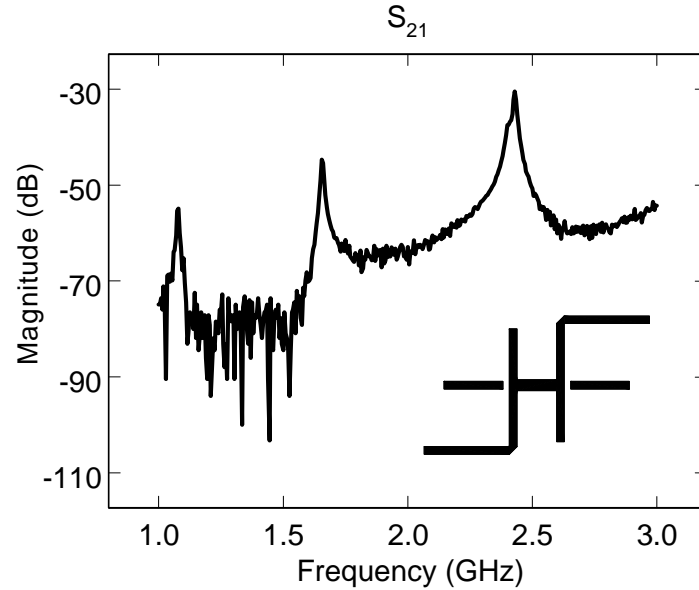


Fig. 22. Measured  $S_{21}$  for the back-to-back  $L$ -shape resonator.

Inspecting the frequency responses in Figs. 22 and 23, the spike at  $f_{mo3} = 2.43$  GHz is suppressed by the ring resonators and only one spike appears at low frequency ( $f_{mo1} = 1.08$  GHz) with a high insertion loss, which does not influence the filter performance. Furthermore, the resonant frequency ( $f_{mo2} = 1.655$  GHz) of the resonator in Fig. 22 couples with the ring resonators. By changing the length  $L_c$ , the resonant frequencies will move to different locations. For a shorter length  $L_c$ , the resonant frequencies move to higher frequency and for a longer length  $L_c$ , the resonant frequencies shift to lower frequency. Considering the filter performance, a proper length  $L_c$  should be carefully chosen. The filter has an insertion loss of 1.63 dB in the passband with a 3-dB bandwidth of 155 MHz.

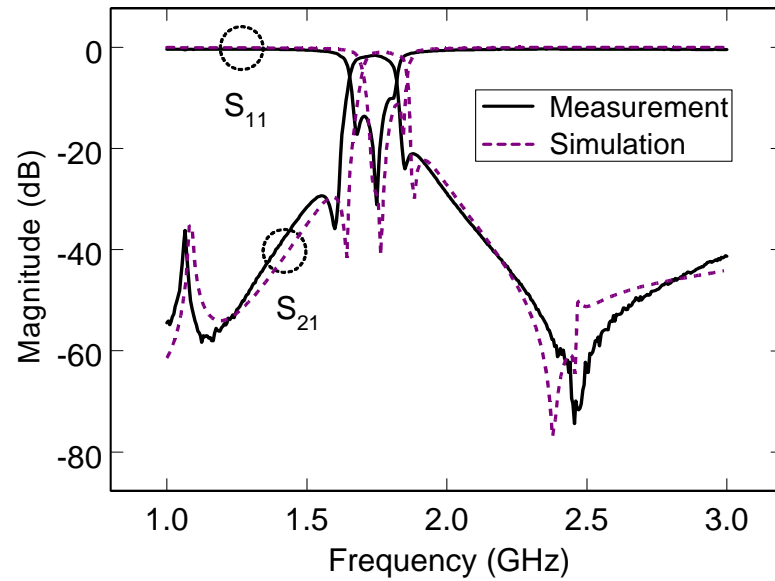


Fig. 23. Simulated and measured results for the filter using two resonators with  $L$ -shape coupling arms.

## 2) *Dual-mode Bandpass Filter Using Three Cascaded Ring Resonators*

Fig. 24 illustrates the filter using three cascaded ring resonators. Any two of three resonators are linked by a  $L$ -shape arm with a short transmission line  $L_c$  of 6.2mm with a width  $w_l = 1.691$  mm. The simulated and measured results are shown in Fig. 25. The filter has an insertion loss of 2.39 dB in the passband with a 3-dB bandwidth of 145 MHz. Table VII summarizes the filter performance with one, two and three ring resonators.

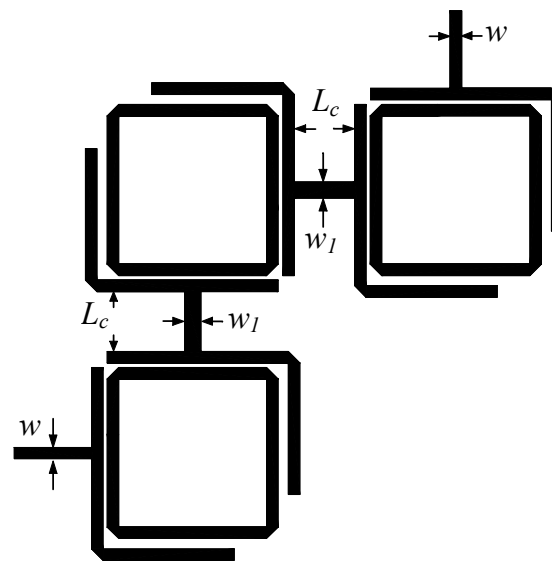


Fig. 24. Layout of the filter using three resonators with  $L$ -shape coupling arms.

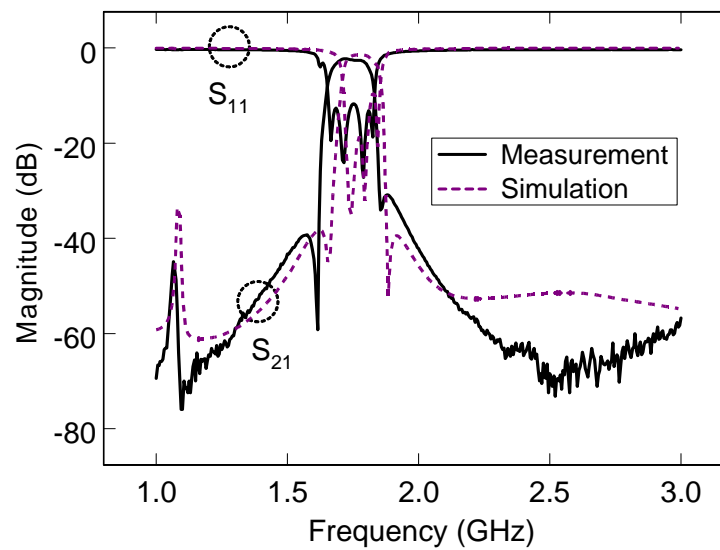


Fig. 25. Simulated and measured results for the filter using three resonators with  $L$ -shape coupling arms.



Table VII Filter performance

	One ring Fig. 19	Two rings Fig. 23	Three rings Fig. 25
Minimum S21	1.04 dB	1.63 dB	2.39 dB
Frequency Range for S11 < 10 dB	1.655 to 1.835 GHz	1.665 to 1.81 GHz	1.685 to 1.83 GHz
3 - dB Bandwidth	192.5 MHz	155 MHz	145 MHz
Fractional Bandwidth	11 %	8.9 %	8.45 %
Band Rejection	Better than 10 dB	Better than 20 dB	Better than 30 dB

#### D. Conclusions

A novel type of microwave dual-mode filter using square ring resonators with an enhanced  $L$ -shape coupling arm is proposed. By changing the length of tuning stubs and gap sizes between tuning stubs and ring resonator, the insertion loss and frequency response of the filter can be optimized. To acquire a low insertion-loss and wide-band pass band characteristic, the single-mode ring resonator should have stronger coupling between the feeders and the ring resonator. Also, the dual-mode ring resonator should choose a proper external  $Q$  and coupling coefficient  $K$  to achieve the low insertion-loss and wide-band pass band characteristics. Filters using cascaded ring resonators provide a sharp rejection band and narrow passband bandwidth with quasi-elliptic characteristics.

## CHAPTER V

SLOW-WAVE BANDPASS FILTERS USING RING OR STEPPED IMPEDANCE  
HAIRPIN RESONATORS\**A. Introduction*

Microstrip ring and stepped impedance hairpin resonators have many attractive features and can be used in satellites, mobile phones and other wireless communication systems. The main advantages of the resonators are their compact size, easy fabrication, narrow bandwidth and low radiation loss. Therefore, the resonators are widely used in the design of filters, oscillators, and mixers [5,53].

Some of the bandpass filters that use the ring resonator utilize the dual-mode characteristic to achieve a sharp cut-off frequency response [14]. However, the filters use perturbation notches or stubs that make their frequency response sensitive to fabrication uncertainties [14]. In addition, bandpass filters that use using parallel- or cross-coupling ring resonators to produce Chebyshev- or elliptic-function characteristics [54,55] suffer from high insertion loss. Recently, the ring resonator filters using high temperature superconductor (HTS) and micromachined circuit technologies have demonstrated low insertion loss and a sharp cut-off frequency response, but at the expense of high fabrication costs [56].

The hairpin resonator was first introduced to reduce the size of the conventional parallel-coupled half-wavelength resonator with subsequent improvements made to reduce its size [53,57]. Beyond the advantage of the compact size, the spurious frequencies of the stepped impedance hairpin resonator are shifted from the integer

---

\*Reprinted with permission from (complete publication information) “Slow-wave bandpass filters using ring or stepped impedance hairpin resonators” by Lung-Hwa Hsieh and Kai Chang, 2002. *IEEE Trans. Microwave Theory Tech.*, vol. 50, pp. 1795-1800. © 2004 by the IEEE.

multiples of the fundamental resonant frequency due to the effect of the capacitance-load coupled lines. Also, compact size bandpass filters using stepped impedance hairpin resonators with parallel- or cross-coupling structures have shown high insertion loss [52,58]. An interesting slow-wave bandpass filter has been reported [59] that uses capacitively loaded parallel- and cross-coupled open-loop ring resonators. This filter also shows high insertion loss.

In this chapter, slow-wave bandpass filters using a microstrip line periodically loaded by ring or stepped impedance hairpin resonators are introduced. By using the parallel and series resonance characteristics of the resonators, the slow-wave periodic structures perform as a bandpass filter. The new slow-wave bandpass filters, designed at fundamental resonant frequency of the resonators, also are different from conventional slow-wave filters, which utilize higher order modes to build up a bandpass filter with a wide passband [60] or to provide lowpass or bandstop features [61,62]. In comparison with bandpass filters that use parallel- and cross-coupled resonators with coupling gaps between the resonators, these new slow-wave bandpass filters show lower insertion loss at similar resonant frequencies [52,54,55,58]. This is an important finding since the new filter structure uses more conductor than the parallel- and cross-coupled structures. This implies that the new filter topology significantly reduces the insertion loss caused in parallel- and cross-coupled bandpass structures by eliminating coupling gaps between resonators. The performance of the new slow-wave filters is evaluated by experiment and calculation with good agreement.

### *B. Analysis of the Slow-Wave Periodic Structure*

Fig. 26(a) illustrates a conventional slow-wave periodic structure. The transmission line is periodically loaded with identical open stub elements. Each unit element includes a length of  $d$  transmission line with a length of  $l$  open stub, where  $Z_{inl}$  is the input impedance looking into the open stub. The conventional slow-wave periodic structure usually works as a lowpass or stopband filter [61,62]. Also, using higher order modes, the conventional slow-wave periodic structure can act as a wide band bandpass filter, by

constructing two consecutive stopbands close to the passband [60]. Considering the slow-wave periodic structure in Fig. 26(b), a loading impedance  $Z_L$  is connected at the end of the open stub. The input impedance  $Z_{in2}$  is given by

$$Z_{in2} = Z_o \frac{Z_L + jZ_o \tan(\beta l)}{Z_o + jZ_L \tan(\beta l)} \text{ for lossless line} \quad (58)$$

where  $Z_o$  and  $\beta$  are the characteristic impedance and phase constant of the open stub, respectively.

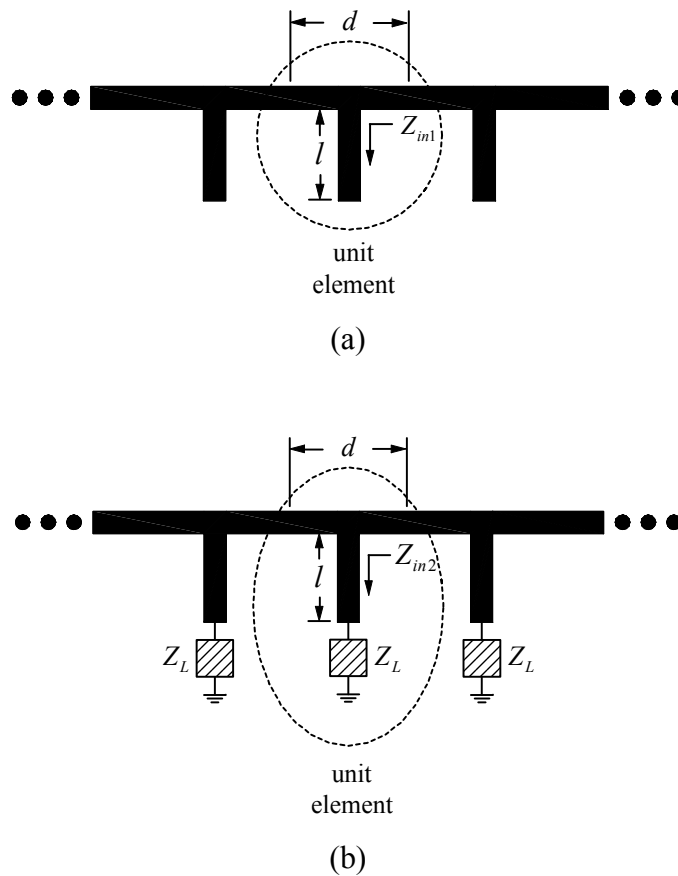


Fig. 26. Slow-wave periodic structure (a) conventional type and (b) with loading  $Z_L$  at open end.

If  $Z_L = \infty$  or 0 with a very small value of  $\tan(\beta l)$ , the input impedance  $Z_{in2} \rightarrow \infty$  or 0, respectively. Under these cases, the slow-wave periodic structure loaded by  $Z_{in2}$  in Fig. 26(b) provides passband ( $Z_{in2} \rightarrow \infty$ ) and stopband ( $Z_{in2} \rightarrow 0$ ) characteristics. For example, the conventional capacitance-load Kuroda-identity periodic structure is the case of  $Z_L = \infty$  with  $l = \lambda_g / 8$  [38].

Fig. 27 shows lossless parallel and series resonant circuits. At resonance, the input impedance  $Z_{LC}$  of the parallel and series resonant circuits is  $\infty$  and 0, respectively.

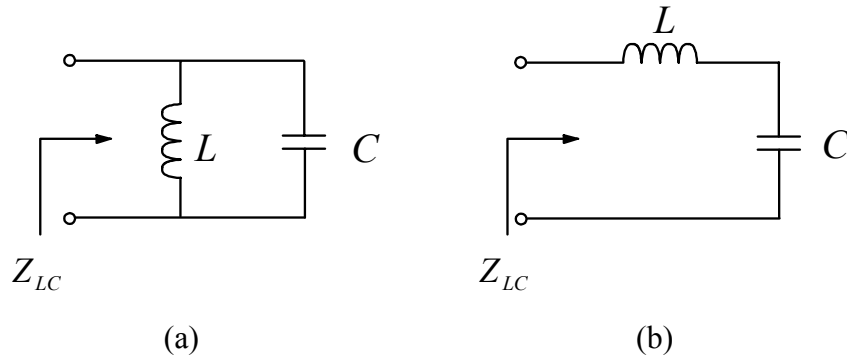


Fig. 27. Lossless (a) parallel and (b) series resonant circuits.

The input impedance  $Z_{LC}$  of the resonant circuits can act as the loading impedance  $Z_L$  in Fig. 26(a) for the passband and stopband characteristics of a slow-wave periodic structure. In practice, for the high  $Q$  ring and hairpin resonators, the input impedance of the resonators shows very large and small values at parallel and series resonant frequencies, respectively. Thus, a slow-wave periodic structure loaded by ring or hairpin resonators with two series resonant frequencies close to a parallel resonant frequency [5,53] can be designed for a bandpass filter at fundamental mode.

The key point behind this new slow-wave filter topology is that both the series and the parallel resonances of the loading circuit are used to achieve bandpass characteristics. The approach can, in fact, be interpreted as using the stop bands of two

series resonances in conjunction with the pass band of a parallel resonance to achieve a bandpass frequency response. It is noted, however, that in some cases, undesired pass bands below and above the main pass band may require a high pass or band pass section to be used in conjunction with this approach.

### C. *Slow-Wave Bandpass Filters Using Square Ring Resonators*

Fig. 28 shows a transmission line loaded by a square ring resonator with a line-to-ring coupling structure and its simple equivalent circuit, where  $Z_{in3}$  is the input impedance looking into the transmission line  $l_b$  toward the ring resonator with the line-to-ring coupling.

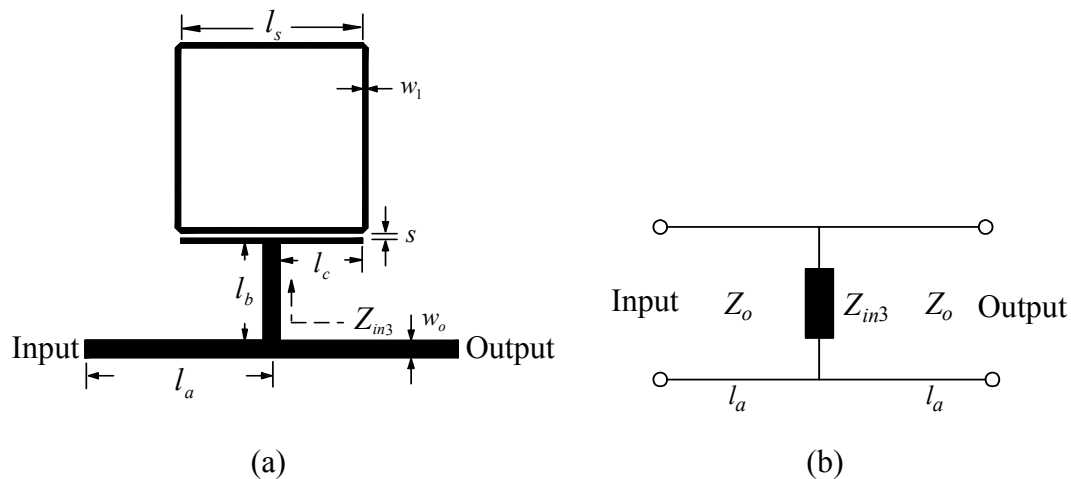


Fig. 28. Slow-wave bandpass filter using one ring resonator with one coupling gap (a) layout and (b) simplified equivalent circuit.

As seen in Fig. 29(a), the coupling structure includes the coupling line, one side of the square ring resonator and a coupling gap. This coupling structure can be treated as symmetrical coupled lines [63]. The coupling gap between the symmetrical coupled lines is modeled as a capacitive L-network as shown in Fig. 29(b) [37].

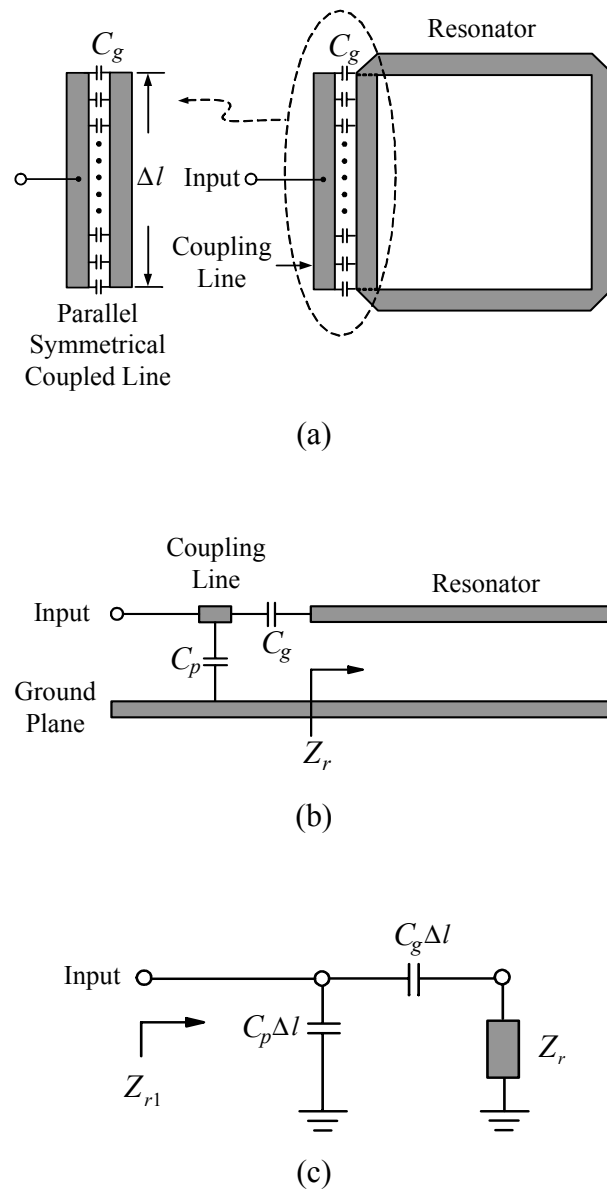


Fig. 29. Line-to-ring coupling structure (a) top view (b) side view and (c) equivalent circuit.

$C_g$  is the gap capacitance per unit length, and  $C_p$  is the capacitance per unit length between the strip and ground plane. These capacitances,  $C_g$  and  $C_p$ , can be found from the even- and odd-mode capacitances of symmetrical coupled lines [64]. Fig. 29(c)

shows the equivalent circuit of the capacitive L-network, where the input impedance of the ring resonator  $Z_r$  can be obtained from [37]. The input impedance  $Z_{r1}$  looks into the line-to-ring coupling structure toward the ring resonator. The input impedance  $Z_{in3}$  is

$$Z_{in3} = \frac{Z_{r1} + jZ_o \tan(\beta l_b)}{Z_o + jZ_{r1} \tan(\beta l_b)} \quad (59)$$

where  $Z_{r1} = (Z_r + Z_g) \parallel Z_p$ ,  $Z_g = 1/j\omega C_g \Delta l$ ,  $Z_p = 1/j\omega C_p \Delta l$ , and  $\omega$  is the angular frequency. The parallel ( $f_p$ ) and series ( $f_s$ ) resonances of the ring resonator can be obtained by setting

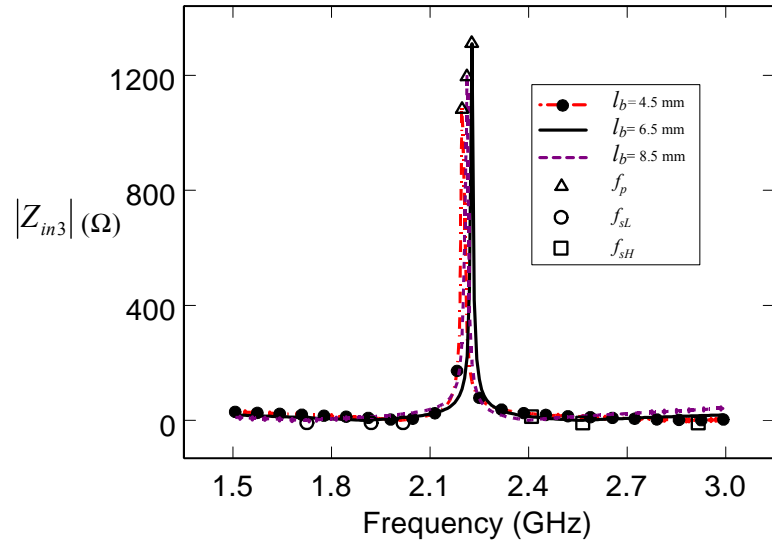
$$|Y_{in3}| = |1/Z_{in3}| \cong 0 \text{ and } |Z_{in3}| \cong 0. \quad (60)$$

The frequency response of the ring circuit can be calculated using the equivalent circuit in Fig. 28(b). The  $ABCD$  matrix of the ring circuit is

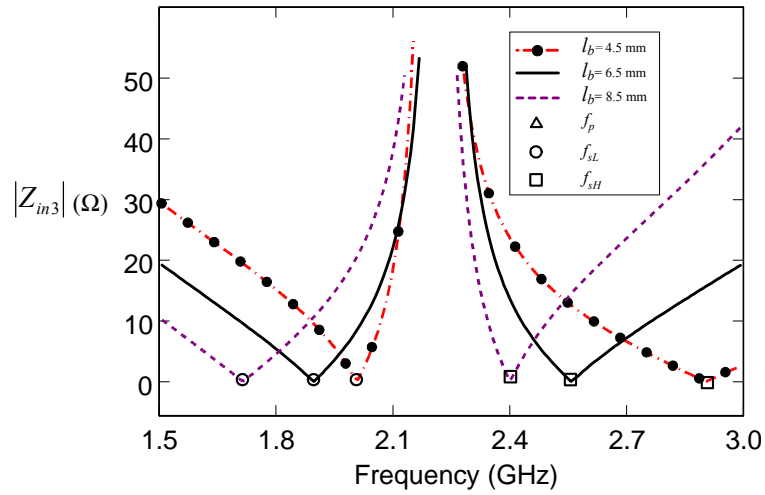
$$\begin{aligned} \begin{bmatrix} A & B \\ C & D \end{bmatrix} &= \begin{bmatrix} \cos(\beta l_a) & jZ_o \sin(\beta l_a) \\ jY_o \sin(\beta l_a) & \cos(\beta l_a) \end{bmatrix} \begin{bmatrix} 1 & 0 \\ Y_{in3} & 1 \end{bmatrix} \begin{bmatrix} \cos(\beta l_a) & jZ_o \sin(\beta l_a) \\ jY_o \sin(\beta l_a) & \cos(\beta l_a) \end{bmatrix} \\ &= \begin{bmatrix} 1 - 2\sin^2(\beta l_a) + jZ_o Y_{in3} \sin(\beta l_a) \cos(\beta l_a) & \\ Y_{in3} \cos^2(\beta l_a) + j2Y_o \sin(\beta l_a) \cos(\beta l_a) & \\ -Z_o^2 Y_{in3} \sin^2(\beta l_a) + j2Z_o \sin(\beta l_a) \cos(\beta l_a) & \\ 1 - 2\sin^2(\beta l_a) + jZ_o Y_{in3} \sin(\beta l_a) \cos(\beta l_a) & \end{bmatrix} \end{aligned} \quad (61)$$

where  $Y_o = 1/Z_o$ . Using  $Y_{in3}(f_p)$  and  $Z_{in3}(f_s)$ , the passband and stopband of the ring circuit can be obtained by calculating  $S_{11}$  and  $S_{21}$  from the  $ABCD$  matrix in (61).





(a)



(b)

Fig. 30. Variation in input impedance  $|Z_{in3}|$  for different lengths of  $l_b$  showing (a) parallel and series resonances and (b) an expanded view for the series resonances.

The ring circuit was designed at the center frequency of 2.4 GHz and fabricated on a RT/Duroid 6010.5 substrate with a thickness  $h = 50$  mil and a relative dielectric constant  $\epsilon_r = 10.5$ . The dimensions of the filter are  $l_s = 12.07$  mm,  $s = 0.2$  mm,  $l_a = 12.376$  mm,  $l_b = 6.5$  mm,  $w_o = 1.158$  mm, and  $w_l = 0.3$  mm. These parameter values are synthesized

from the design equations using numerical optimization to construct a bandpass filter with attenuation poles centered at  $\pm 330$  MHz about the parallel resonant frequency. Fig. 30(a) shows the calculated input impedance  $Z_{in3}$  with parallel and two series resonances of the ring resonator at different lengths of  $l_b$ . The parallel ( $f_p$ ), lower ( $f_{sL}$ ) and higher ( $f_{sH}$ ) series resonances corresponding to the passband and stopband of the ring circuit in Fig. 28 are denoted by  $\Delta$ ,  $\circ$ , and  $\square$ , respectively. By adjusting the length of  $l_b$  properly, the parallel resonance can be centered between two series resonances. Also, Fig. 30(b) shows an extended view for series resonances. The measured and calculated frequency response of the ring circuit is illustrated in Fig. 31.

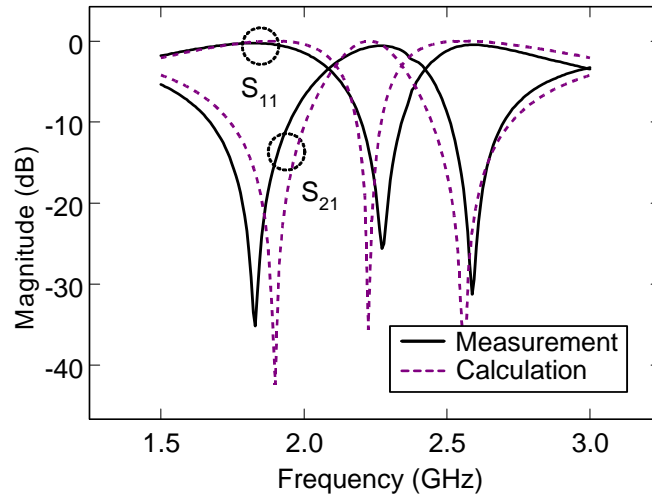


Fig. 31. Measured and calculated frequency response for the slow-wave bandpass filter using one square ring resonator.

The filter has a fractional 3-dB bandwidth of 15.5%. The insertion and return losses are 0.53 dB and 25.7dB at 2.3GHz, respectively. Two attenuation poles are at 1.83 and 2.59 GHz with attenuation level of 35.2 and 31.3 dB, respectively. The measured unloaded  $Q$  of the closed-loop ring resonator is 122.

To improve the passband and rejection, a slow-wave bandpass filter using three ring resonators has also been built. As seen in Fig. 32, the transmission line is loaded

periodically by three ring resonators, where  $Z_{in4}$  is the input impedance looking into  $l_e$  toward the ring. The filter uses the same dimensions as the filter with a single ring resonator in Fig. 28, but with the transmission lengths  $l_d = 15.686$  mm and  $l_e = 5.5$  mm, which are optimized by the calculation equations to obtain wider stop bands than the filter in Fig. 28.

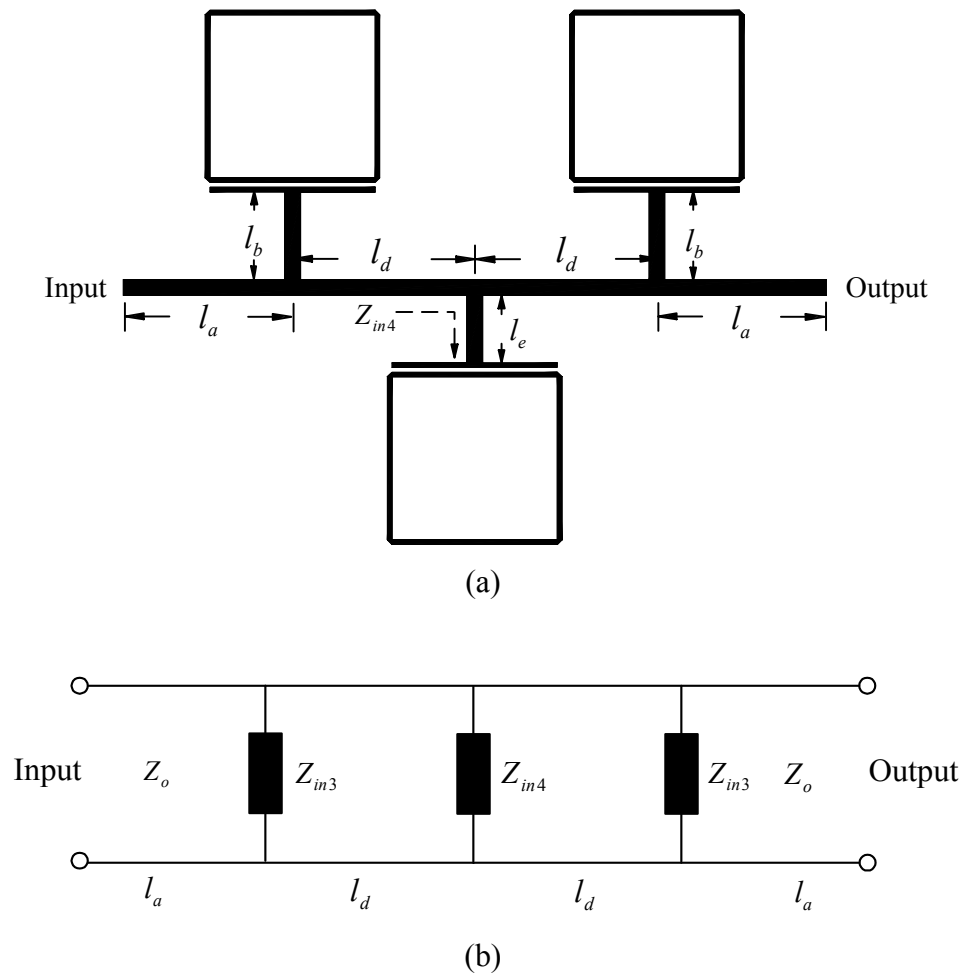


Fig. 32. Slow-wave bandpass filter using three ring resonators (a) layout and (b) simplified equivalent circuit.

The frequency response of the filter can be obtained from  $ABCD$  matrix of the equivalent circuit in Fig. 32(b). Fig. 33 illustrates the measured and calculated results. The filter with an elliptic-function characteristic has a 3-dB fractional bandwidth of 8.5% and a pass band from 2.16 to 2.34 GHz with return loss better than 10 dB. The maximum insertion loss in the pass band is 1.45 dB with a ripple of  $\pm 0.09$  dB. In addition, the two stop bands exhibit a rejection level larger than 50 dB within 1.76-2 GHz and 2.52-2.7 GHz. Observing the frequency response of the filters in Figs. 31 and 33, the differences between the calculated and measured results are due to the use of a lossless calculation model.

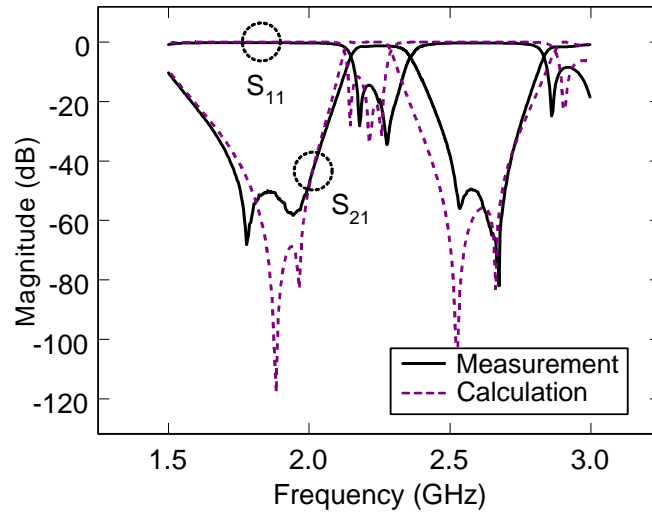


Fig. 33. Measured and calculated frequency response for slow-wave bandpass filter using three square ring resonators.

#### D. *Slow-Wave Bandpass Filters Using Stepped Impedance Hairpin Resonators*

The hairpin has parallel and series resonance characteristics and can also be used as the loading impedance  $Z_L$  in the slow-wave periodic structure of Fig. 26(b) to construct a bandpass response. Fig. 34 shows the filter using one stepped impedance hairpin resonator and its simple equivalent circuit, where  $Z_{in5}$  is the input impedance looking

into  $l_g$  toward the resonator.  $Z_{r2}$ , the input impedance of the stepped impedance hairpin resonator, can be obtained from [53]. Similar to the ring circuit in Fig. 28, the frequency response of the hairpin circuit can also be obtained from the  $ABCD$  matrix of the equivalent circuit in Fig. 34(b). The filter was designed at the center frequency of 2 GHz and fabricated on a RT/Duroid 6010.2 substrate with thickness  $h = 25$  mil and a relative dielectric constant  $\epsilon_r = 10.2$ . The parameters of the filter are shown as follows:  $l_g = 3$  mm,  $l_l = 3$  mm,  $l_2 = 3.35$  mm,  $l_3 = 2.5$  mm,  $l_4 = 2.596$  mm,  $w_2 = 0.591$  mm,  $w_3 = 1.425$  mm,  $w_4 = 0.3$  mm,  $g = 0.25$  mm,  $l_f = 12.345$  mm and  $l_h = 8.9$  mm.

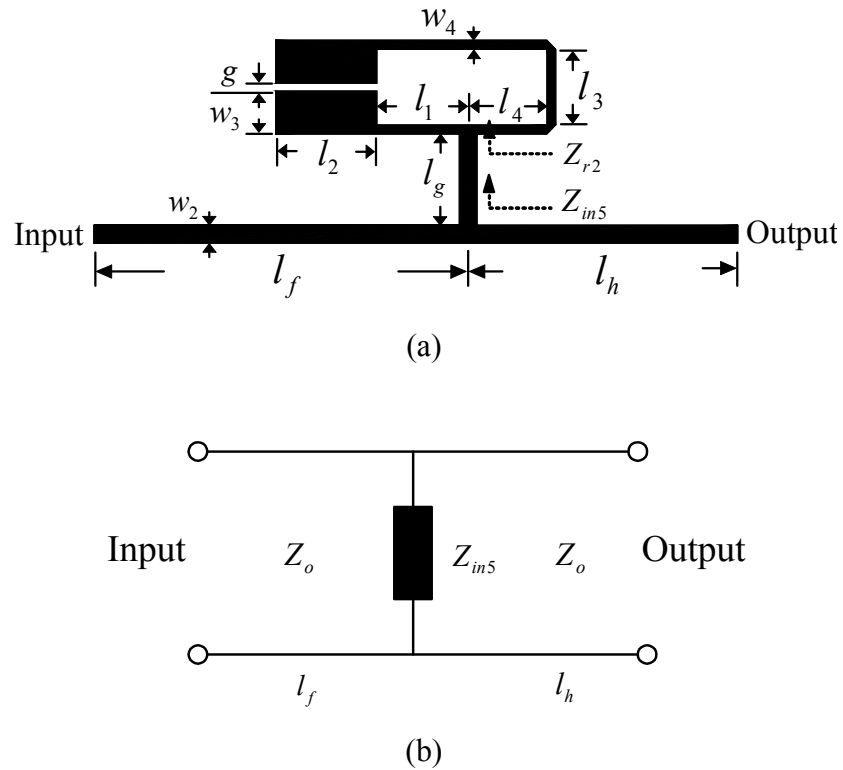


Fig. 34. Slow-wave bandpass filter using one stepped impedance hairpin resonator (a) layout and (b) simplified equivalent circuit.

These parameter values are synthesized from the design equations, similar to (61), using numerical optimization to build a bandpass filter with attenuation poles centered at  $\pm 530$  MHz about the parallel resonant frequency. Calculated and measured results similar to Figs. 30 and 31 have been obtained. Also, by adjusting the length of  $l_g$  properly, the two series resonances can be centered about the parallel resonance when  $l_g = 3$  mm.

Fig. 35 shows the transmission line loaded periodically by six stepped impedance hairpin resonators. The filter uses the same dimensions as the filter using a single hairpin resonator in Fig. 34, but with the transmission length  $l_k = 14.755$  mm, which is optimized by the calculation equations for maximum rejection.

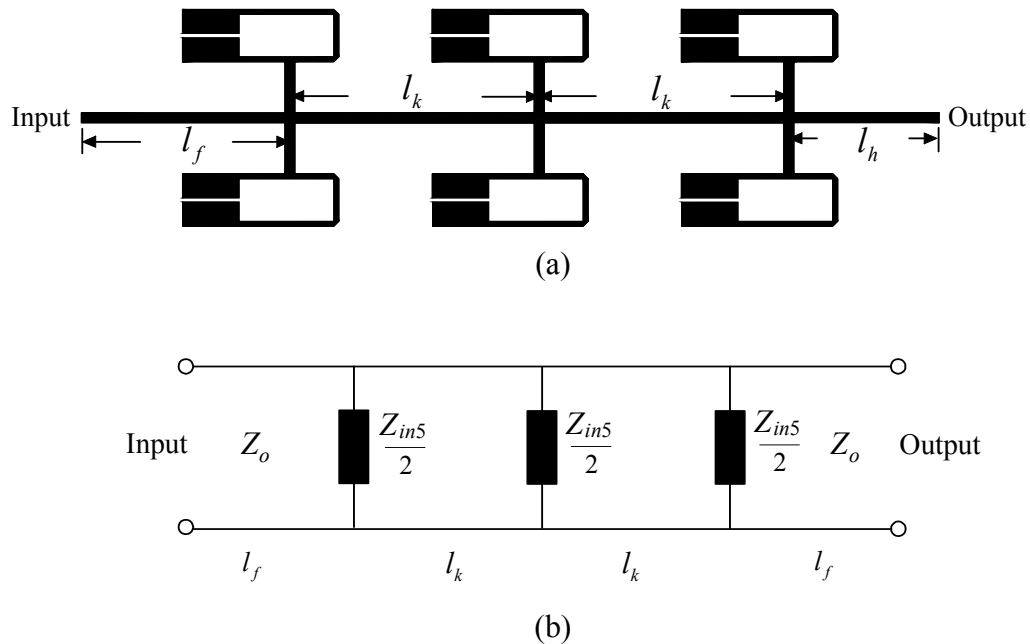


Fig. 35. Slow-wave bandpass filter using six stepped impedance hairpin resonators (a) layout and (b) simplified equivalent circuit.

Fig. 36 illustrates the measured and calculated results. The filter with a Chebyshev characteristic has a 3-dB fractional bandwidth of 8.55%. A pass band is from 1.84 to

1.98GHz with a return loss better than 10 dB. The maximum insertion loss in the pass band is 1.82 dB with a ripple of  $\pm 0.06$  dB. In addition, two stop bands exhibit a rejection level greater than 60 dB within 1.32-1.57 GHz and 2.38-2.76 GHz. The measured unloaded  $Q$  of the stepped impedance hairpin resonator is 146. Due to the use of the lossless model for calculation, these calculated responses show small differences from measured results.

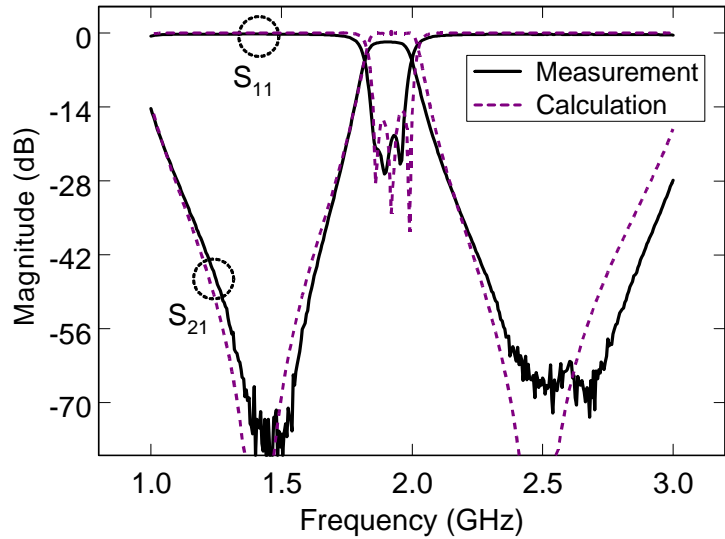


Fig. 36. Measured and calculated frequency response for slow-wave bandpass filter using six stepped impedance hairpin resonators.

### E. Conclusions

Novel slow-wave bandpass filters using a microstrip line periodically loaded with ring or stepped impedance hairpin resonators are proposed. By using the parallel and series resonance characteristics of the resonators, the new slow-wave periodic structures behave as bandpass filters. The new filters with a narrow passband designed at the fundamental mode of the resonators are different from the conventional slow-wave filters. Furthermore, the new filters have lower insertion loss than those of filters using

parallel- or cross-coupled ring and stepped impedance hairpin resonators. The filters have been investigated by experiment and calculation with good agreement.



## CHAPTER VI

TUNABLE MICROSTRIP BANDPASS FILTERS WITH TWO TRANSMISSION  
ZEROS\**A. Introduction*

The characteristics of compact size, high selectivity, and low insertion loss for modern microwave filters are highly required in the next generation of mobile and satellite communication systems. To achieve the high selectivity characteristic, Levy introduced filters using cross-coupled structure [65]. The cross coupling between nonadjacent resonators creates transmission zeros that improve the skirt rejection of the microstrip filters [66]. However, microstrip filters using the cross-coupled structure need at least four resonators and show a high insertion loss [66,67]. Recently, microstrip bandpass filters were proposed that used hairpin resonators with asymmetric input and output feed lines tapping on the first and the last resonators to obtain two transmission zeros lying on either side of the passband [67]. In comparison with the cross-coupled filter [66,67], the filter using two resonators shown in this chapter can also provide a sharp cut-off frequency response but has lower insertion loss due to less conductor losses and fewer coupling gaps. However, [67] only shows a special case of two hairpin resonators with two asymmetric feed lines tapped at the center. Thus, the locations of two transmission zeros are at the fundamental and higher odd mode resonances. Hairpin filters with tunable transmission zeros using impedance transformers tapped on the resonators were later reported in [68]. Furthermore, [67] did not discuss the variation in the coupling between the resonators due to the placement of the tapping positions of the

---

\*Reprinted with permission from (complete publication information) “Tunable microstrip bandpass filters with two transmission zeros” by Lung-Hwa Hsieh and Kai Chang, 2003. *IEEE Trans. Microwave Theory Tech.*, vol. 51, pp. 520- 525. © 2004 by the IEEE.

asymmetric feed lines. The coupling conditions between resonators are very important for a filter design.

In this chapter, a simple transmission-line model is used to calculate the locations of the two transmission zeros corresponding to the tapping positions of the asymmetric and symmetric feed lines. The coupling effects due to the tapping positions of the asymmetric feed lines are also discussed. This model makes it possible to accurately design cascaded bandpass filters to obtain high selectivity and excellent out-of-band rejection. A filter using four cascaded resonators shows a better rejection than the cross-coupled filters using four resonators. The measured performance of the cascaded filter shows good agreement with the new theory. Moreover, the passband tuning is demonstrated using a piezoelectric transducer.

### B. Analysis of Filters with Asymmetric and Symmetric Tapping Feed Lines

Fig. 37 shows the configuration of the filter using two hairpin resonators with asymmetric feed lines tapping the resonators. The input and output feed lines divide the resonators into two sections of  $l_1$  and  $l_2$ . The total length of the resonator is  $l = l_1 + l_2 = \lambda_g / 2$ , where  $\lambda_g$  is the guided-wavelength at fundamental resonance. The coupling between the two open ends of the resonators is simply expressed by the gap capacitance  $C_{s1}$  [67,69].

Inspecting Fig. 37, the whole circuit represents a shunt circuit, which consists of upper and lower sections. Each section is composed of  $l_1$ ,  $l_2$ , and  $C_{s1}$ . The  $ABCD$  matrixes for the upper and lower sections of the lossless shunt circuit are

$$\begin{bmatrix} A & B \\ C & D \end{bmatrix}_{upper} = M_1 M_2 M_3 \quad (62a)$$

$$\begin{bmatrix} A & B \\ C & D \end{bmatrix}_{lower} = M_3 M_2 M_1 \quad (62b)$$

with  $M_1 = \begin{bmatrix} \cos \beta l_1 & jz_o \sin \beta l_1 \\ jy_o \sin \beta l_1 & \cos \beta l_1 \end{bmatrix}$ ,  $M_2 = \begin{bmatrix} 1 & z_c \\ 0 & 1 \end{bmatrix}$ , and  $M_3 = \begin{bmatrix} \cos \beta l_2 & jz_o \sin \beta l_2 \\ jy_o \sin \beta l_2 & \cos \beta l_2 \end{bmatrix}$

where  $\beta$  is the propagation constant,  $z_c = 1/j\omega C_{s1}$  is the impedance of the gap capacitance  $C_{s1}$ ,  $\omega$  is the angular frequency,  $z_o = 1/y_o$  is the characteristic impedance of the resonator. The  $Y$  parameters for this shunt circuit can be obtained by adding the upper- and the lower-section  $Y$ -parameters, which follow from (62a) and (62b), respectively. The  $S_{21}$  of the circuit can then be calculated from the total  $Y$ -parameters and is expressed as

$$S_{21} = \frac{j4 \left( z_o \sin \beta l - \frac{\cos \beta l_1 \cos \beta l_2}{\omega C_{s1}} \right) Y_L}{\left[ 2 \cos \beta l + \frac{y_o \sin \beta l}{\omega C_{s1}} + j \left( z_o \sin \beta l - \frac{\cos \beta l_1 \cos \beta l_2}{\omega C_{s1}} \right) Y_L \right]^2 - 4} \quad (63)$$

where  $Y_L$  is the load admittance. Comparing (62)-(63) with (12), (13), and (16) in [55], (12), (13), and (16) in [68] only present a special case of the two hairpin resonators with two asymmetric feed lines tapped at the center.

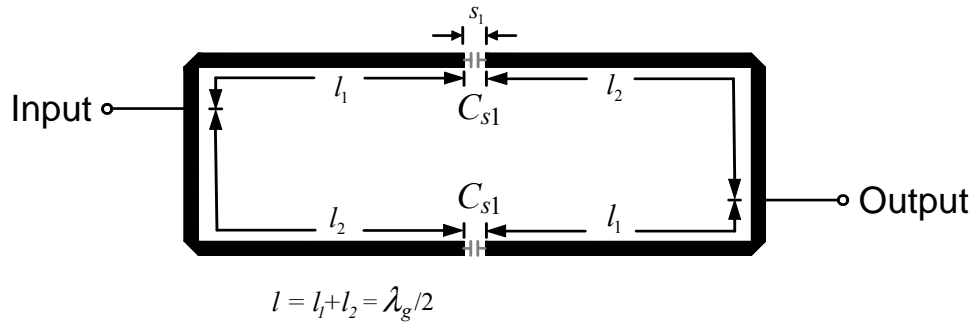


Fig. 37. Configuration of the filter using two hairpin resonators with asymmetric tapping feed lines.

Equations (62) and (63) given here are more general for the asymmetric feed lines tapped at arbitrary positions on the resonators. The transmission zeros can be found by letting  $S_{21} = 0$ , namely

$$z_o \sin \beta l - \frac{\cos \beta l_1 \cos \beta l_2}{\omega C_{s1}} = 0. \quad (64)$$

For a small  $C_{s1}$ , (64) can be approximated as

$$\cos \beta l_1 \cos \beta l_2 \cong 0. \quad (65)$$

Inspecting (65), it shows the relation between the transmission zeros and the tapping positions. Substituting  $\beta = \frac{2\pi f \sqrt{\epsilon_{eff}}}{c}$  into (65), the transmission zeros corresponding to the tapping positions are

$$f_1 = \frac{nc}{4l_1 \sqrt{\epsilon_{eff}}} \text{ and } f_2 = \frac{nc}{4l_2 \sqrt{\epsilon_{eff}}} \quad n = 1, 3, 5... \quad (66)$$

where  $f$  is the frequency,  $\epsilon_{eff}$  is the effective dielectric constant,  $n$  is the mode number,  $c$  is the speed of light in free space, and  $f_1$  and  $f_2$  are the frequencies of the two transmission zeros corresponding to the tapping positions of the lengths of  $l_1$  and  $l_2$  on the resonators. At the transmission zeros,  $S_{21} = 0$  and there is maximum rejection. Fig. 38 shows the measured results for different tapping positions on the hairpin resonators in Fig. 37. The filter was designed at the fundamental frequency of 2 GHz and fabricated on a RT/Duroid 6010.2 substrate with a thickness  $h = 25$  mil and a relative dielectric constant  $\epsilon_r = 10.2$ . Table VIII shows the measured and the calculated results for the transmission zeros corresponding to the different tapping positions. Inspecting the results, the measurements agree well with the calculations.

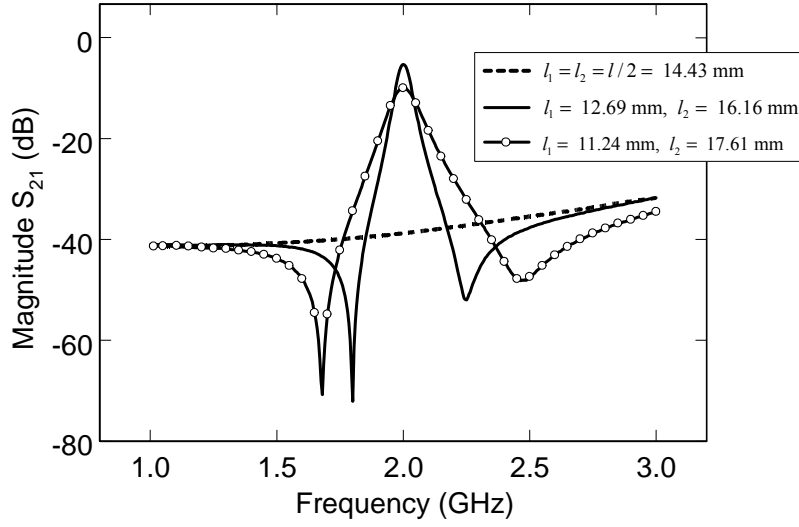


Fig. 38. Measured results for different tapping positions with coupling gap  $s_1 = 0.35$  mm .

Table VIII Measured and calculated results of the hairpin resonators for different tapping positions

	Measurements	Calculations
$l_1=l_2=l/2=14.43$ mm	No passband at 2 GHz	$f_1 = f_2 = 2$ GHz
$l_1= 12.69$ mm, $l_2= 16.16$ mm	$f_1= 1.8$ GHz, $f_2= 2.25$ GHz	$f_1= 1.79$ GHz, $f_2= 2.27$ GHz
$l_1= 11.24$ mm, $l_2= 17.61$ mm	$f_1= 1.68$ GHz, $f_2= 2.48$ GHz	$f_1= 1.64$ GHz, $f_2= 2.57$ GHz

Fig. 39 shows the configuration of the filter using two hairpin resonators with symmetric feed lines tapping the resonators. The  $ABCD$  matrixes for the upper and lower sections of the lossless shun circuit are given by

$$\begin{bmatrix} A & B \\ C & D \end{bmatrix}_{upper} = M_1 M_2 M_1 \quad (67)$$

$$\begin{bmatrix} A & B \\ C & D \end{bmatrix}_{lower} = M_3 M_2 M_3. \quad (68)$$

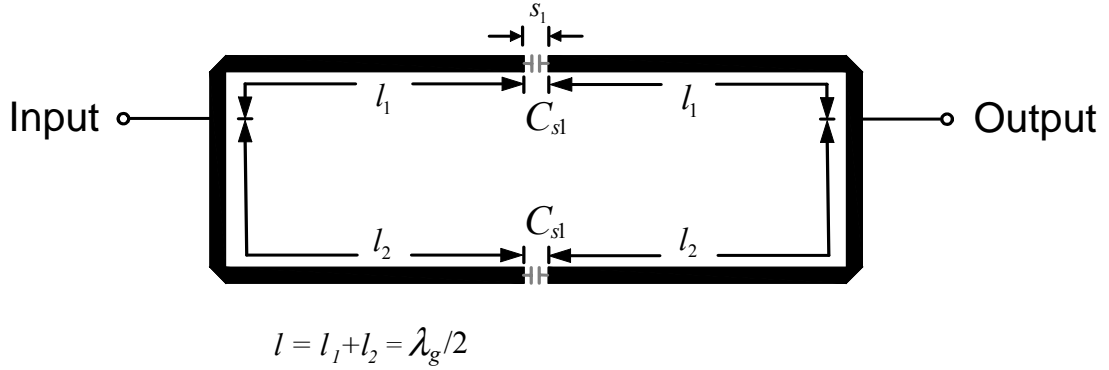


Fig. 39. Configuration of the filter using two hairpin resonators with symmetric tapping feed lines.

Also, by using the same operations as above, the  $S_{21}$  of the circuit can be obtained as

$$S_{21} = \frac{2MNY_L}{(P + MY_L)^2 - N^2} \quad (68)$$

where

$$M = z_c^2 \cos^2 \beta l_1 \cos^2 \beta l_2 - z_o^2 \sin 2\beta l_1 \sin 2\beta l_2 + j2z_o z_c \sin \beta l \cos \beta l_1 \cos \beta l_2,$$

$$N = z_c (\cos^2 \beta l_1 + \cos^2 \beta l_2) + j2z_o (\sin \beta l_1 \cos \beta l_1 + \sin \beta l_2 \cos \beta l_2), \text{ and}$$

$$P = z_c (\cos^2 \beta l_1 + \cos^2 \beta l_2 - 2\sin^2 \beta l) + j \sin \beta l (2z_o \cos \beta l + z_c^2 y_o \cos \beta l_1 \cos \beta l_2).$$

Observing (68), it is not easy to inspect the value of  $S_{21}$  to find any transmission zero. To investigate the results in (68), a filter tapped by the symmetric feed lines with lengths of  $l_1 = 12.56$  mm and  $l_2 = 16.56$  mm is used. As shown in Fig. 40, the calculated results agree well with the measured results. Also, in Fig. 40, there is no transmission zero, which implies  $S_{21} \neq 0$  in (68). Comparing with the asymmetric tapping feed line structure in Fig. 37, the filter that uses the symmetric tapping feed lines shows a Chebyshev frequency response.

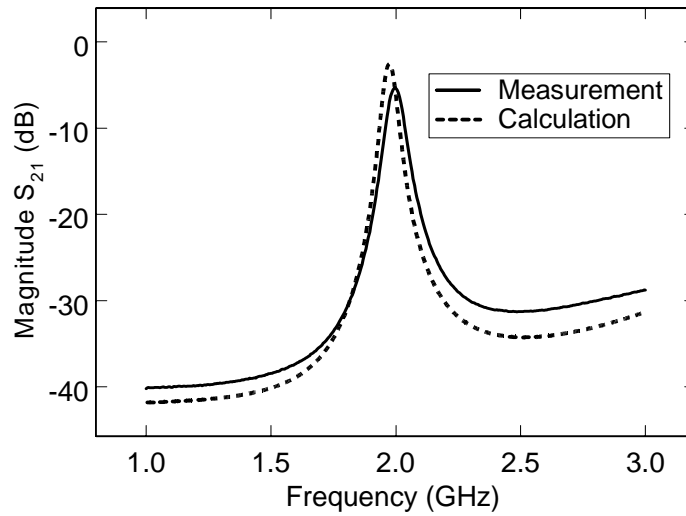


Fig. 40. Measured and calculated results for the filter using symmetric tapping feed lines with coupling gap  $s_1 = 0.35$  mm.

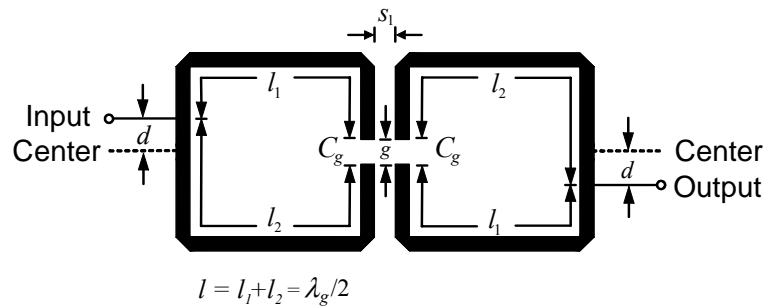


Fig. 41. Layout of the filter using two open-loop ring resonators with asymmetric tapping feed lines.

### C. Compact Size Filters

#### 1) Filters Using Two Open-Loop Ring Resonators

Fig. 41 shows the filter using two open-loop ring resonators [55]. This type resonator with two folded arms is more compact than the filter in Fig. 37. This filter has the same dimensions as the filter in Fig. 37, except for the two additional 45 degree chamfered bends and the coupling gap  $g = 0.5$  mm between the two open ends of the

ring. Fig. 42 shows the measured results for the different tapping positions on the rings. The measured locations of the transmission zeros are listed in Table IX. Comparing with Table VIII, the locations of the transmission zeros of the filters using open-loop rings are very close to those of the filters using hairpin resonators. This implies that the coupling effects between the two rings and the effects of two additional 45 degree chamfered bends only slightly affect the locations of the two transmission zeros. Thus, (66) can also be used to predict the locations of the transmission zeros of the filters using open-loop rings.

Table IX Measured results of the open-loop ring resonators for different tapping positions

Measurements	
$l_1=l_2=l/2=14.43$ mm	No passband at 2 GHz
$l_1=12.69$ mm, $l_2=16.16$ mm	$f_1=1.83$ GHz, $f_2=2.24$ GHz
$l_1=11.24$ mm, $l_2=17.61$ mm	$f_1=1.69$ GHz, $f_2=2.5$ GHz

Observing the measured results in Figs. 38 and 42, the tapping positions also affect the couplings between two resonators. The case of  $l_1 = 12.69$  mm and  $l_2 = 16.16$  mm in Fig. 42 shows an overcoupled condition [49,70], which has a hump within the passband. The overcoupled condition is given by

$$K > \frac{1}{Q_u} + \frac{1}{Q_{ext}} \quad (69)$$

where  $K$  is the coupling coefficient,  $Q_u$  is the unloaded  $Q$  of either of the two resonators, and  $Q_{ext}$  is the external  $Q$ . The coupling condition of the filter can be found using the measured  $K$ ,  $Q_u$ , and  $Q_{ext}$  [5,55,71]. The measured  $K$  is



$$K = \frac{f_{p2}^2 - f_{p1}^2}{f_{p2}^2 + f_{p1}^2} \quad (70)$$

where  $f_{p2}$  and  $f_{p1}$  are the high and low resonant frequencies.

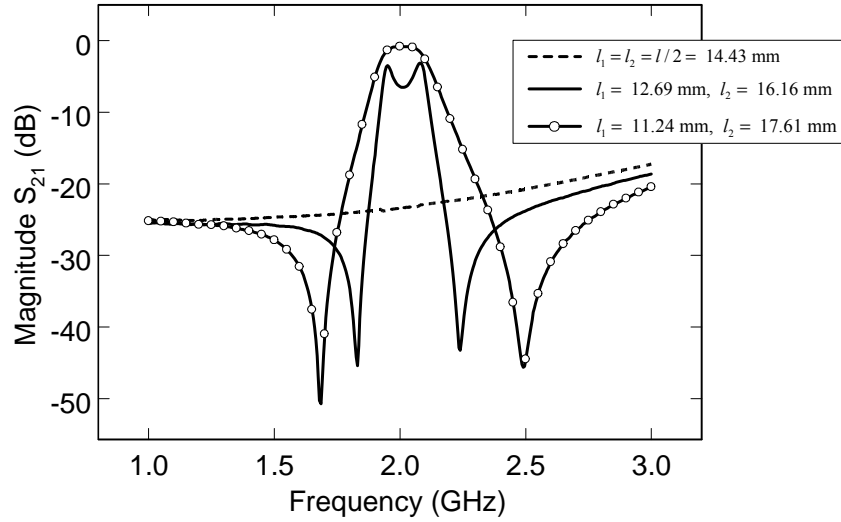


Fig. 42. Measured results for different tapping positions with coupling gap  $s_1 = 0.35$  mm.

The measured external  $Q$  is given by

$$Q_{ext} = \frac{f_o}{\Delta f_{\pm 90^\circ}} \quad (71)$$

where  $\Delta f_{\pm 90^\circ}$  is the bandwidth about the resonant frequency, over which the phase varies from  $-90^\circ$  to  $+90^\circ$ . Also, the expression for the measured unloaded  $Q$  can be found in [5].

Fig. 41 shows the tapping positions at a distance  $d$  from the center of the resonators to the input and output ports. When  $d$  becomes shorter or the tapping position moves toward to the center, the external  $Q$  becomes larger [57]. The larger external  $Q$  allows the filter to approach the overcoupled condition in (70), causing a hump within the passband. In addition, observing (66) and (69), for a shorter  $d$ , the two transmission zeros appear close to the passband, providing a high selectivity nearby the passband. But, this may easily induce an overcoupled condition. Beyond the coupling effects caused by the tapping positions, the coupling gap  $s_l$  also influences the couplings between two resonators [55]. Therefore, to avoid overcoupling, the proper tapping positions and gap size should be carefully chosen.

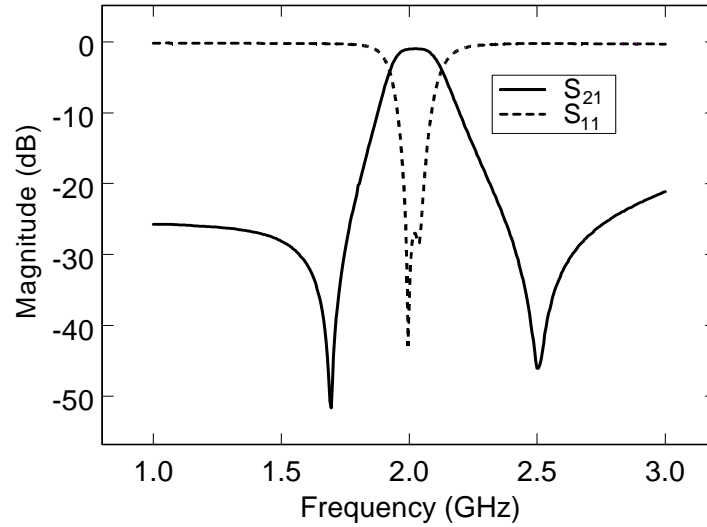


Fig. 43. Measured results of the open-loop ring resonators for the case of tapping positions of  $l_1 = 11.24$  mm and  $l_2 = 17.61$  mm.

Fig. 43 shows the measured results of the filter for the case of  $l_1 = 11.24$  mm and  $l_2 = 17.61$  mm. This filter with  $K = 0.02 < 1/Q_u + 1/Q_{ext} = 1/130 + 1/15.4$  shows an undercoupled condition [36,57], which does not have a hump in the passband. The filter has an insertion loss of 0.95 dB at 2.02 GHz, a return loss of greater than 20 dB from

1.98 to 2.06 GHz, and two transmission zeros at 1.69 GHz with  $-50.7$  dB rejection and 2.5 GHz with  $-45.5$  dB rejection, respectively. The 3-dB fractional bandwidth of the filter is 10.4 %. Comparing with the insertion losses of the cross coupling filters at similar fundamental resonant frequencies (2.8 dB in [67] and 2.2 dB in [55]), the filter in Fig. 43 has a lower insertion loss of 0.95 dB.

## 2) Filters Using Four Cascaded Open-Loop Ring Resonators

The filter using cascaded resonators is shown in Fig. 44. The filter uses the same dimensions as the open-loop ring in Fig. 41 with the tapping positions of  $l_1 = 11.24$  mm and  $l_2 = 17.61$  mm at the first and last resonators. Also, the offset distance  $d_1$  between the rings 2 and 3 is designed for asymmetric feeding between rings 1, 2 and rings 3,4 to maintain the sharp cut-off frequency response. Therefore, the positions of the two transmission zeros of the filter can be predicted around 1.69 and 2.5 GHz, respectively. The coupling gap size between rings is  $s_2$ .

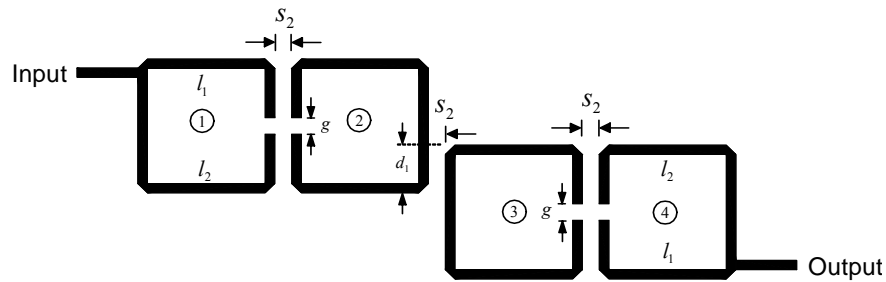


Fig. 44. Configuration of the filter using four cascaded open-loop ring resonators.

The coupling gap  $s_2 = 0.5$  mm and the offset distance  $d_1 = 2.88$  mm are optimized by EM simulation [35] to avoid the overcoupled condition.

The measured external  $Q$  and the mutual coupling  $M$  can be calculated from (70) and (71), and they are

$$Q_{ext} = 15.4 \text{ and } M = \begin{bmatrix} 0 & -0.037 & 0 & 0 \\ -0.037 & 0 & 0.035 & 0 \\ 0 & 0.035 & 0 & -0.037 \\ 0 & 0 & -0.037 & 0 \end{bmatrix}, \text{ where the negative sign in}$$

coupling matrix is for electrical coupling [55]. Fig. 45 shows the simulated and measured results. The filter has a fractional 3-dB bandwidth of 6.25%. The insertion loss is 2.75 dB at 2 GHz, and the return loss is greater than 13.5 dB within 1.95-2.05 GHz. The out-of-band rejection is better than 50 dB extended to 1 and 3 GHz and beyond.

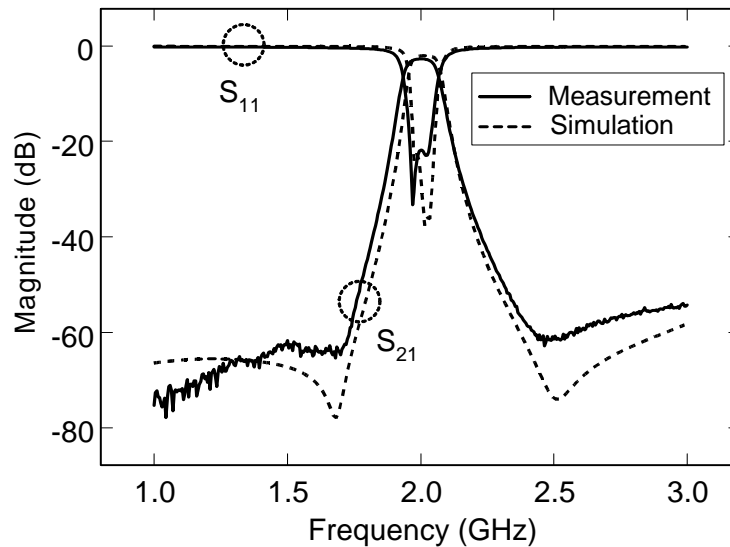


Fig. 45. Measured and simulated results of the filter using four cascaded open-loop ring resonators.

### 3) *Filters Tuning by a Piezoelectric Transducer*

Electronically tunable filters have many applications in transmitters and receivers. As shown in Fig. 46, the tunable filter circuit consists of the filter using cascaded resonators, a piezoelectric transducer (PET), and an attached dielectric perturber [72]

above the filter. The PET is a composition of lead, zirconate, and titanate [73]. The PET shown in Fig. 46 consists of two piezoelectric layers and one shim layer.

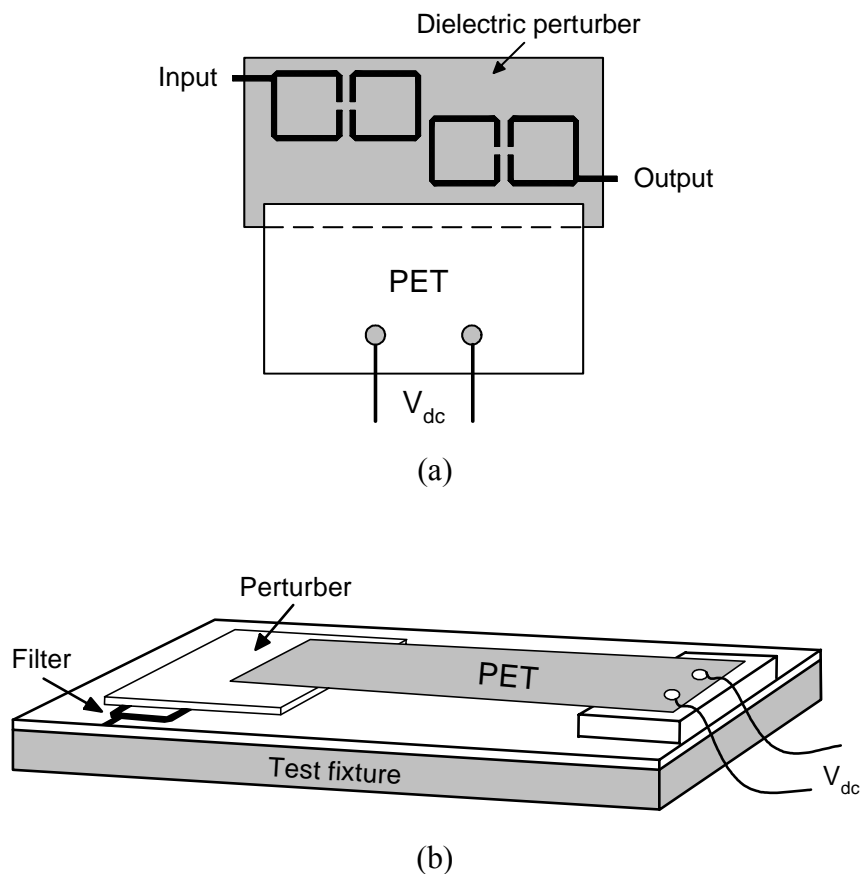


Fig. 46. Configuration of the tunable bandpass filter (a) top view and (b) 3D view.

The center shim laminated between the two same polarization piezoelectric layers adds mechanical strength and stiffness. Also, the shim is connected to one polarity of a DC voltage to deflect the PET and move it up or down vertically. The PET can be deflected over  $\pm 1.325$  mm at  $\pm 90$  V.

Inspecting the structure in Fig. 46, when the perturber moves up or down, the effective dielectric constant of the filter is decreasing or increasing [74], respectively, allowing the

passband of the filter to shift toward the higher or lower frequencies. Fig. 47 shows the measured results for the tuning range of the passband. With the maximum applied voltage of 90 V and a perturber of dielectric constant  $\epsilon_r = 10.8$  and thickness  $h = 50$  mil, the tuning range of the filter is 6.5 %. The small tuning range can be increased by using a higher dielectric constant perturber. The 3-dB bandwidths of the filters with and without PET tuning are 130 MHz and 125 MHz, respectively. This shows that the PET tuning has little effect on bandwidth. The size of the PET is 70 mm x 32 mm x 0.635 mm. The overall size of the filter including the perturber and PET is 90 mm x 50 mm x 3.85 mm.

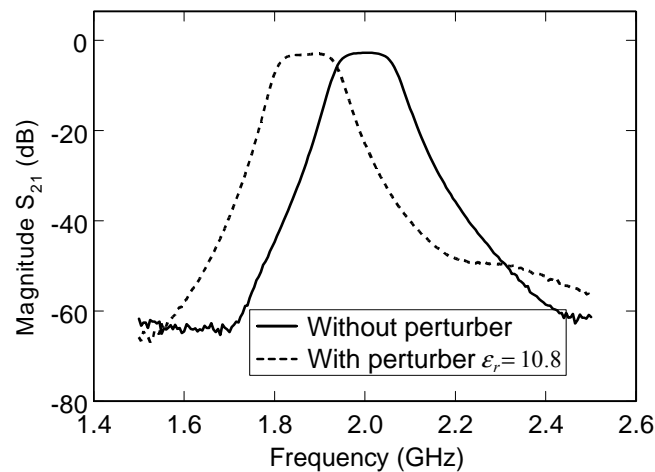


Fig. 47. Measured results of the tunable bandpass filter with a perturber of  $\epsilon_r = 10.8$  and  $h = 50$  mil.

#### D. Conclusions

A simple transmission-line model is used to calculate the locations of two transmission zeros to design high-selectivity microstrip bandpass filters. In addition, the coupling effects due to the tapping positions of the asymmetric feed lines are discussed. The filter using two open-loop ring resonators with two transmission zeros show lower insertion loss than a cross-coupled filter. Also, the filter using four cascaded resonators

shows a better rejection than a cross-coupled filter using four resonators. Moreover, a PET is used to vary the effective dielectric constant of the filter to tune the passband of the filter. These compact size and high selectivity bandpass filters should be useful for wireless and satellite communication systems.

## CHAPTER VII

COMPACT, LOW INSERTION LOSS, SHARP REJECTION AND WIDEBAND  
MICROSTRIP BANDPASS FILTERS\**A. Introduction*

High performance, compact size, and low cost are highly desirable for modern microwave filters in the next generation of many wireless systems. The microstrip ring resonator satisfies these demands and is finding wide use in many bandpass filters [5]. However, the conventional end-to-line coupling structure of the ring resonator suffers from high insertion loss [18]. Also, the coupling gaps between the feed lines and the resonator affect the resonant frequencies of the resonator. To reduce the high insertion loss, filters used an enhanced coupling structure or lumped capacitors were proposed [14,21,51,70,75]. However, the filters using this enhanced coupling structure still have coupling gaps. In addition, the filters using lumped capacitors are not easy to fabricate. Ring resonators using high temperature superconductor (HTS) to obtain a very low insertion loss have been reported [76]. This approach has the advantage of very low conductor loss but requires a complex fabrication process.

In this chapter, a new compact, low insertion loss, sharp rejection, wideband microstrip bandpass filter is proposed. The wide bandpass filter is developed from a new bandstop filter introduced in section *B*. Two tuning stubs are added to the bandstop filter to create a wide passband. Without coupling gaps between feed lines and rings, there are no mismatch and radiation losses between them. Thus, the new filter can obtain a low insertion loss [77], and the major losses of the filter are contributed by

---

\*Reprinted with permission from (complete publication information) "Compact, low insertion loss, sharp rejection and wideband microstrip bandpass filters" by Lung-Hwa Hsieh and Kai Chang, 2003. *IEEE Trans. Microwave Theory Tech.*, vol. 51, pp. 1241-1246. © 2004 by the IEEE.



conductor and dielectric losses. A simple transmission line model is used to calculate the frequency responses of the filters. The measurements show good agreement with the calculations.

*B. Bandstop and Bandpass Filters Using a Single Ring with One or Two Tuning Stubs*

*1) Bandstop Characteristic*

The bandstop characteristic of the ring circuit can be realized by using two orthogonal feed lines with coupling gaps between the feed lines and the ring resonator [5]. For odd-mode excitation, the output feed line is coupled to a position of the zero electric field along the ring resonator and shows a short circuit [78]. Therefore, no energy is extracted from the ring resonator, and the ring circuit provides a stopband. A ring resonator directly connected to a pair of orthogonal feed lines is shown in Fig. 48. No coupling gaps are used between the resonator and the feed lines. The circumference  $l_r$  of the ring resonator is expressed as [5]

$$l_r = n\lambda_g \quad (72)$$

where  $n$  is the mode number and  $\lambda_g$  is the guided wavelength.

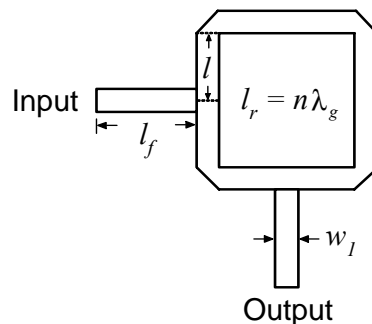


Fig. 48. A ring resonator using direct-connected orthogonal feeders.

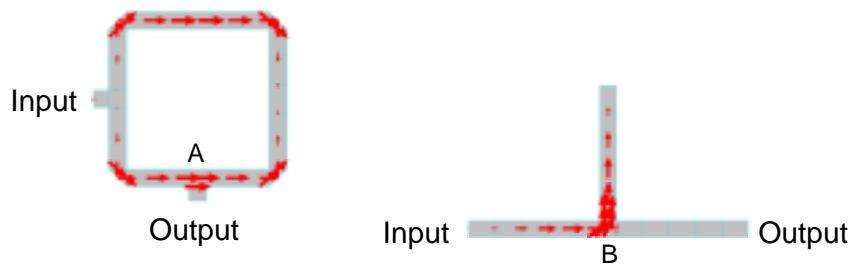


Fig. 49. Simulated electric current at the resonant frequency for the ring and open stub bandstop circuits.

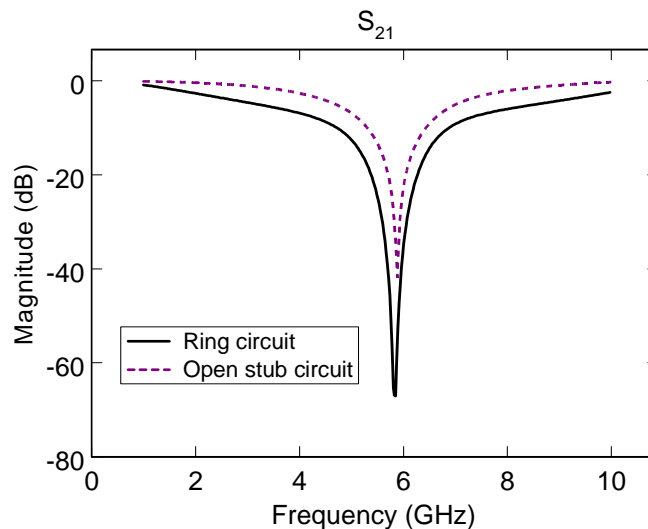


Fig. 50. Simulated results for the bandstop filters.

In order to investigate the behavior of this ring circuit, an EM simulator [35] and a transmission line model are used. Fig. 49 shows the EM simulated electric current distribution of the ring circuit and a conventional  $\lambda_g/4$  open-stub bandstop filter at the same fundamental resonant frequency. The arrows represent the electric current. The simulated electric current shows minimum electric fields at positions A and B, which correspond to the maximum magnetic fields. Thus, both circuits provide bandstop characteristics by presenting zero voltages to the outputs at the resonant frequency that

can be observed by their simulated frequency response of  $S_{21}$  as shown in Fig. 50. The ring resonator and the conventional  $\lambda_g/4$  open-stub bandstop filter are designed at fundamental resonant frequency of  $f_o = 5.6$  GHz and fabricated on a RT/Duriod 6010.2 substrate with a thickness  $h = 25$  mil and a relative dielectric constant  $\epsilon_r = 10.2$ . The dimensions of the ring are  $l_f = 5$  mm,  $l_r = 20.34$  mm,  $w_l = 0.6$  mm.

The equivalent ring circuit shown in Fig. 51 is divided by the input and output ports to form a shunt circuit denoted by the upper and lower parts, respectively. The equivalent circuits of the 45-degree-mitered bend are represented by the inductor  $L$  and capacitor  $C$  [79] those are expressed by

$$C = 0.001h[(3.39\epsilon_r + 0.62)(\frac{w_l}{h})^2 + 7.6\epsilon_r + 3.8](\frac{w_l}{h}) \text{ pF} \quad (73a)$$

$$L = 0.22h\{1 - 1.35 \exp[-0.18(\frac{w_l}{h})^{1.39}]\} \text{ nH} \quad (73b)$$

where  $h$  and  $w_l$  are in mm. The capacitance  $jB_T$  is the T-junction effect between the feed line and the ring resonator [80]. The frequency response of the ring circuit can be calculated from the equivalent ring circuit using  $ABCD$ ,  $Y$ , and  $S$  parameters. Fig. 52 shows the calculated and measured results with good agreement.

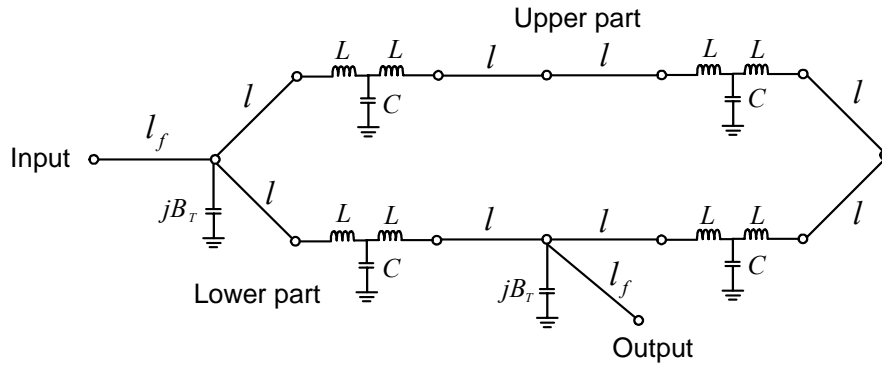


Fig. 51. Equivalent circuit of the ring using direct-connected orthogonal feed lines.

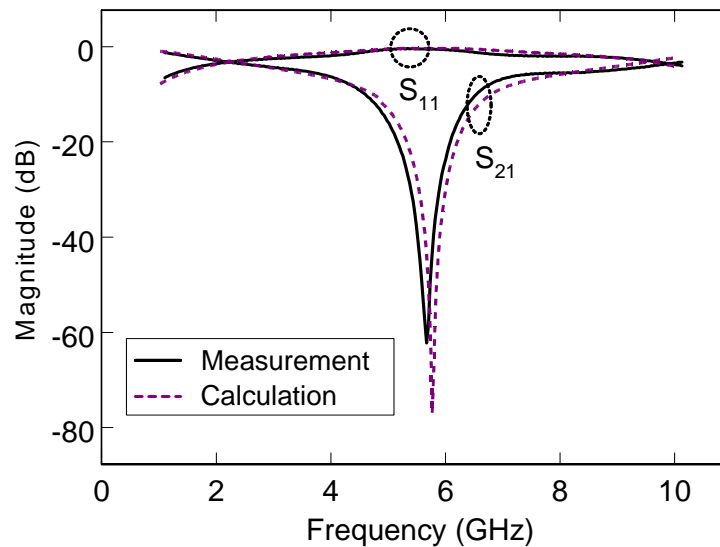


Fig. 52. Calculated and measured results of the ring using direct-connected orthogonal feed lines.

## 2) One Tuning Stub

The effect of adding a tuning stub on the gap-coupled ring resonator has been discussed [5]. By changing the size or length of the tuning stub, the frequency response of the ring resonator is varied. Fig. 53 illustrates the orthogonal-feed ring resonator with a tuning stub of  $l_t = \lambda_g / 4$  designed at the fundamental resonant frequency and placed at the center of either side of the ring resonator. Furthermore, the ring resonator with one tuning stub forms an asymmetric configuration and will excite degenerate modes. The higher impedance of the tuning stub ( $w_2$  for 50 ohms  $<$   $w_1$  for 64 ohms) is designed for a better return loss of the filter using two tuning stubs that will be shown in the part 3 of this section.

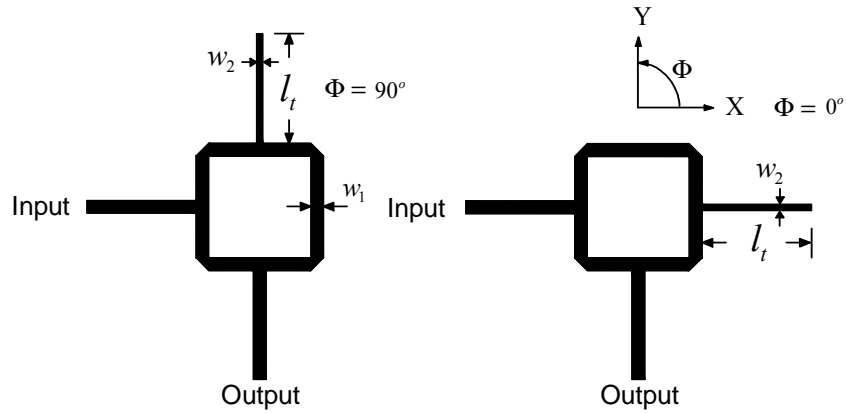


Fig. 53. Configuration of the ring with a tuning stub of  $l_t = 5.03$  mm and  $w_2 = 0.3$  mm at  $\Phi = 90^\circ$  or  $0^\circ$ .

Fig. 54 shows the equivalent circuit of the ring circuit with the tuning stub at  $\Phi = 90^\circ$ .  $Y_t$  is the admittance looking into the tuning stub and can be expressed by

$$Y_t = y_o \tanh[\gamma(l_t + l_{open})] + jB_{T1} \quad (74)$$

where  $y_o$  is the characteristic admittance of the tuning stub,  $\gamma$  is the complex propagation constant,  $l_{open}$  is the equivalent open-effect length [69], and  $jB_{T1}$  is the capacitance of the T-junction between the ring and the tuning stub  $l_t$ . The frequency response of the ring circuit can be obtained from the equivalent circuit by using  $ABCD$ ,  $Y$ , and  $S$  parameter calculations. Fig. 55 shows the calculated results for the different lengths of the tuning stub located at  $\Phi = 90^\circ$ . Inspecting the results, when the length of the tuning stub increases, the degenerate modes of the ring at the fundamental and the third modes are excited and moved to the lower frequencies. In addition, at the length of  $l_t = \lambda_g/4 = 5.03$  mm, the ring circuit has three attenuation poles as shown in Fig. 56.

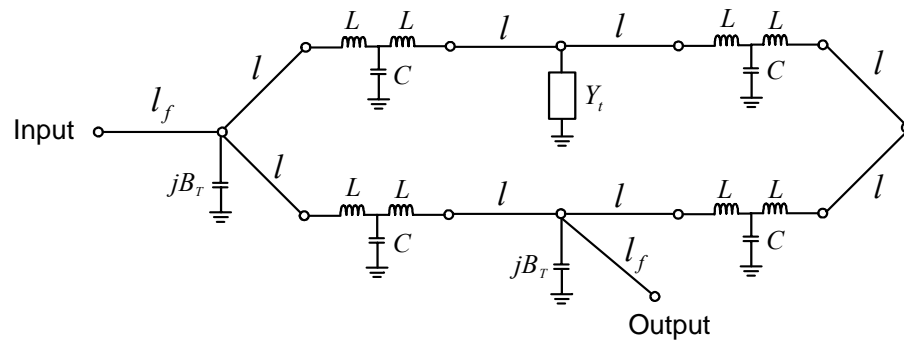


Fig. 54. Equivalent circuit of the ring using a tuning stub at  $\Phi = 90^\circ$ .

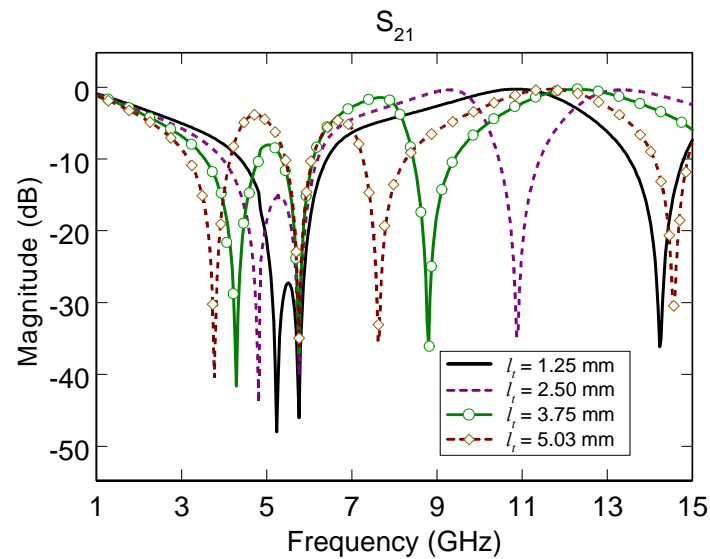


Fig. 55. Calculated results of the ring with various lengths of the tuning stub at  $\Phi = 90^\circ$ .

Comparing the frequency response to that of the ring circuit without the tuning stub in Fig. 52, the two additional degenerate modes are induced by the  $\lambda_g/4$  tuning stub. The three attenuation poles are  $f_1 = 3.81$  GHz with -39 dB rejection,  $f_o = 5.77$  GHz with -36 dB rejection, and  $f_2 = 7.75$  GHz with -37 dB rejection. Furthermore, inspecting the ring resonators with the tuning stub at  $\Phi = 90^\circ$  or  $\Phi = 0^\circ$  in Fig. 53,  $S_{21}$  is the same for both cases due to the symmetry between these reciprocal networks.

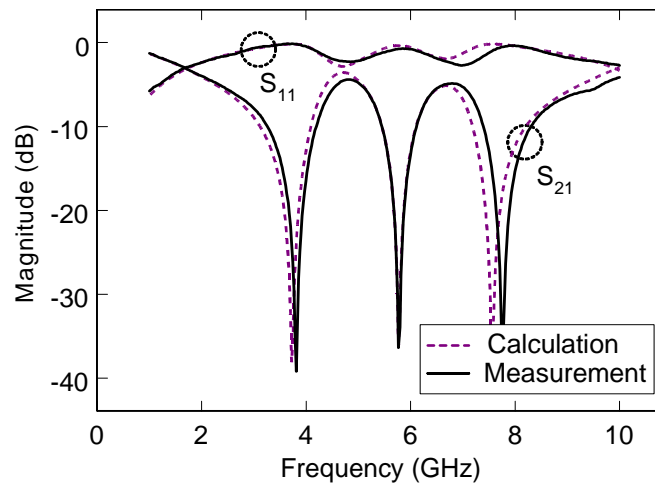


Fig. 56. Calculated and measured results of the ring using a tuning stub at  $\Phi = 90^\circ$ .

### 3) Two Tuning Stubs

Fig. 57 shows the layout and equivalent circuit of a ring resonator with two tuning stubs of length  $l_t = \lambda_g/4$  at  $\Phi = 90^\circ$  and  $\Phi = 0^\circ$ . This symmetric ring circuit is divided by the tuning stubs and the input/output ports into four equal sections. The ring circuit can be treated as a combination of both perturbed ring circuits given in Fig. 53.

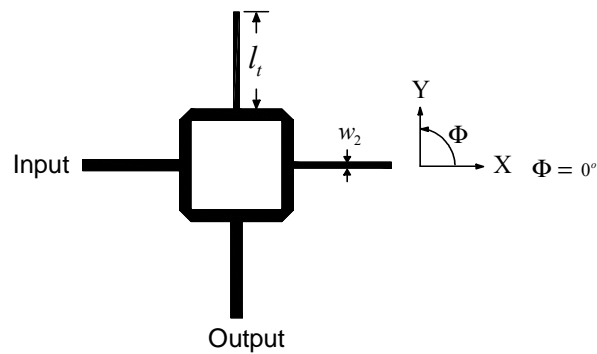


Fig. 57. Layout of the ring using two tuning stubs at  $\Phi = 90^\circ$  and  $0^\circ$ .

Also, by changing the lengths of two tuning stubs, the frequency response of the ring circuit will be varied. Observing the calculated results in Fig.58, two attenuation poles starting from the center frequencies of the fundamental and the third modes move to the lower frequencies and form a wide passband. The measured and calculated results of the filter with the tuning stubs of length  $\lambda_g/4$  are shown in Fig. 59. In addition, due to the symmetric structure, the ring circuit in Fig. 57 only excites a single mode.

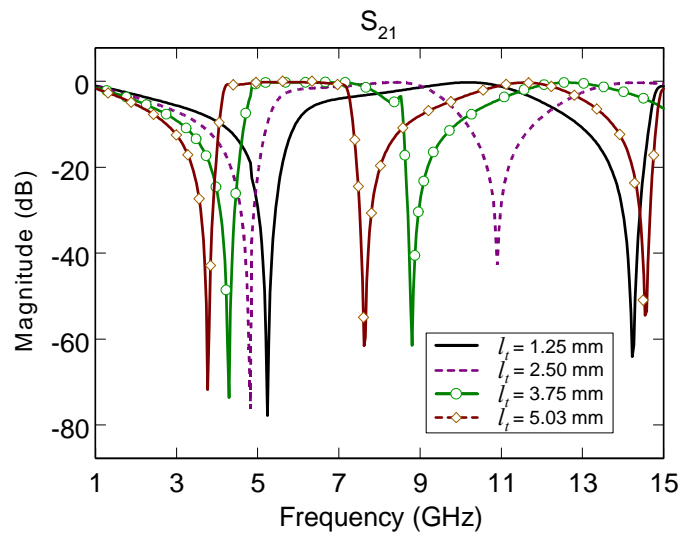


Fig. 58. Calculated results of the ring with various lengths of the tuning stub at  $\Phi = 90^\circ$  and  $0^\circ$ .

Comparing the results in Fig. 59 with those in Fig. 56, the effects of adding two tuning stubs with a length of  $l_t = \lambda_g/4$  at  $\Phi = 90^\circ$  and  $\Phi = 0^\circ$  provide a sharper cut-off frequency response, increase attenuations, and obtain a wide pass band. Two attenuation poles are  $f_1 = 3.81$  GHz with -46 dB rejection and  $f_2 = 7.75$  GHz with -51 dB rejection. The differences between the measurement and the calculation on  $f_1$  and  $f_2$  are due to fabrication tolerances that cause a slightly asymmetric layout and excite small degenerate modes.



The key point behind this new filter topology is that two tuning stubs loaded on the ring resonator at  $\Phi = 90^\circ$  and  $\Phi = 0^\circ$  are used to achieve a wide passband with a sharp cut-off characteristic. This approach can, in fact, be interpreted as using two stopbands induced by two tuning stubs in conjunction with the wide passband. In some cases, an undesired passband below the main passband may require a high passband section to be used in conjunction with this approach.

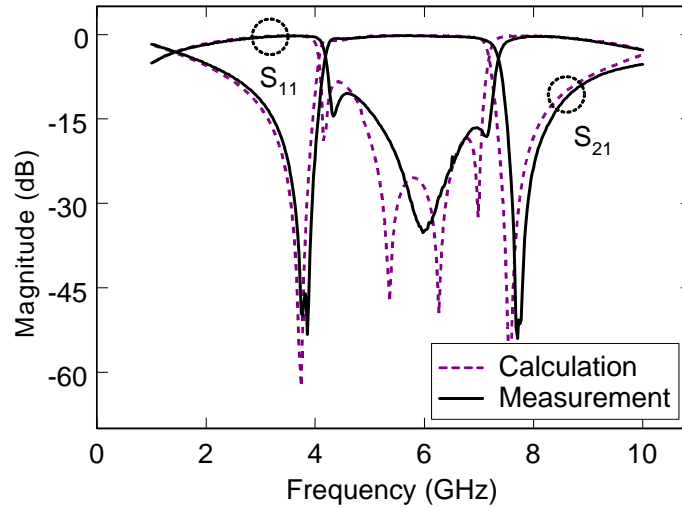


Fig. 59. Calculated and measured results of the ring with two tuning stubs of  $l_t = \lambda_g/4 = 5.026$  mm at  $\Phi = 90^\circ$  and  $0^\circ$ .

### C. Wideband Microstrip Bandpass Filters with Dual Mode Effects

Observing the frequency response in Fig. 59, the two stopbands of the filter show a narrow bandwidth. To increase the narrow stopbands, a dual-mode design can be used [5]. A square perturbation stub at  $\Phi = 45^\circ$  on the ring resonator is incorporated in Fig. 60(a). The square stub perturbs the fields of the ring resonator so that the resonator can excite a dual mode around the stopbands in order to improve the narrow stopbands. By increasing (decreasing) the size of the square stub, the distance (stopband bandwidth)

between two modes is increased (decreased). The equivalent circuits of the square stub and the filter are displayed in Figs. 60(b) and (c), respectively.

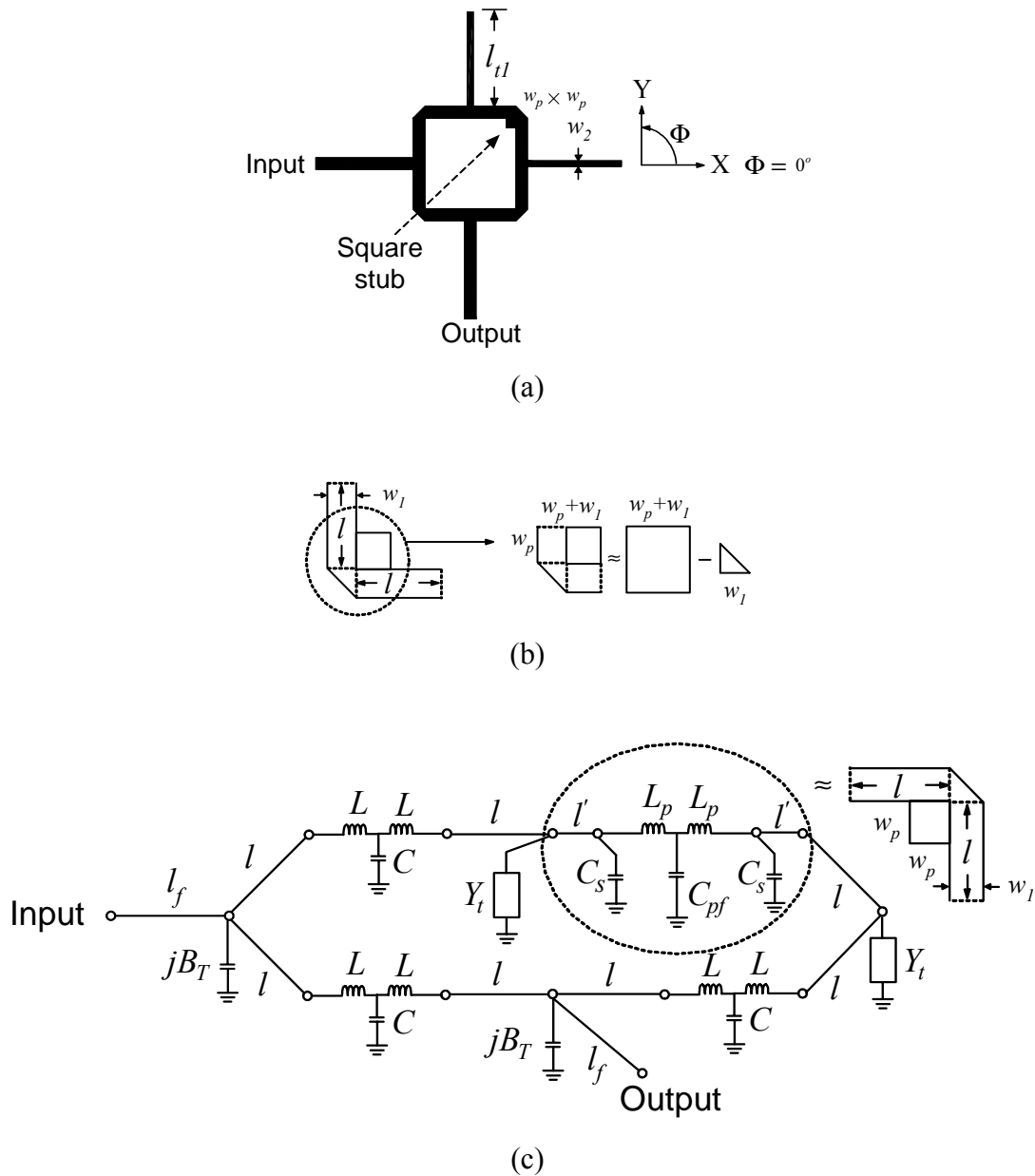


Fig. 60. The dual-mode filter (a) layout, (b) equivalence of the perturbed stub and (c) overall equivalent circuit.

As seen in Fig. 60(b), the geometry at the corner of  $\Phi = 45^\circ$  is approximately equal to the square section of width  $w_l + w_p$ , subtracting an isometric triangle of height  $w_l$ . Also, the equivalent L-C circuit of this approximation is shown in Fig. 60(c) where  $C_{pf} = C_r - C$  and  $L_p = LL_r/(L-L_r)$ . The equivalent capacitance and inductance of the right angle bend,  $C_r$  and  $L_r$ , are given by [79]

$$C_r = 0.001h[(10.35\epsilon_r + 2.5)\left(\frac{w_l + w_p}{h}\right)^2 + 2.6\epsilon_r + 5.64]\left(\frac{w_l + w_p}{h}\right) \text{ pF} \quad (75a)$$

$$L_r = 0.22h\{1 - 1.35 \exp[-0.18\left(\frac{w_l + w_p}{h}\right)^{1.39}]\} \text{ nH}. \quad (75b)$$

The asymmetric step capacitance  $C_s$  is [81]

$$C_s = w_p(0.012 + 0.0039\epsilon_r) \text{ pF}. \quad (76)$$

In the above equations, all lengths are in mm. The length of the tuning stubs and the size of the square stub are  $l_{t1} = 4.83$  mm and  $w_p \times w_p = 0.5 \times 0.5$  mm<sup>2</sup>.

The calculated and measured results of the filter are shown in Fig. 61. As seen in Fig. 61, the square stub generates two transmission zeros (which are marked as x in Fig. 61) or dual modes located on either side of the passband at 3.66, 7.62 and 7.62, 8.07 GHz, respectively. Comparing  $S_{21}$  with that in Fig. 59, the dual mode effects or transmission zeros increase the stopband bandwidth and also improve the return loss in the edges of the passband. The filter has 3-dB fractional bandwidth of 51.6 %, a insertion loss of better than 0.7 dB, two rejections of greater than 18 dB within 3.43 – 4.3 GHz and 7.57 to 8.47 GHz, and an attenuation rate for the sharp cut-off frequency responses of 137.58 dB/GHz (calculated from 4.173 GHz with –36.9 dB to 4.42 GHz with –2.85 dB) and 131.8 dB/ GHz (calculated from 7.44 GHz with 3.77 dB to 7.62 GHz with -27.5 dB). In addition, comparing the new filter with some compact and low insertion loss filters [82,83], those filters only show gradual rejections. To obtain a

sharp cut-off frequency response, the filters need to increase numbers of resonators. However, increasing numbers of resonators increases the insertion loss and the size of the filter and also narrows the passband bandwidth [84,85].

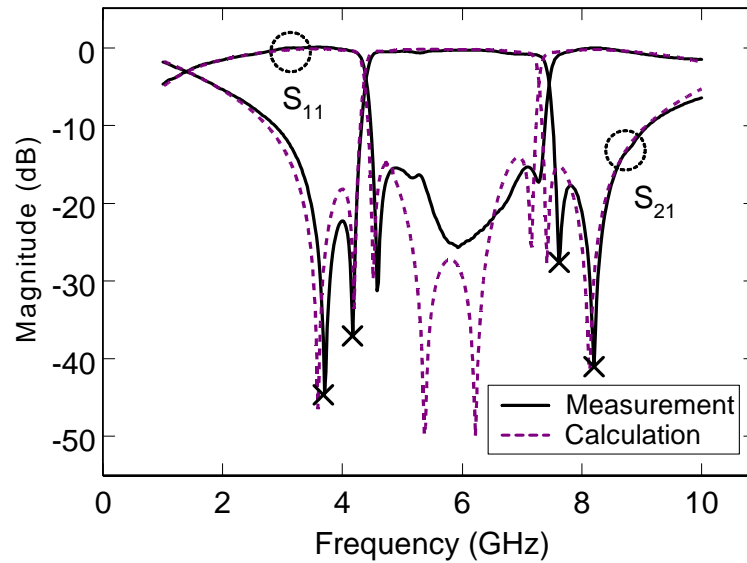


Fig. 61. Calculated and measured results of the dual-mode ring filter. The crosses (x) show the two transmission zero locations.

To obtain even higher rejection, a filter using three cascaded ring resonators is shown in Fig. 62. In this configuration, the three ring resonators are connected by a short transmission line of length  $l_c = \lambda_g / 4 = 4.89$  mm. The different length  $l_{t2} = 4.85$  mm,  $l_{t3} = 4.88$  mm,  $l_{t4} = 4.83$  mm for the tuning stubs are optimized for a good return loss.

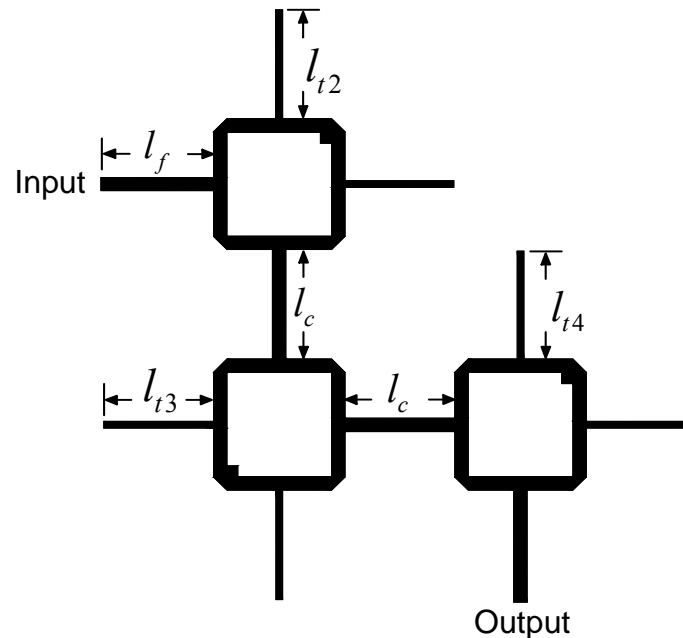


Fig. 62. Configuration of the cascaded dual-mode ring resonator.

Fig. 63 shows the calculated and measured results. The calculation also uses the transmission-line model with  $ABCD$ ,  $Y$ , and  $S$  parameter operations. The 3-dB fractional bandwidth of the filter is 49.3 %. The filter has an insertion loss better than 1.6 dB and return loss greater than 13.3 dB in the passband from 4.58 to 7.3 GHz. Two stopbands are located at 2.75-4.02 GHz and 7.73-9.08 GHz with rejection greater than 40 dB. The attenuation rate of the filter for the sharp cut-off frequency responses is 99.75 dB/GHz (calculated from 4.17 GHz with  $-34.9$  dB to 4.49 GHz with  $-2.98$  dB) and 101.56 dB/GHz (calculated from 7.32 GHz with  $-3.4$  dB to 7.64 GHz with  $-35.9$  dB).

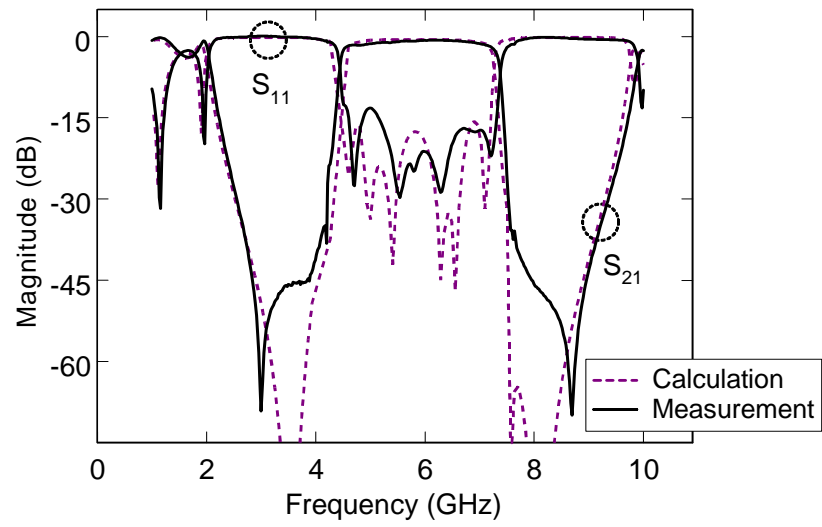


Fig. 63. Calculated and measured results of the cascaded dual-mode ring resonator filter.

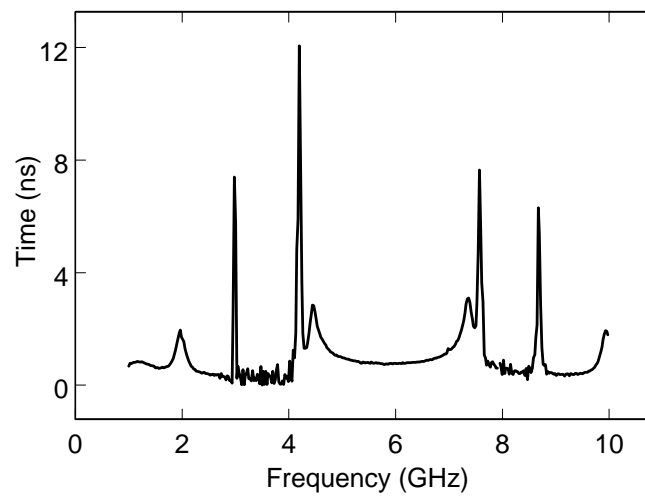


Fig. 64. Group delay of the cascaded dual-mode ring resonator filter.

The group delay of this wideband bandpass filter can be calculated by

$$\tau = -\frac{\partial \angle S_{21}}{\partial \omega} \quad (77)$$

where  $\angle S_{21}$  is the insertion loss phase and  $\omega$  is the frequency in radians per second. Fig. 64 shows the group delay of the filter. Within the passband, the group delay is below 2 nS.

#### *D. Conclusions*

A new compact, low insertion loss, sharp rejection, and wideband microstrip bandpass filter has been developed. A bandstop filter using a ring resonator with direct-connected orthogonal feeders is introduced. Next, new filters are developed from the bandstop filter to achieve a wideband passband and two sharp stopbands. Also, a dual-mode design was used to increase the widths of rejection bands. Without any coupling gaps between feed lines and rings, there are no mismatch and radiation losses between them. Therefore, the new filters show low insertion loss. Simple transmission line models are used to calculate the frequency responses of the new filters. The measurements agree well with the calculations. The new filters were designed for mitigating the interference in full duplex systems in satellite communications.

## CHAPTER VIII

## COMPACT ELLIPTIC-FUNCTION LOWPASS FILTERS\*

*A. Introduction*

Compact size and high performance microwave filters are highly demanded in many communication systems. Due to the advantages of small size and easy fabrication, the microstrip hairpin has been drawing much attention. From the conventional half-wavelength hairpin resonator to the latest stepped impedance hairpin resonator, a size reduction of the resonator has been dramatically achieved [52,57,67,86,87,88]. Conventionally, the behavior of the stepped impedance hairpin resonator has been described by using even- and odd-mode and network models [52,67]. However, they only showed limited expressions in terms of  $ABCD$  matrix, which do not provide a useful circuit design implementation such as equivalent lumped element circuits.

Small size lowpass filters are frequently required in many communication systems to suppress harmonics and spurious signals. The conventional stepped-impedance and Kuroda-identity-stubs lowpass filters only provide Butterworth and Chebyshev characteristics with a gradual cut-off frequency response [38]. In order to have a sharp cut-off frequency response, these filters require more sections. Unfortunately, increasing the number of sections also increases the size of the filter and insertion loss. Recently, the lowpass filter using photonic bandgap and defect ground structures [89,90] illustrated a similar performance as those of the conventional ones. A compact semi-lumped lowpass filter was also proposed [91]. However, using lumped elements increase the fabrication difficulties.

---

\*Reprinted with permission from (complete publication information) “Compact elliptic-function lowpass filters using microstrip stepped impedance hairpin resonators” by Lung-Hwa Hsieh and Kai Chang, 2003. *IEEE Trans. Microwave Theory Tech.*, vol. 51, pp. 193- 199. © 2004 by the IEEE.



The microstrip elliptic-function lowpass filters show the advantages of high performance, low cost and easy fabrication [92,93]. In [93], the elliptic-function lowpass filters using elementary rectangular structures provide a wide band passband with a sharp cut-off frequency response, but a narrow stopband.

In this chapter, an equivalent circuit model for the stepped impedance hairpin resonator is described. Also, a compact elliptic-function lowpass filter using the stepped impedance hairpin resonator is demonstrated. The dimensions of the prototype lowpass filters are synthesized from the equivalent circuit model with the published element-value tables. The exact dimensions of the filter are optimized by EM simulation. The filter using multiple cascaded stepped impedance hairpin resonators shows a very sharp cut-off frequency response with a low insertion loss. Furthermore, additional attenuation poles are added to suppress the second harmonic and achieve a broad stopband bandwidth. The measured results agree well with simulated results.

### B. Equivalent Circuit Model for the Step Impedance Hairpin

Fig. 65 shows the basic layout of the stepped impedance hairpin resonator. The stepped impedance hairpin resonator consists of the single transmission line  $l_s$  and coupled lines with a length of  $l_c$ .  $Z_s$  is the characteristic impedance of the single transmission line  $l_s$ .

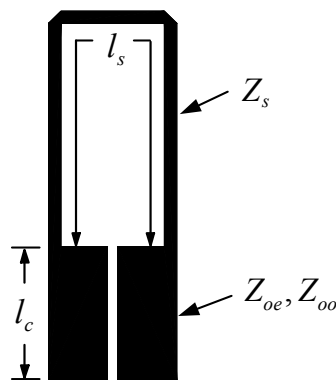


Fig. 65. A stepped impedance hairpin resonator.

$Z_{oe}$  and  $Z_{oo}$  are the even- and odd-mode impedance of the symmetric capacitance-load parallel coupled lines with a length of  $l_c$ . By selecting  $Z_s > \sqrt{Z_{oe}Z_{oo}}$ , the size of the stepped impedance hairpin resonator is smaller than that of the conventional hairpin resonator [94]. Also, the effect of the loading capacitance shifts the spurious resonant frequencies of the resonator from integer multiples of the fundamental resonant frequency, thereby reducing interferences from high-order harmonics.

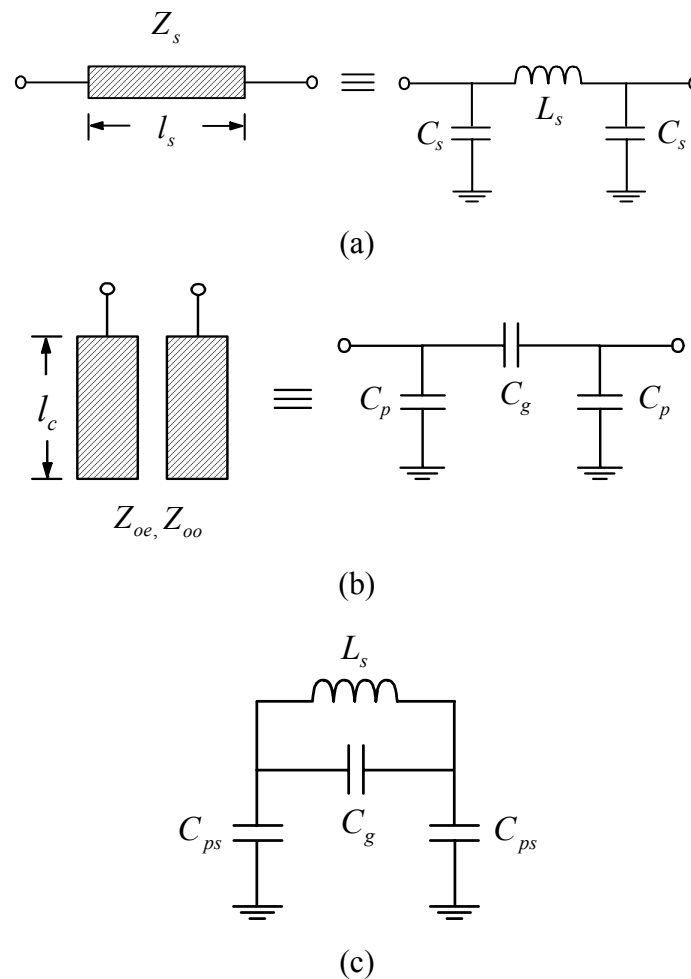


Fig. 66. Equivalent circuit of (a) single transmission line, (b) symmetric coupled lines, and (c) stepped impedance hairpin resonator.

The single transmission line is modeled as an equivalent  $L$ - $C$   $\pi$ -network as shown in Fig. 66(a). For the lossless single transmission line with a length of  $l_s$ , the  $ABCD$  matrix is given by

$$\begin{bmatrix} A & B \\ C & D \end{bmatrix} = \begin{bmatrix} \cos(\beta_s l_s) & jZ_s \sin(\beta_s l_s) \\ jY_s \sin(\beta_s l_s) & \cos(\beta_s l_s) \end{bmatrix} \quad (78)$$

$$\begin{bmatrix} A & B \\ C & D \end{bmatrix} = \begin{bmatrix} 1 + Z_L Y_c & Z_L \\ Y_c(2 + Z_L Y_c) & 1 + Z_L Y_c \end{bmatrix} \quad (79)$$

where  $Z_L = j\omega L_s$ ,  $Y_c = j\omega C_s$ ,  $\omega$  is the angular frequency,  $L_s$  and  $C_s$  are the equivalent inductance and capacitance of the single transmission line. Comparing (78) with (79), the equivalent  $L_s$  and  $C_s$  can be obtained as

$$L_s = \frac{Z_s \sin(\beta_s l_s)}{\omega} \text{ H} \quad (80a)$$

$$\text{and } C_s = \frac{1 - \cos(\beta_s l_s)}{\omega Z_s \sin(\beta_s l_s)} \text{ F.} \quad (80b)$$

Moreover, as seen in Fig. 66(b), the symmetric parallel coupled lines are modeled as an equivalent capacitive  $\pi$ -network. The  $ABCD$  matrix of the lossless parallel coupled lines is expressed as [52]

$$\begin{bmatrix} A & B \\ C & D \end{bmatrix} = \begin{bmatrix} \frac{Z_{oe} + Z_{oo}}{Z_{oe} - Z_{oo}} & \frac{-j2Z_{oe}Z_{oo} \cot(\beta_c l_c)}{Z_{oe} - Z_{oo}} \\ j2 & \frac{Z_{oe} + Z_{oo}}{Z_{oe} - Z_{oo}} \\ \frac{(Z_{oe} - Z_{oo}) \cot(\beta_c l_c)}{Z_{oe} - Z_{oo}} & \frac{Z_{oe} - Z_{oo}}{Z_{oe} - Z_{oo}} \end{bmatrix} \quad (81)$$

where  $\beta_c$  is the phase constant of the coupled lines. Also, the  $ABCD$  matrix of the equivalent capacitive  $\pi$ -network is

$$\begin{bmatrix} A & B \\ C & D \end{bmatrix} = \begin{bmatrix} 1 + Z_g Y_p & Z_g \\ Y_p (2 + Z_g Y_p) & 1 + Z_g Y_p \end{bmatrix} \quad (82)$$

where  $Z_g = 1/j\omega C_g$ ,  $Y_p = j\omega C_p$ . In comparison of (81) and (82), the equivalent capacitances of the  $\pi$ -network are found as

$$C_g = \frac{Z_{oe} - Z_{oo}}{2\omega Z_{oe} Z_{oo} \cot(\beta_c l_c)} \text{ F} \quad (83a)$$

$$\text{and } C_p = \frac{1}{\omega Z_{oe} \cot(\beta_c l_c)} \text{ F.} \quad (83b)$$

Furthermore, combining the equivalent circuits of the single transmission line and coupled lines shown in Figs. 66(a) and (b), the equivalent circuit of the stepped impedance hairpin resonator in terms of lumped elements  $L$  and  $C$  is shown in Fig. 66(c), where  $C_{ps} = C_p + C_s + C_\Delta$  is the sum of the capacitances of the single transmission line, coupled lines and the junction discontinuity ( $C_\Delta$ ) [81] between the single transmission line and the coupled lines.

The physical dimensions of the filter can be synthesized by using the available L-C tables and (80) and (83). The widths of the single transmission line and coupled lines of the filter can be obtained from selecting the impedances that satisfy the condition  $Z_s > \sqrt{Z_{oe} Z_{oo}}$ . The lengths of the single transmission line and coupled lines of the filter transformed from (80a) and (83b) are

$$l_s = \frac{\sin^{-1}(\omega_c L_{st} / Z_s)}{\beta_s} \quad (84a)$$

$$\text{and } l_c = \frac{\tan^{-1}[\omega_c Z_{oe} (C_{pst} - C_s - C_\Delta)]}{\beta_c} \quad (84b)$$

where  $\omega_c$  is the 3 dB cut-off angular frequency,  $L_{st}$  and  $C_{pst}$  are the inductance and capacitance chosen from the available L-C tables.  $C_s$  and  $C_g$  can be calculated from (84a), (80b) and (84b), (83a), respectively.

C. Compact Elliptic-Function Lowpass Filters

1) Lowpass Filter Using One Stepped Impedance Hairpin Resonator

Fig. 67 shows the geometry and equivalent circuit of the elliptic-function lowpass filter using one stepped impedance hairpin resonator with feed lines  $l_f$ .

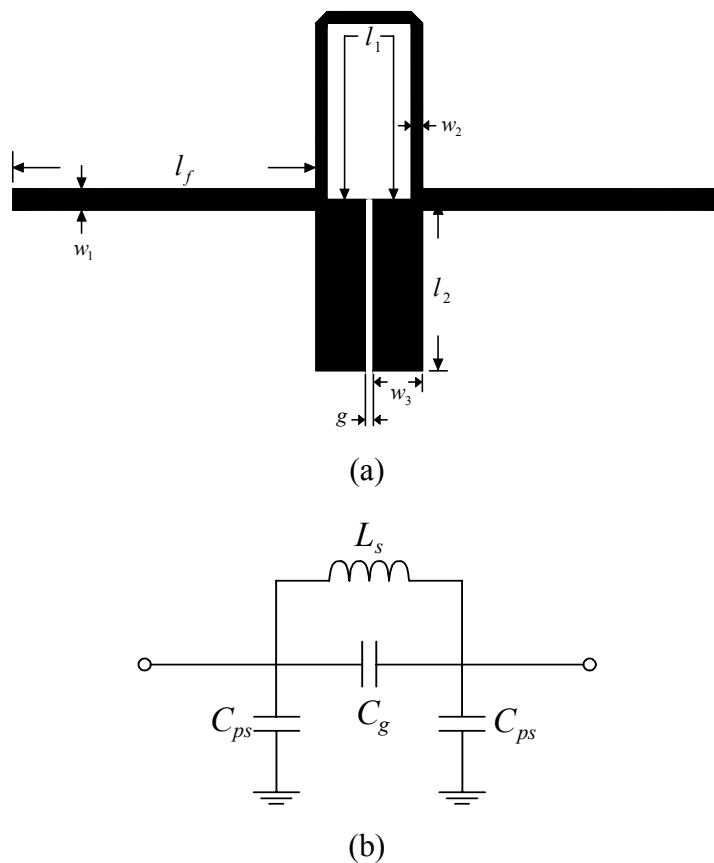


Fig. 67. The lowpass filter using one hairpin resonator (a) layout and (b) equivalent circuit.

As seen from the equivalent circuit in Fig. 67(b),  $L_s$  is the equivalent inductance of the single transmission line of the filter.  $C_g$  is the equivalent capacitance of the coupled lines and  $C_{ps}$  is sum of the capacitances of the transmission line  $l_l$  and the coupled lines. Using the available elliptic-function element-value tables [95] with impedance and frequency scaling, the dimensions of the prototype lowpass filter can be approximately synthesized by (80), (83) and (84). The exact dimensions are adjusted to optimize the performance of the filter using EM simulation software IE3D [35] to account for the loss and the discontinuity effects not included in the lumped-element model of Fig. 67(b). The lowpass filter is designed for a 3-dB cut-off frequency of 2 GHz and fabricated on a 25mil thick RT/Duroid 6010.2 substrate with relative dielectric constant  $\epsilon_r = 10.2$ .

Table X shows the equivalent L-C values from the available L-C tables, approximated L-C values, and optimized L-C values, respectively. Observing the available L-C tables, the filter using one microstrip hairpin resonator is difficult to synthesize. An approximate synthesis is introduced by using some inductances and capacitances chosen from the available L-C tables and (80), (83), (84). For instance, using the inductance and capacitance  $L_s$  and  $C_{ps}$  in the available L-C tables, the lengths of the single and coupled lines can be found from (84) and (80b). Also, the capacitance  $C_g$  can be obtained from (83a).

Table X L-C values of the filter using one hairpin resonator

	$C_{ps}$	$C_g$	$L_s$
Available L-C tables	1.52 pF	0.13 pF	4.2 nH
Approximated L-C values	1.52 pF	0.22 pF	4.2 nH
Optimized L-C values	2.23 pF	0.34 pF	4.87 nH

Fig. 68 shows the simulated frequency responses of the filter using L-C values in Table X. The simulated frequency response of the filter with the available L-C tables is obtained using the Agilent ADS circuit simulator. The simulated frequency responses of the filter with the approximated and optimized L-C values are obtained using the IE3D EM simulator.

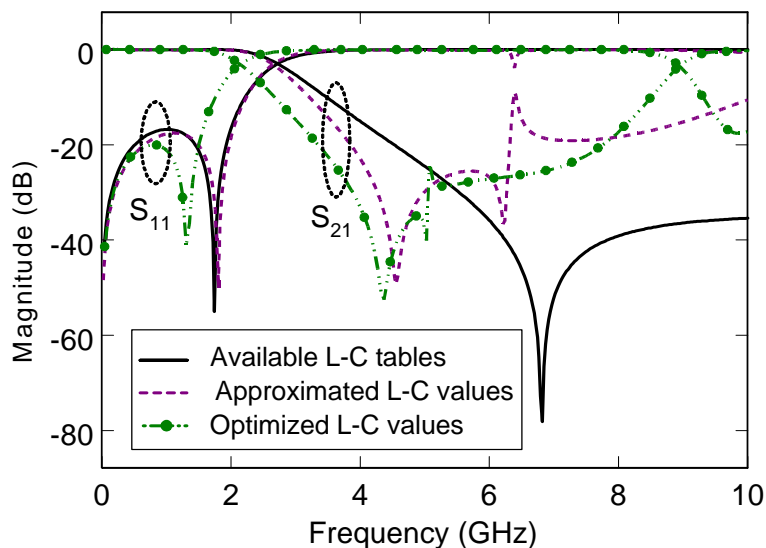
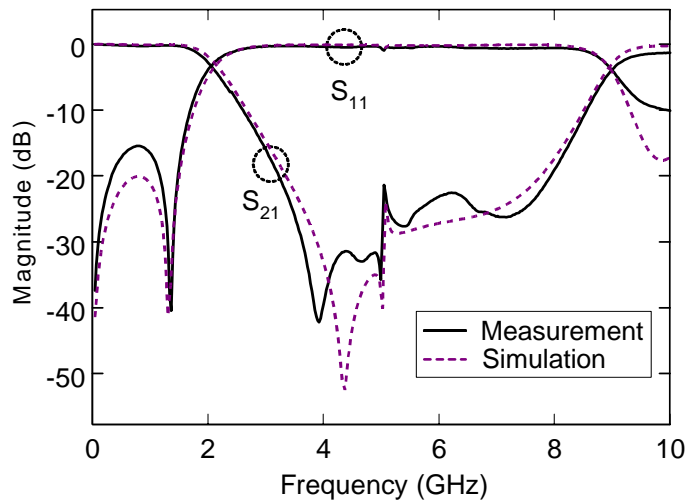


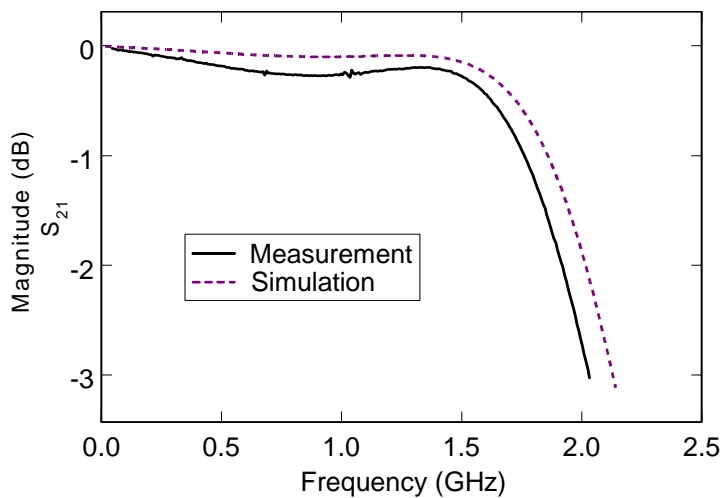
Fig. 68. Simulated frequency responses of the filter using one hairpin resonator.

Observing the simulated results in Fig. 68, the equal ripple response of the microstrip filter at the stopband is affected by the harmonics of the filter. The optimized filter with larger L-C values has a closer 3dB cut-off frequency at 2 GHz and a better return loss. The optimized dimensions of the filter are  $l_f = 8$  mm,  $l_1 = 11.92$  mm,  $l_2 = 4.5$  mm,  $w_1 = 0.56$  mm,  $w_2 = 0.3$  mm,  $w_3 = 1.31$  mm and  $g = 0.2$  mm. Fig. 69 shows the measured and simulated results of the filter with the optimized dimensions. Inspecting the measured results, the elliptic-lowpass filter has a 3-dB passband from DC to 2.03 GHz. The insertion loss is less than 0.3 dB, and the return loss is better than 15 dB from DC to 1.57

GHz. The rejection is greater than 20 dB within 3.23-7.93GHz. The ripple is  $\pm 0.14$  dB as shown in Fig. 69(b).



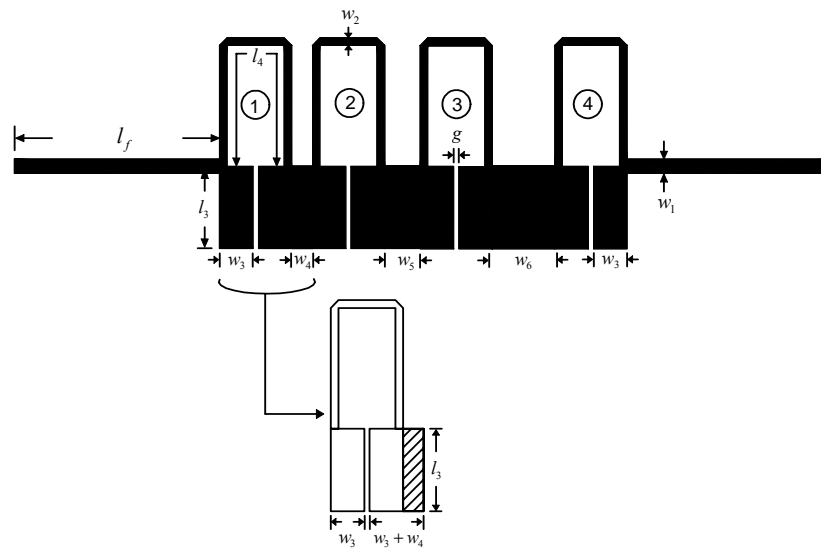
(a)



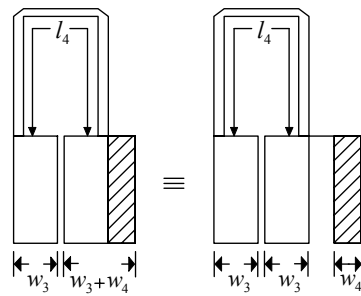
(b)

Fig. 69. Measured and simulated (a) frequency response and (b)  $S_{21}$  within the 3-dB bandwidth for the filter using one hairpin resonator.

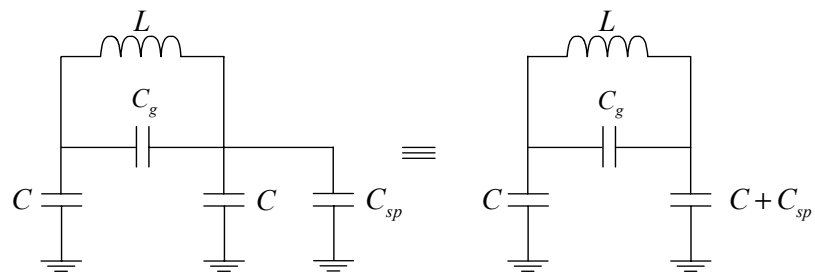




(a)



(b)



(c)

Fig. 70. The lowpass filter using cascaded hairpin resonators (a) layout, (b) asymmetric coupled lines, and (c) equivalent circuit of the asymmetric coupled lines.

2) *Lowpass Filter Using Multiple Cascaded Stepped Impedance Hairpin Resonators*

Fig. 70(a) shows the lowpass filter using four multiple cascaded stepped impedance hairpin resonators. Inspecting this structure, two resonators are linked by an adjacent transmission line with width of  $w_4$ ,  $w_5$ , or  $w_6$ . Due to the adjacent transmission line, the coupled lines become an asymmetrical coupling structure as shown on the left side of Fig. 70(b). The asymmetrical coupled lines can be roughly treated as a symmetric coupled lines with a separate parallel single transmission line as shown on the right side of the Fig. 70(b) [96]. Therefore, as seen in Fig. 70(c), the equivalent circuit of the asymmetric coupled lines can be approximately represented by that of the symmetric coupled lines in Fig. 66(b) and a equivalent capacitance  $C_{sp}$  of a single transmission line in shunt. The equivalent capacitance  $C_{sp}$  is given by

$$C_{sp} = \epsilon_0 \epsilon_r w/h \text{ (F/unit length)} \quad (85)$$

where  $w$  is the width of the adjacent transmission line and  $h$  is the substrate thickness. The equivalent circuit of the lowpass filter is illustrated in Fig. 71.

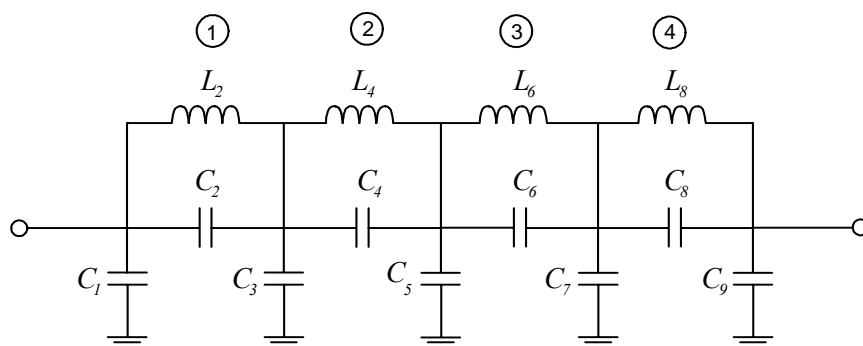


Fig. 71. Equivalent circuit of the lowpass filter using cascaded hairpin resonators.

Table XI shows the available L-C tables, approximated L-C values, and optimized L-C values of the filter using four cascaded hairpin resonators. Also, observing the available L-C tables, the inductances and capacitances between resonators show a high variation, which is difficult to synthesize a lowpass filter using cascaded microstrip hairpin resonators. For example, by using the inductances and capacitances  $L_2, L_4, L_6, L_8, C_1, C_3, C_5, C_7, C_9$  in the available tables and (84), (85), the capacitances  $C_4$  and  $C_6$  calculated from (83a) are very small. In this case, the 3 dB cut-off frequency of the filter is larger than that of the filter using the available L-C tables. Moreover, if the filter is synthesized by using the inductances and capacitances  $L_2, L_4, L_6, L_8, C_2, C_4, C_6, C_8$  in the available tables and (80b), (84a), (85), (86), then the capacitances  $C_3, C_5,$  and  $C_7$  will become large, where (86) transformed from (83a) for the synthesized length of the coupled lines is given by

$$l_c = \frac{\tan^{-1}[2\omega_c C_{gt} Z_{oe} Z_{oo} / (Z_{oe} - Z_{oo})]}{\beta_c} \quad (86)$$

where  $C_{gt}$  is the capacitance chosen from the available L-C tables. In this case, the 3 dB cut-off frequency of the filter will be smaller than that of the filter using the available L-C tables.

Table XI L-C values of the filter using four hairpin resonators

	$C_1$	$C_2$	$L_2$	$C_3$	$C_4$	$L_4$	$C_5$	$C_6$	$L_6$	$C_7$	$C_8$	$L_8$	$C_9$
Available L-C tables	1.98 pF	0.2 pF	5.07 nH	2.65 pF	1.21 pF	3.45 nH	1.95 pF	1.65 pF	2.9 nH	2.17 pF	0.74 pF	3.84 nH	1.56 pF
Approximated L-C values	1.98 pF	0.24 pF	5.07 nH	4.83 pF	0.61 pF	3.45 nH	4.97 pF	0.44 pF	2.9 nH	4.49 pF	0.45 pF	3.84 nH	2.16 pF
Optimized L-C values	1.79 pF	0.23 pF	4.89 nH	3.93 pF	0.23 pF	4.89 nH	4.48 pF	0.23 pF	4.89 nH	3.93 pF	0.23 pF	4.89 nH	1.79 pF

To obtain a proper 3 dB cut-off frequency, an alternative approximate method is used. In the beginning, one can use the capacitance and inductance  $C_1, L_2$  in the available L-C tables and (80b), (83a), (84) to calculate  $C_2, C_{s1}$  and  $C_{p1}$ , where the subscripts of  $s1$  and  $p1$  are the capacitances associated with the first resonator. Then, using  $C_3, L_4$  in the available L-C tables and (78b), (81a), (82), the capacitances  $C_4, C_{s2}$  and  $C_{p2}$  can be obtained. Thus, the total synthesized value for  $C_3$  is given by

$$C_3(\text{syn.}) = C_{p1} + C_{s1} + 2C_{\Delta} + C_{p2} + C_{s2} + C_{sp} l_c. \quad (87)$$

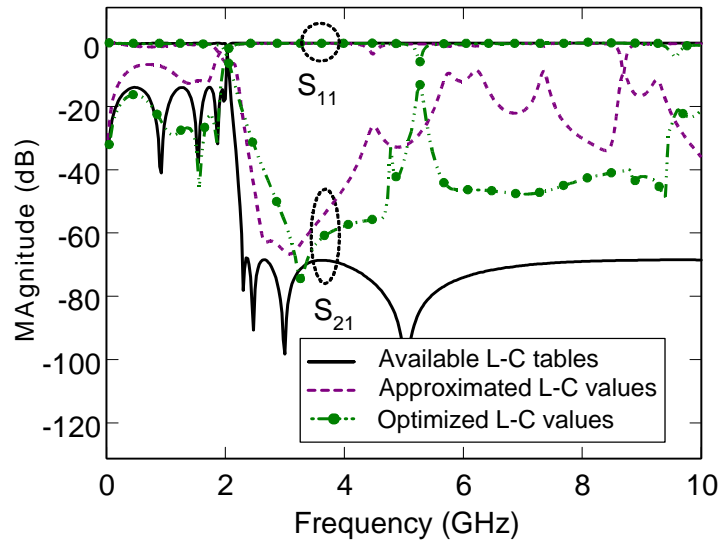


Fig. 72. Simulated frequency responses of the filter using four cascaded hairpin resonators.

Furthermore, by adjusting the capacitance  $C_{sp}$  value (size of a adjacent microstrip line), one can obtain  $C_3$  (L-C tables) =  $C_3$  (syn.). If the sum of the capacitances  $C_{p1} + C_{s1} + 2C_{\Delta} + C_{p2} + C_{s2}$  is large than  $C_3$  (L-C tables), the capacitance  $C_{sp}$  may be selected by a proper size of a microstrip line to link two resonators. The rest of the synthesized L-C values can be found by using the same procedure. Fig. 72 shows the

simulated frequency responses of the filter using the available L-C tables, approximated L-C values, and optimized L-C values shown in Table XI. Observing the simulated results of the filter using the approximated L-C values in Fig. 72, they show a 3 dB cut-off frequency close to 2 GHz but with harmonics at the stopband. These harmonics at the stopband are due to the different L-C values (sizes) of the hairpin resonators.

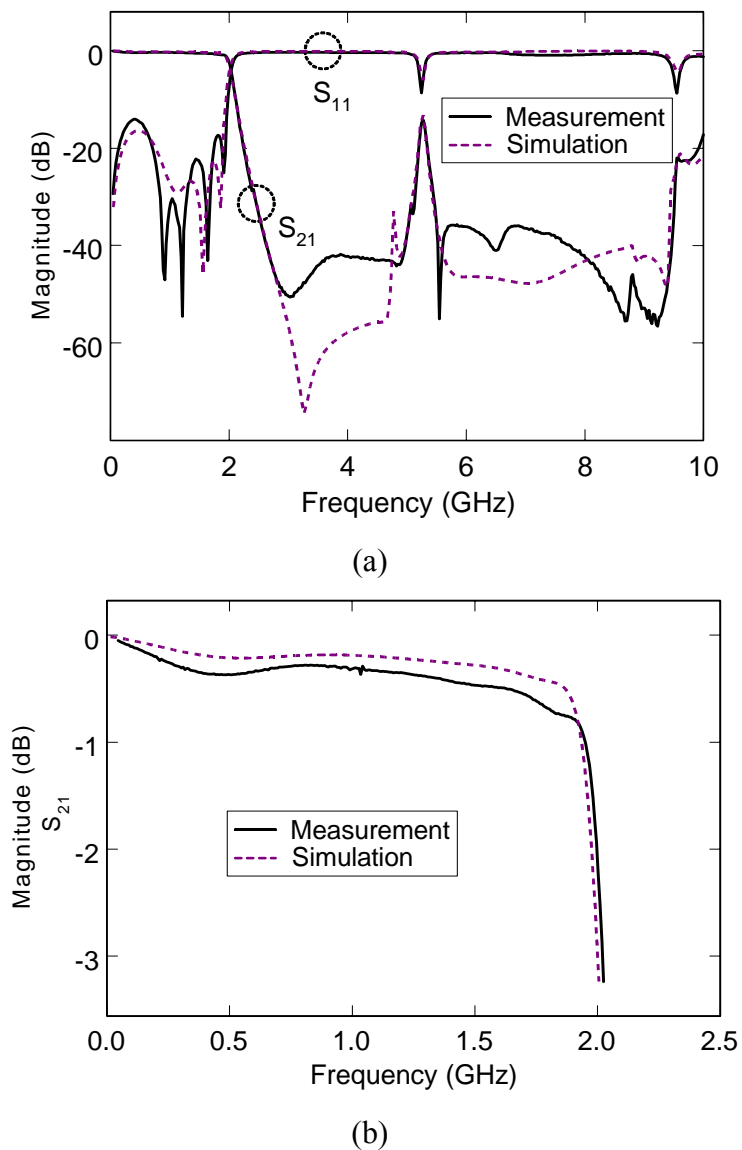


Fig. 73. Measured and simulated (a) frequency response and (b)  $S_{21}$  within the 3-dB bandwidth for the filter using cascaded hairpin resonators.

To reduce the harmonics at the stopband, an optimized filter constructed by identical hairpin resonators is used. Furthermore, during the optimization, it can be found that the filter can achieve a low return loss by using a long single transmission line and short coupled lines. The optimized L-C values are listed in Table XI. Inspecting the simulated results in Fig. 72, the optimized filter using identical hairpin resonators can reduce harmonics at the stopband and provide a low return loss in the passband.

The optimized dimensions of the filter in Fig. 70(a) are  $l_3 = 3.2$  mm,  $l_4 = 12.02$  mm,  $w_4 = w_6 = 0.8$  mm,  $w_5 = 2$  mm.  $l_f$ ,  $w_1$ ,  $w_2$ ,  $w_3$  and  $g$  are the same dimensions as before. The measured and simulated frequency responses of the optimized filter are shown in Fig. 73. This lowpass filter provides a much sharper cut-off frequency response and deeper rejection band compared to the results of using one hairpin resonator given in the part 1 of this section. This filter has a 3-dB passband from DC to 2.02 GHz. The return loss is better than 14 dB from DC to 1.96 GHz. The insertion loss is less than 0.6 dB. The rejection is greater than 42 dB from 2.68 to 4.93 GHz. The ripple is  $\pm 0.23$  dB as shown in Fig. 73(b).

### 3) *Broad Stopband Lowpass Filters*

Observing the frequency response of the lowpass filter in Fig. 73, the stopband bandwidth is limited by harmonics, especially for the second harmonic. In order to extend the stopband bandwidth, additional attenuation poles at the second harmonic can be added. The additional attenuation poles can be implemented by additional lowpass filter using two cascaded hairpin resonators with a higher 3-dB cut-off frequency and attenuation at the second harmonic as shown in Fig. 74. The desired higher 3-dB cut-off and attenuation frequencies of the additional lowpass filter can be obtained by using similar synthesis procedure as in part 2 of this section. The optimized dimensions of the additional lowpass filter are  $l_5 = 2.55$  mm,  $l_6 = 10.02$  mm,  $w_7 = 0.5$  mm  $l_f$ ,  $w_1$ ,  $w_2$ ,  $w_3$  and  $g$  have the same dimensions as before in part 2 of this section.

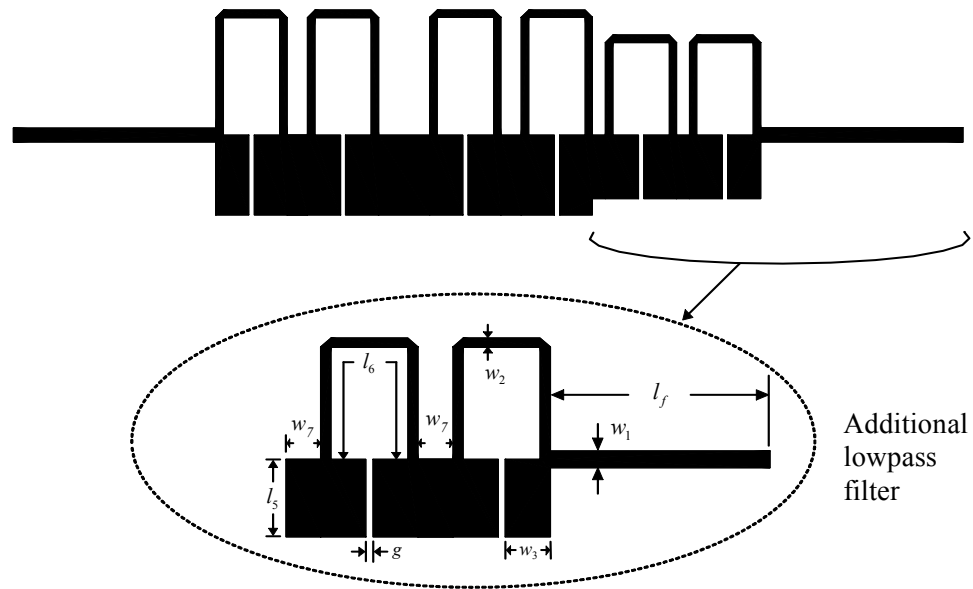
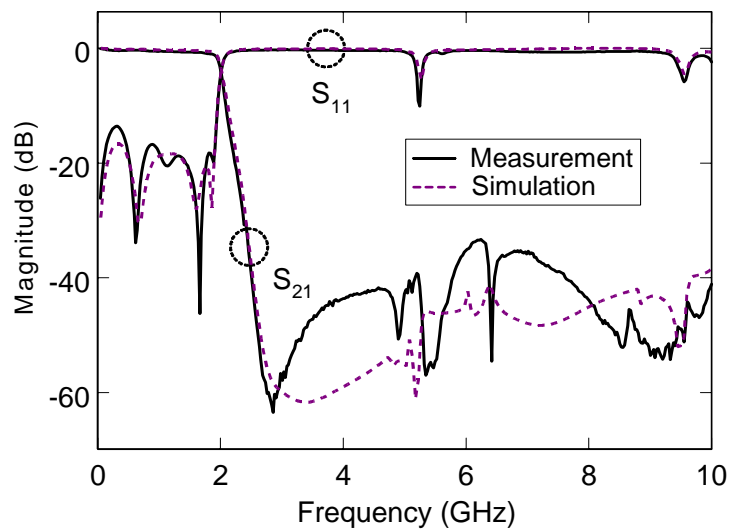
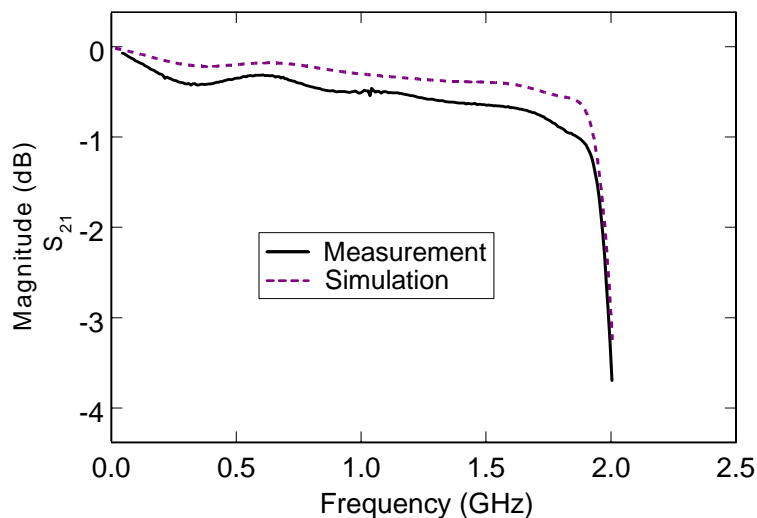


Fig. 74. Layout of the lowpass filter with additional attenuation poles.

Fig. 75(a) shows the measured and simulated results. The additional lowpass filter attenuates the level of the second harmonic and achieve a wider stopband bandwidth with attenuation better than 33.3 dB from 2.45 to 10 GHz. The return loss of the filter is greater than 13.6 dB within DC-1.94 GHz. The insertion loss is less than 1 dB. As seen in Fig. 75(b), the ripple is  $\pm 0.33$  dB.



(a)



(b)

Fig. 75. Measured and simulated (a) frequency response and (b)  $S_{21}$  within the 3-dB bandwidth for the filter with additional attenuation poles.

#### D. Conclusions

Compact elliptic-function lowpass filters using stepped impedance hairpin resonators are proposed. The filters are synthesized and optimized from the equivalent lumped-element model using the available element-value tables and EM simulation. The lowpass filter using multiple cascaded stepped impedance hairpin resonators shows a



very sharp cut-off frequency response and low insertion loss. Moreover, with additional attenuation poles, the lowpass filter can obtain a wide stopband bandwidth. The measured results of the lowpass filters agree well with simulated results. The useful equivalent circuit model for the stepped impedance hairpin resonator provides a simple method to design filters and other circuits.

## CHAPTER IX

PIEZOELECTRIC TRANSDUCER TUNED FEEDBACK MICROSTRIP RING  
RESONATOR OSCILLATORS\**A. Introduction*

In the past years, many different oscillators using dielectric or microstrip ring resonators have been reported. Due to their advantages of low cost, good temperature stability, and easy fabrication, they are widely used in many RF and microwave systems. The push-push type of the dielectric resonator is used in many oscillator designs [97-99]. However, due to the physical geometry of the dielectric resonator, it is not easy to mount a varactor on the dielectric resonator to tune the oscillator frequency [100]. Recently, the push-push microstrip ring resonator oscillators were proposed [101,102]. The oscillator using a ring resonator is easier to fabricate than that of dielectric resonator in hybrid or monolithic circuits. Moreover, a varactor can be easily mounted on a resonator to tune the oscillation frequency [101]. In addition to the push-push type oscillators, the feedback oscillators were also widely used in many RF and microwave systems due to the simplicity of the circuit design [103,104].

Electronically tunable resonators and oscillators using varactors have been reported [9,105,106,107]. However, mounting varactors on the resonator requires some slits to be cut in the resonator and additional bias circuits. These modifications directly affect the resonant frequencies of the resonator and make the resonator circuit more complicated. Recently, a piezoelectric transducer tuned oscillator was reported [108]. The oscillator

---

\*Reprinted with permission from (complete publication information) “High efficiency piezoelectric transducer tuned feedback microstrip ring resonator oscillators operating at high resonant frequencies” by Lung-Hwa Hsieh and Kai Chang, 2003. *IEEE Trans. Microwave Theory Tech.*, vol. 51, pp. 1141- 1145. © 2004 by the IEEE.

tuned by a voltage controlled piezoelectric transducer tuning without any cutting slit and bias circuit on the resonator provides a wide tuning range.

In this chapter, a voltage controlled piezoelectric transducer tuned microstrip ring resonator oscillator using a feedback structure is introduced. This new oscillator consists of a ring resonator with two orthogonal feed lines, a feedback configuration and a voltage controlled piezoelectric transducer. A close-loop ring resonator using a pair of orthogonal feed lines suppresses odd resonant frequencies and operates at even resonant frequencies. This operation has a similar characteristic of high operating resonant frequencies as that of the push-push oscillators. A simple transmission-line model is used to predict the high operating resonant frequency characteristic of the ring resonator using the orthogonal feeding structure. The measured and simulated results agree well. The oscillator has a high DC to RF efficiency of 48.7 % at 12.09 GHz with a power output of 5.33 dBm. A voltage controlled piezoelectric transducer is used to change the effective dielectric constant of the ring resonator and vary the resonant frequencies of the resonator.

### B. Ring Resonator with Orthogonal Feed Lines

As seen in Fig. 76, the closed-loop ring resonator with total length of  $l = n\lambda_g$  is fed by two orthogonal feed lines, where  $n$  is the mode number and  $\lambda_g$  is the guided-wavelength. The ring resonator fed by the input and output feed lines represents a shunt circuit, which consists of the upper and lower sections of  $l_1 = 3n\lambda_g/4$  and  $l_2 = n\lambda_g/4$ , respectively. The total  $Y$  parameters of the ring circuit are calculated from the individual  $Y$  parameters of the upper and lower sections and are given by

$$\begin{bmatrix} Y_{11} & Y_{12} \\ Y_{21} & Y_{22} \end{bmatrix} = \begin{bmatrix} -jy_o(\cos \beta l_1 + \cot \beta l_2) & jy_o(\csc \beta l_1 + \csc \beta l_2) \\ jy_o(\csc \beta l_1 + \csc \beta l_2) & -jy_o(\cos \beta l_1 + \cot \beta l_2) \end{bmatrix} \quad (88)$$

where  $\beta$  is the propagation constant,  $y_o$  is the characteristic admittance of the ring resonator.

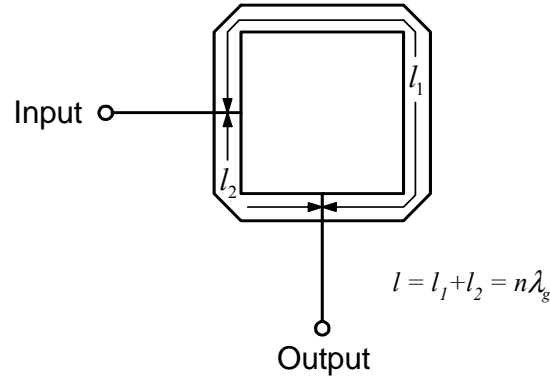


Fig. 76. Configuration of the ring resonator fed by two orthogonal feed lines.

Furthermore,  $S_{21}$  of the ring circuit can be found from (88) and is expressed as

$$S_{21} = \frac{-j2(\csc \frac{3n\pi}{2} + \csc \frac{n\pi}{2})}{[1 - j(\cot \frac{3n\pi}{2} + \cot \frac{n\pi}{2})]^2 + [\csc \frac{3n\pi}{2} + \csc \frac{n\pi}{2}]^2} \quad (89)$$

$$\text{For odd-mode excitation, } |S_{21}| = 0, \quad n = 1, 3, 5, \dots \quad (90a)$$

$$\text{and for even-mode excitation, } |S_{21}| = 1, \quad n = 2, 4, 6, \dots \quad (90b)$$

The calculated results in (90) show that the ring resonator fed by two orthogonal feed lines can suppress the odd mode resonant frequencies and operate at even mode resonant frequencies only. This operation has a similar characteristic of high operating resonant frequencies as that of the push-push oscillator [99]. Fig. 77 shows the layout of the ring circuit using two orthogonal feed lines with coupling gap size of  $s$ . The detail design regarding to the parallel coupling structure between the ring and the feed lines can be

found in [77]. This ring circuit was designed at the fundamental mode of 6 GHz and fabricated on a 20mil thick RT/Duroid 5870 substrate with a relative dielectric constant of  $\epsilon_r = 2.33$ . The dimensions of the ring circuit are  $l_1 = 27.38$  mm,  $l_2 = 9.13$  mm,  $l_f = 8$  mm,  $w = 1.49$  mm and  $s = 0.2$  mm.

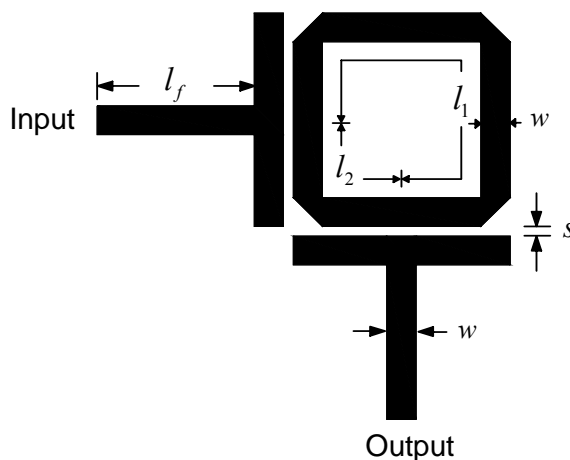


Fig. 77. Configuration of the ring resonator using enhanced orthogonal feed lines.

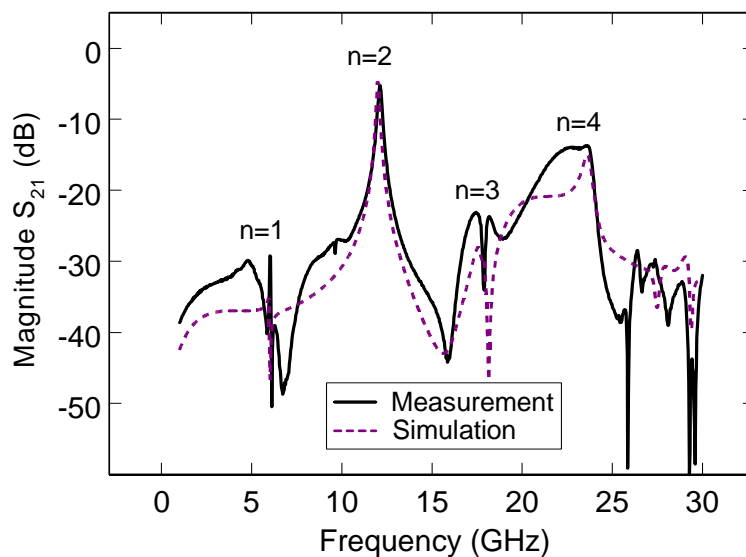


Fig. 78. Simulated and measured results for the ring resonator using enhanced orthogonal feed lines.

The measured and simulated results of this circuit are shown in Fig. 78. The simulation is performed using an EM simulator [35]. Observing the measured and simulated results, they agree well with each other. The results also agree with the predictions given by (90). The measured unloaded  $Q$  of the ring resonator is 125.2.

### C. Feedback Ring Resonator Oscillators

Fig. 79 shows the configuration of the feedback ring resonator oscillator. This configuration consists of a feedback ring circuit and a two-port negative-resistance oscillator with input and output matching networks. The high  $Q$  ring resonator is used to reduce the noise of the two-port negative-resistance oscillator. The active device used is a NE 32484A HEMT. The dimensions of the oscillator are  $l_3 = 3$  mm,  $l_4 = 6.95$  mm,  $l_5 = 15.19$  mm,  $l_6 = 10.69$  mm,  $l_7 = 7.3$  mm,  $l_8 = 9.47$  mm, and  $l_9 = 21.19$  mm.

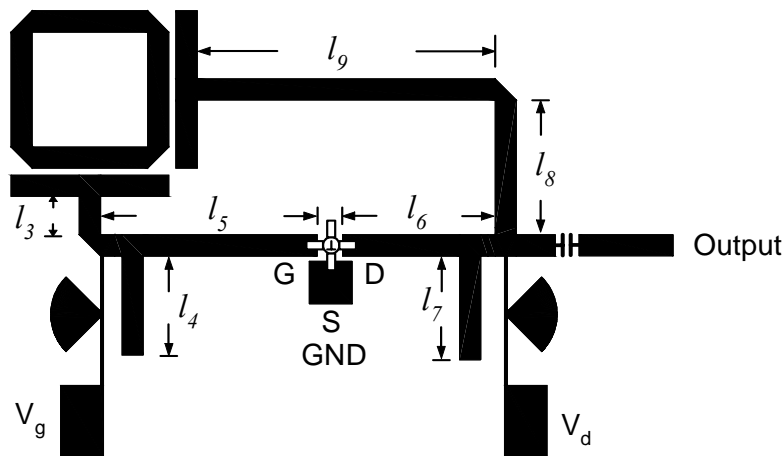


Fig. 79. A feedback ring resonator oscillator.

The two-port negative-resistance oscillator shown in Fig. 80(a) uses the one-open-end S terminal as a series-feedback element to obtain a potential instability. Also, with input and output matching networks, the two-port oscillator with an applied bias of  $V_{gs} =$

-0.65 V and  $V_{ds} = 1$  V has a negative resistance around 12 GHz as shown in Fig. 80(b). The simulated results were performed using the measured S parameters of the transistor, Agilent ADS, and IE3D. Inspecting the results in Fig. 78 and 80(b), the feedback loop from the drain through the ring circuit to the gate maintains oscillation as  $S_{21r} S_{21o} > 1$ , where  $S_{21r} = -5.2$  dB is the loss of the ring circuit and  $S_{21o} = 20.3$  dB is the gain of the two-port negative-resistance oscillator.

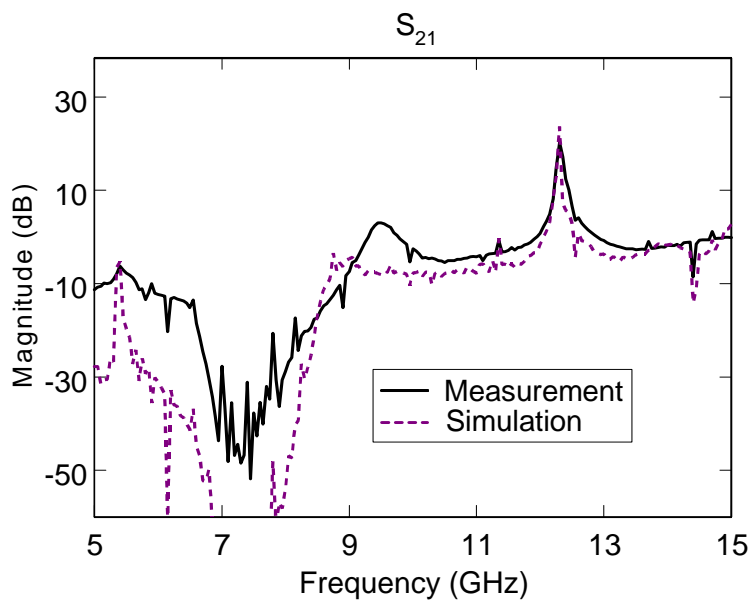
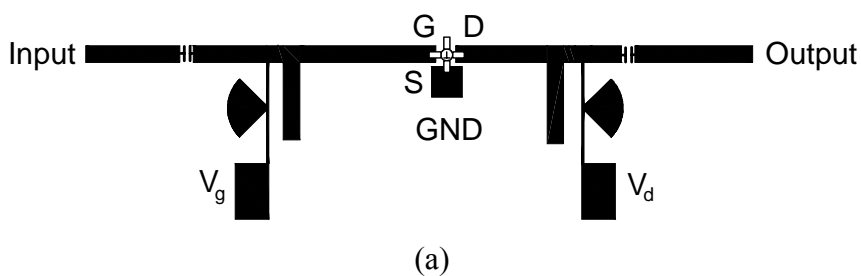


Fig. 80. Two-port negative-resistance oscillator (a) layout and (b) measured and simulated results.

Fig. 81 shows the measured efficiency and oscillation frequency as a function of  $V_{gs}$  with a fixed  $V_{ds}=1.5$  V. The highest DC-to-RF efficiency is 43.3 % with output power of 7.7 dBm at the oscillation frequency of 12.1 GHz. Also, Fig. 82 shows the measured efficiency and oscillation frequency as a function of  $V_{ds}$  with a fixed  $V_{gs} = -0.4$  V. The highest DC-to-RF efficiency is 41.4 % with output power of 6.17 dBm at the oscillation frequency of 12.104 GHz. Inspecting the equation of the DC-to-RF efficiency in (91), if the decreasing rate of  $I_{ds}V_{ds}$  is faster than that of the RF output power,  $P_{out}$ , then oscillators can possibly research to a high DC-to-RF efficiency.

$$\text{Efficiency} = \eta(\%) = \frac{P_{out}}{I_{ds}V_{ds}} \times 100\% . \quad (91)$$

Observing the results in Figs. 81, 82 and (91), the maximum efficiency can be obtained by selecting a low  $V_{gs}$  and  $V_{ds}$ .

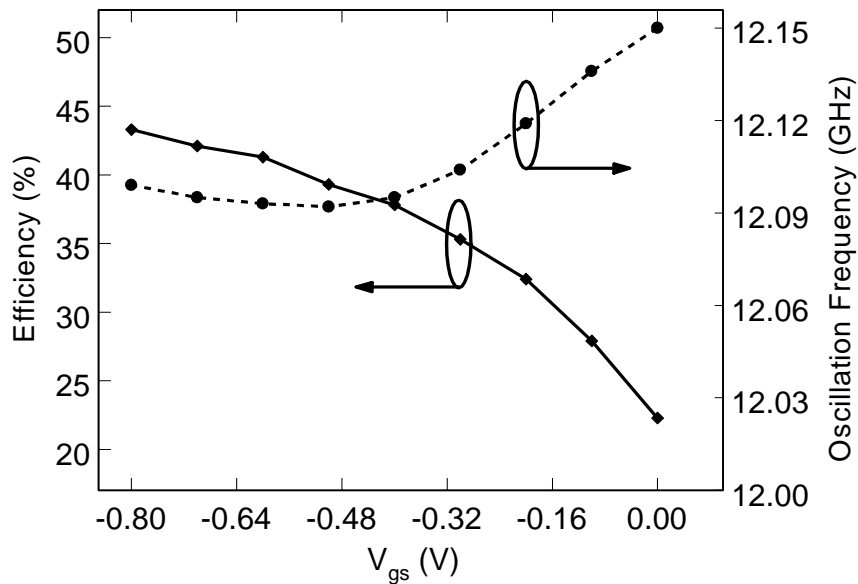


Fig. 81. Measured DC-to-RF efficiency and oscillation frequency versus  $V_{gs}$  with  $V_{ds} = 1.5$  V.



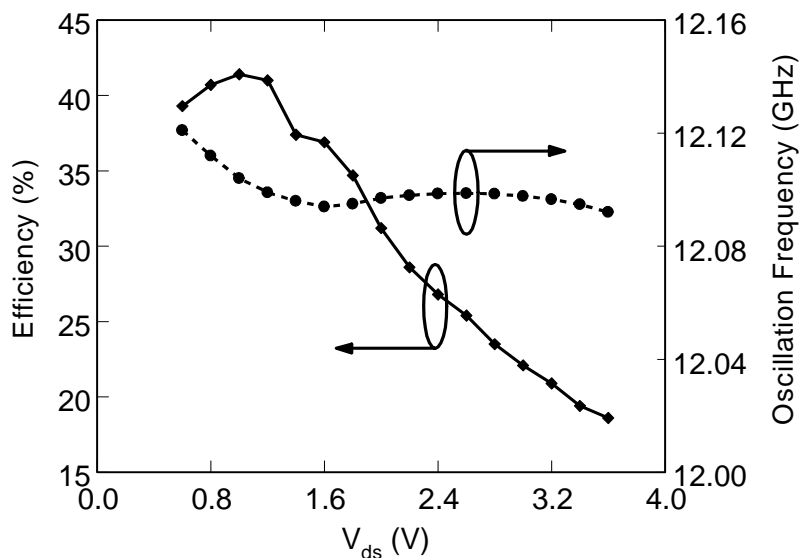


Fig. 82. Measured DC-to-RF efficiency and oscillation frequency versus  $V_{ds}$  with  $V_{gs} = -0.4$  V.

Fig. 83 shows the measured spectrum of the oscillator with applied voltages of  $V_{gs} = -0.65$  V and  $V_{ds} = 1$  V. Also, as shown in Fig. 83, the oscillator is operated at the second harmonic of the ring resonator. The oscillator has the efficiency of 48.7 % with output power of 3.41 mW at 12.09 GHz. The phase noise of the oscillator is -96.17 dBc/Hz at offset frequency of 100KHz. The second and third harmonics of the oscillator are 22.8 dB and 15.1 dB down from the fundamental oscillation frequency. These harmonics have less effect on the fundamental oscillation frequency. Comparing with other oscillators [104], this oscillator provides a high DC-to-RF efficiency.

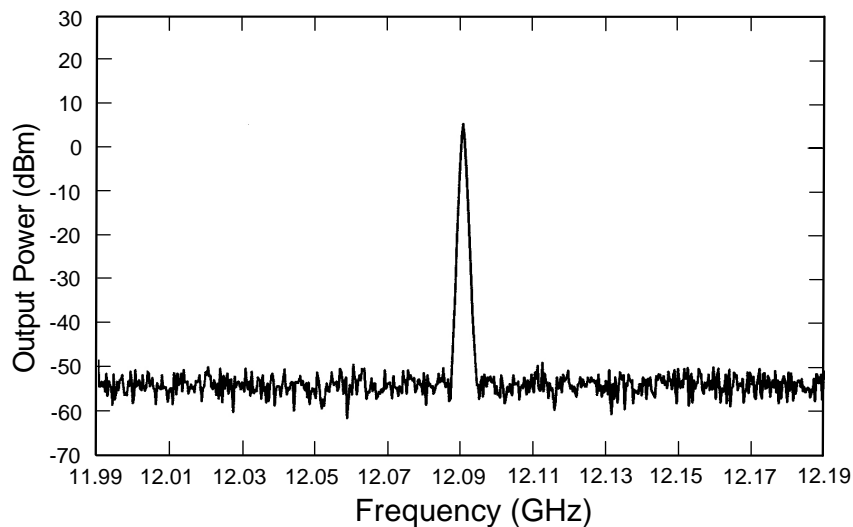


Fig. 83. Output power for the feedback ring resonator oscillator operated at the second harmonic of the ring resonator.

#### *D. Tunable Feedback Ring Resonator Oscillators Using a Piezoelectric Transducer*

Fig. 84 shows the configuration of the ring resonator oscillator integrated with a piezoelectric transducer (PET) with an attached dielectric perturber. The PET is a composition of lead, zirconate, and titanate [73]. The PET shown in Fig. 84 consists of two piezoelectric layers and one shim layer. The center shim laminated between the two same polarization piezoelectric layers adds mechanical strength and stiffness. Also, the shim is connected to one polarity of a DC voltage to deflect the PET and move it up or down vertically. This motion makes it possible to change the effective dielectric constant of the ring resonator [74], thus varying resonant frequency of the ring resonator. The PET can be deflected over  $\pm 1.325$  mm at  $\pm 90$  V with  $1\mu\text{A}$ .

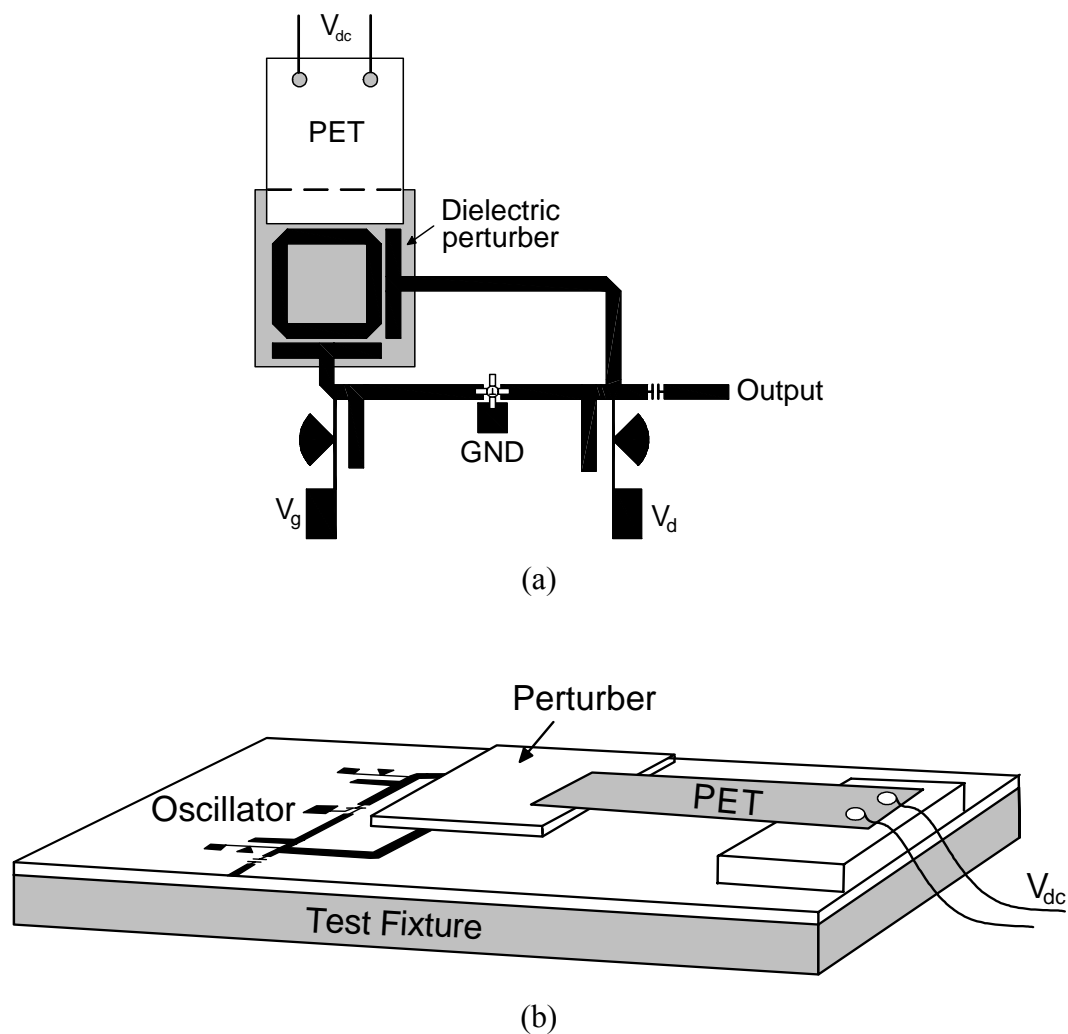


Fig. 84. Configuration of the tunable oscillator using a PET (a) top view and (b) 3 D view.

Fig. 85 shows the measured results of the oscillator using the PET tuning. The perturber attached on the PET has a dielectric constant of  $\epsilon_r = 10.8$  and thickness of  $h = 50$  mil. The tuning range of the oscillator is from 11.49 GHz (+90 V) with a power output of 3.17 dBm to 12 GHz (0 V) with a power output of 5.33 dBm.

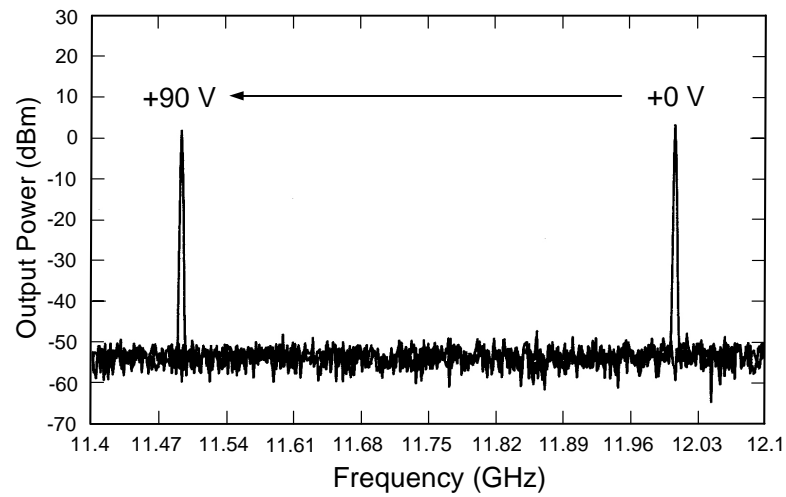


Fig. 85. Measured tuning range of 510 MHz for the tunable oscillator using a PET.

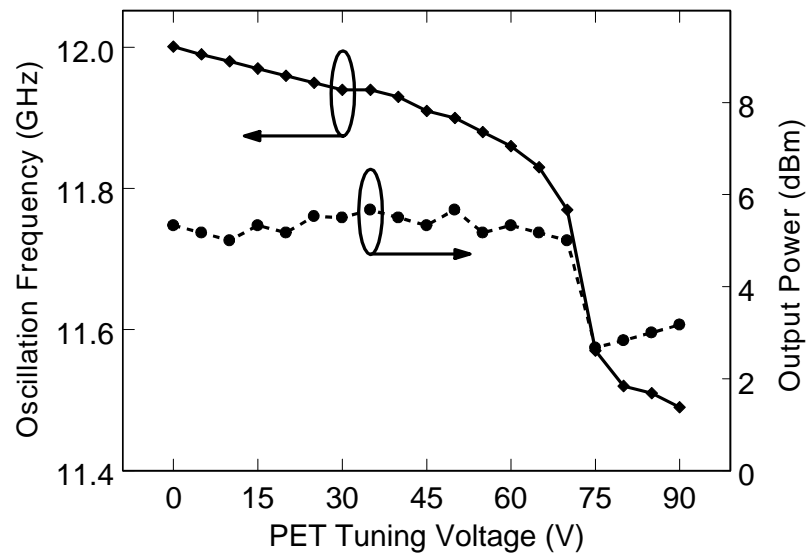


Fig. 86. Tuning oscillation frequencies and output power levels versus PET tuning voltages.

Fig. 86 shows the tunable oscillation frequencies and output power levels versus PET tuning voltages. As seen in Fig. 84, the PET tuning range is about 4.25 % around the oscillation frequency of 12 GHz and the output power is varied from 2.67 to 5.33 dBm.

This good tuning range is due to a wide area perturbation on the whole ring that significantly tunes the resonant frequency of the ring. In addition, by using a higher dielectric perturber, a wider tuning range and a lower DC applied voltage could be achieved [109].

#### *E. Conclusions*

A tunable feedback microstrip ring resonator oscillator has been developed. The new oscillator has the advantages of operating at second resonant frequency, high efficiency, and low cost. The high operating resonant frequency characteristic is studied and predicted by a simple transmission-line model. The simulated and measured results agree well with each other. The new oscillator operated at the fixed frequency of 12.09 GHz has a high efficiency of 48.7 % and an output power of 5.33 dBm. A voltage controlled piezoelectric transducer tuning provides a maximum perturbation on the ring and shows a good tuning range. Unlike the varactor-tuned oscillators, the new oscillator without any additional circuit on the resonator will not affect the natural resonant frequencies of the resonator. The tuning range of the PET-tuned oscillator is 4.25 % around the oscillation frequency of 12 GHz. The VCO should be useful in many wireless and sensor systems.

## CHAPTER X

## SUMMARY

In this dissertation, the analysis and modeling of the microstrip ring resonator has been introduced. The analysis and modeling methods for the ring resonator include a transmission-line model,  $ABCD$ ,  $Y$  parameter conversions, EM simulation, and so on. These simple methods and available commercial EM simulator provide a powerful tool to help designers to understand how the ring circuits operate. In addition, through those methods, new structures of the ring circuits have been invited applied to construct passive and active filters, and oscillators. These new filters and oscillators should be useful in many wireless systems.

A simple transmission-line model has been used to calculate the frequency modes of microstrip ring resonators of any shape for annual, square, and meander. A literature error for the frequency modes of the one-port ring resonator has been found. Moreover, the transmission-line model provides a better dual-mode explanation than the magnetic-wall model.

A simple lumped-element circuit of the closed- and open-loop ring resonators has been derived. Using this equivalent lumped-element circuit, the equal unloaded  $Q$ s of the close- and open-loop ring resonators were obtained. The useful equivalent lumped-element circuit of the ring resonators can provide a simple method to design ring circuits.

A new dual-mode filter using ring resonator with an enhanced L-shape coupling arm has been developed. The enhanced L-shape coupling arm not only provides enhanced couplings to reduce the insertion loss, but also generates a high selectivity characteristic. The filter using cascaded ring resonators with enhanced coupling function shows a sharp rejection and narrow passband.

New slow-wave bandpass filters using a microstrip line periodically loaded with ring or stepped impedance hairpin resonators have been proposed. The slow-wave bandpass filter is constructed by the parallel and series resonance characteristics of the resonators. These new bandpass filters have lower insertion loss than those of the filters using parallel- or cross-coupled filters.

A simple transmission-line model is used to calculate the locations of two transmission zeros to design a bandpass filter with a high selectivity. This filter using two resonators shows lower insertion loss than the cross-coupled filters using four resonators. A piezoelectric transducer (PET) is used to tune the passband of the filter.

A new compact, low insertion loss, high selectivity wideband bandpass filter has been introduced. The filter using direct-connected ring resonator with orthogonal feed lines and tuning stubs can obtain a wide passband and two stopbands. Due to the direct-connected feed lines, the filter can obtain a low insertion loss.

Compact elliptic-function filters using stepped impedance hairpin resonators have been developed. The filters are synthesized and optimized by using available element-value tables and EM simulation. The lowpass filter using cascaded stepped impedance hairpin resonators has a sharp rejection. In addition, by adding additional attenuation poles, the filter can obtain a wide stopband bandwidth. The measured results of the filter agree well with the simulated results.

A piezoelectric tuned feedback microstrip ring resonator oscillator has been fabricated and designed. The oscillator operates at the second harmonic frequency. The high operating resonator frequency characteristic of the ring resonator has been studied. In addition, a high efficiency and good tuning range have been obtained. This VCO is useful in many wireless systems.

## REFERENCES

- [1] P. Troughton, "Measurement technique in microstrip," *Electron. Lett.*, vol. 5, pp. 25-26, January 1969.
- [2] I. Wolff and N. Knoppik, "Microstrip resonator and dispersion measurements on microstrip lines," *Electron. Lett.*, vol. 7, pp. 779-781, December 1971.
- [3] W. Hoefer and A. Chattopadhyay, "Evaluation of the equivalent circuit parameters of microstrip discontinuities through perturbation of a resonant ring," *IEEE Trans. Microwave Theory Tech.*, vol. 23, pp. 1067-1071, December 1975.
- [4] K. Chang, F. Hsu, J. Berenz, and K. Nakano, "Find optimum substrate thickness for millimeter-wave GaAs MMICs," *Microwave & RF*, vol. 27, pp. 123-128, September 1984.
- [5] K. Chang, *Microwave Ring Circuits and Antennas*, New York: Wiley, 1996.
- [6] J. -S. Hong and M. J. Lancaster, "Microstrip bandpass filter using degenerate modes of a novel meander loop resonator," *IEEE Microwave Guided Wave Lett.*, vol. 5, pp. 371-372, November 1995.
- [7] J. -S. Hong and M. J. Lancaster, "Compact microwave elliptic function filter using novel microstrip meander open-loop resonators," *Electron. Lett.*, vol. 32, pp. 563-564, March 1996.
- [8] L. -H. Hsieh, B. H. Strassner, S. J. Kokel, C. T. Rodenbeck, M. Y. Li, K. Chang, F. E. Little, G. D. Arndt, and P. H. Ngo, "Development of a retrodirective wireless microwave power transmission system," in *IEEE AP-S Symp.*, June 2003, pp. 393 – 396.
- [9] Y. -S. Wu and F. J. Rosenbaum, "Mode chart for microstrip resonators," *IEEE Trans. Microwave Theory Tech.*, vol. 21, pp. 487-489, July 1973.
- [10] K. Chang, T. S. Martin, F. Wang, and J. L. Klein, "On the study of microstrip ring and varactor-tuned circuits," *IEEE Trans. Microwave Theory Tech.*, vol. 35, pp. 1288-1295, December 1987.
- [11] G. K. Gopalakrishnan and K. Chang, "Bandpass characteristics of split-modes in asymmetric ring resonators," *Electron. Lett.*, vol. 26, pp. 774-775, June 1990.



- [12] Z. M. Hejazi, P. S. Excell, and Z. Jiang, "Compact dual-mode filters for HTS satellite systems," *IEEE Microwave Guided Wave Lett.*, vol. 8, pp. 275-277, November 1998.
- [13] I. Wolff, "Microstrip bandpass filter using degenerate modes of a microstrip ring resonator," *Electron. Lett.*, vol. 8, pp. 163-164, June 1972.
- [14] L. Zhu and K. Wu, "A joint field/circuit model of line-to-ring coupling structures and its application to the design of microstrip dual-mode filters and ring resonator circuits," *IEEE Trans. Microwave Theory Tech.*, vol. 47, pp. 1938-1948, October 1999.
- [15] L. -H Hsieh and K. Chang, "Dual-mode elliptic-function bandpass filter using one single patch resonator without coupling gap," *Electron. Lett.*, vol. 36, pp. 2022 – 2023, November 2000.
- [16] L. -H. Hsieh and K. Chang, "Compact size and low insertion loss Chebyshev-function bandpass filters using dual-mode patch resonators," *Electron. Lett.*, vol. 37, pp. 1070 – 1071, August 2001.
- [17] I. Awai and T. Yamashita, "Two-stage bandpass filters based on rotated excitation of circular dual-mode resonators," *IEEE Microwave and Guided Wave Lett.*, vol. 7, pp. 212-213, August 1997.
- [18] G. K. Gopalakrishnan and K. Chang, "Novel excitation schemes for the microstrip ring resonator with lower insertion loss," *Electron. Lett.*, vol. 30, pp. 148-149, January 20, 1994.
- [19] J. -S. Hong and M. J. Lancaster, "Bandpass characteristics of new dual-mode microstrip square loop resonators," *Electron. Lett.*, vol. 31, pp 891-892, May 1995.
- [20] J. Y. Park and J. C. Lee, "A new enhanced coupling structure of microstrip ring resonator with two coupled lines and a slit," in *IEEE MTT-S Int. Microwave Symp. Dig.*, pp. 805-808, 1998.

- [21] W. C. Jung, H. J. Park and J. C. Lee, "Microstrip ring bandpass filters with new interdigital side-coupling structure," in *Asia Pacific Microwave Conf.*, vol. 3, pp. 678-681, 1999.
- [22] L. Nenet, D. Denis, L. Billonnet, B. Jarry and P. Guillon, "Analysis and optimization of noise and gain performances for various topologies of microwave ring resonator planar active filters," in *IEEE MTT-S Int. Microwave Symp. Dig.*, pp. 1223-1226, 1999.
- [23] A. Griol and J. Marti, "Microstrip multistage coupled ring active bandpass filters with harmonic suppression," *Electron. Lett.*, vol. 25, pp. 575-577, April 1999.
- [24] L. -H. Hsieh and K. Chang, "Simple analysis of the frequency modes for microstrip ring resonators of any general shape and the correction of an error in literature," *Microwave and Optical Tech. Lett.*, vol. 38, pp. 209 – 213, August 2003.
- [25] L. -H. Hsieh and K. Chang, "Equivalent lumped elements G, L, C and unloaded Qs of closed- and open-loop ring resonators," *IEEE Trans. Microwave Theory Tech.*, vol. 50, pp. 453 – 460, February 2002.
- [26] L. -H Hsieh and K. Chang, "A piezoelectric transducer tuned bandstop filter," *Electron. Lett.*, vol. 38, pp. 970-971, August 2002.
- [27] L. -H Hsieh and K. Chang, "Low-loss and high-selectivity bandpass filter with harmonic suppression and piezoelectric transducer tuning," *Electron. Lett.*, vol. 39, pp. 783-784, May 2003.
- [28] L. -H. Hsieh and K. Chang, "Tunable microstrip bandpass filters with two transmission zeros," *IEEE Trans. Microwave Theory Tech.*, vol. 51, pp. 520–525, February 2003.
- [29] L. -H Hsieh and K. Chang, "Compact, low insertion loss, sharp rejection wideband bandpass filters using dual-mode ring resonators with tuning stubs" *Electron. Lett.*, vol. 37, pp. 1345-1346, October 2001.

- [30] L. -H. Hsieh and K. Chang, "Compact, low insertion loss, sharp rejection and wideband microstrip bandpass filters" *IEEE Trans. Microwave Theory Tech.*, vol. 51, pp. 1241-1246, April 2003.
- [31] L. -H. Hsieh and K. Chang, "Compact, elliptic-function lowpass filters using microstrip stepped impedance hairpin resonators" *IEEE Trans. Microwave Theory Tech.*, vol. 51, pp. 193-199, January 2003.
- [32] L. -H. Hsieh and Kai Chang, "Compact, broad-stopband elliptic-function lowpass filters using microstrip stepped impedance hairpin resonators," in *IEEE MTT-S Int. Microwave Symp. Dig.*, pp. 1775-1778, June 2003.
- [33] L. -H. Hsieh and K. Chang, "High efficiency piezoelectric transducer tuned feedback microstrip ring resonator oscillators operating at high resonant frequencies," *IEEE Trans. Microwave Theory Tech.*, vol. 51, pp. 1141-1145, April 2003.
- [34] T. C. Edwards, "Microstrip measurements," in *MTT-S Int. Microwave Sym. Dig.*, pp.338-341, 1982.
- [35] *IE3D Version 9.16*, Zeland Software Inc., Fremont, California, July 2002.
- [36] C. C. Yu and K. Chang, "Transmission-line analysis of a capacitively coupled microstrip-ring resonator," *IEEE Trans. Microwave Theory Tech.*, vol. 45, pp. 2018-2024, November 1997.
- [37] G. Gonzalez, *Microwave Transistor Amplifiers Analysis and Design*, 2nd ed. New Jersey: Prentice-Hall, 1997.
- [38] D. M. Pozar, *Microwave Engineering*, 2nd ed. New York: Wiley, 1998.
- [39] R. Garg and I. J. Bahl, "Microstrip discontinuities," *Int. J. Electron.*, vol. 45, pp. 81-87, July 1978.
- [40] V. K. Trpathi and I. Wolff, "Perturbation analysis and design equations for open- and closed-ring microstrip resonators," *IEEE Trans. Microwave Theory Tech.*, vol. 32, pp. 405-409, April 1984.

- [41] E. Belohoubek and E. Denlinger, "Loss considerations for microstrip resonators," *IEEE Trans. Microwave Theory Tech.*, vol. 23, pp. 522-526, June 1975.
- [42] R. A. Pucel, D. J. Masse', and C. P. Hartwig, "Losses in microstrip," *IEEE Trans. Microwave Theory Tech.*, vol. 16, pp. 342-350, June 1968.
- [43] M. Kobayashi, "A dispersion formula satisfying recent requirements in microstrip CAD," *IEEE Trans. Microwave Theory Tech.*, vol. 36, pp. 1246-1250, August 1988.
- [44] E. Hammerstad and O. Jensen, "Accurate models for microstrip computer-aided design," *IEEE MTT-S Int. Microwave Symp. Dig.*, pp. 407-409, 1980.
- [45] I. J. Bahl and R. Garg, "Simple and accurate formulas for microstrip with finite strip thickness," *Proc. IEEE*, vol. 65, pp. 1611-1612, November 1977.
- [46] G. Tsuzuki, M. Suzuki, N. Sakakibara and Y. Ueno, "Novel superconducting ring filter," *IEEE MTT-S Int. Microwave Symp. Dig.*, pp. 379-382, 1998.
- [47] M. Reppel and H. Chaloupka, "Novel approach for narrowband super conducting filters," in *IEEE MTT-S Int. Microwave Symp. Dig.*, pp. 1563-1566, 1999.
- [48] F. Rouchaud, V. Madrangeas, M. Aubourg, P. Guillon, B. Theron, and M. Maignan, "New classes of microstrip resonators for HTS microwave filters applications," *IEEE MTT-S Int. Microwave Symp. Dig.*, pp. 1023-1026, 1998.
- [49] G. L. Matthaei, L. Young, and E. M. T. Jones, *Microwave filters, impedance-matching networks, and coupling structures*, New York: McGraw-Hill, 1980.
- [50] K. K. M. Cheng, "Design of dual-mode ring resonators with transmission zeros," *Electron. Lett.*, vol. 33, pp. 1392-1393, July 1997.
- [51] L. -H. Hsieh and K. Chang, "Compact dual-mode elliptic-function bandpass filter using a single ring resonator with one coupling gap," *Electron. Lett.*, vol. 36, pp. 1626-1627, September, 2000.
- [52] M. Sagawa, K. Takahashi, and M. Makimoto, "Miniaturized hairpin resonatorfilters and their application to receiver front-end MIC'," *IEEE Trans. Microwave Theory Tech.*, vol. 37, pp. 1991-1997, December, 1989.

- [53] M. Makimoto and S. Yamashita, *Microwave Resonators and Filters for Wireless Communication Theory, Design and Application*, Berlin: Springer, 2001.
- [54] C. -C. Yu and K. Chang, "Novel compact elliptic-function narrow-band bandpass filters using microstrip open-loop resonators with coupled and crossing lines," *IEEE Trans. Microwave Theory Tech.*, vol. 46, pp. 952-958, July, 1998.
- [55] J. -S. Hong and M. J. Lancaster, "Couplings of microstrip square open-loop resonators for cross-coupled planar microwave filters," *IEEE Trans. Microwave Theory Tech.*, vol. 44, pp. 2099-2119, November, 1996.
- [56] J. -S. Hong, M. J. Lancaster, D. Jedamzik, R. B. Greed, and J. C. Mage, "On the performance of HTS microstrip quasi-elliptic function filters for mobile communications application," *IEEE Trans. Microwave Theory Tech.*, vol. 48, pp. 1240-1246, July, 2000.
- [57] J. -S. Wong, "Microstrip tapped-line filter design," *IEEE Trans. Microwave Theory Tech.*, vol. 27, pp. 44-50, January, 1979.
- [58] J. T. Kuo, M. J. Maa, and P. H. Lu, "A microstrip elliptic function filter with compact miniaturized hairpin resonators," *IEEE Microwave and Guided Wave Lett.*, vol. 10, pp. 94-95, March, 2000.
- [59] J. -S. Hong and M. J. Lancaster, "Theory and experiment of novel microstrip slow-wave open-loop resonator filters," *IEEE Trans. Microwave Theory Tech.*, vol. 45, pp. 2358-2365, December, 1997.
- [60] J. P. Hsu, T. Anada, H. Tsubaki, Y. Migita, and K. Nagashima, "Synthesis of planar microwave band-pass filter based on foster-type network and normal mode expansion method," in *IEEE MTT-S Int. Microwave Symp. Dig.*, pp. 1199-1202, 1992.
- [61] F. R. Yang, K. P. Ma, Y. Qian, and T. Itoh, "A uniplanar compact photonic-bandgap (UC-PBG) structure and its applications for microwave circuits," *IEEE Trans. Microwave Theory Tech.*, vol. 47, pp. 1509-1514, August, 1999.
- [62] H. C. Bell, "Narrow bandstop filters," *IEEE Trans. Microwave Theory Tech.*, vol. 39, pp. 2188-2191, December, 1991.

- [63] G. Kumar and K. C. Gupta, "Broad-band microstrip antennas using additional resonators gap-coupled to the radiating edges," *IEEE Trans. Antenna Propagat.*, vol. 32, pp. 1375-1379, December, 1984.
- [64] R. Mongia, I. Bahl, and P. Bhartia, *RF and Microwave Coupled-Line Circuits*, Boston: Artech House, 1999.
- [65] R. Levy, "Filters with single transmission zeros at real or imaginary frequencies," *IEEE Trans. Microwave Theory Tech.*, vol. 24, pp. 172-181, April 1976.
- [66] K. T. Jokela, "Narrow-band stripline or microstrip filters with transmission zeros at real and imaginary frequencies," *IEEE Trans. Microwave Theory Tech.*, vol. 28, pp. 542-547, June 1980.
- [67] S. -Y. Lee and C. -M. Tsai "New cross-coupled filter design using improved hairpin resonators," *IEEE Trans. Microwave Theory Tech.*, vol. 48, pp. 2482-2490, December 2000.
- [68] C. -M. Tsai, S. -Y. Lee, and C. -C. Tsai, " Hairpin filters with tunable transmission zeros," in *IEEE MTT-S Int. Microwave Symp. Dig.*, pp. 2175-2178, 2001.
- [69] K. C. Gupta, R. Garg, I. Bahl, and P. Bhartia, *Microstrip Lines and Slotlines*, 2<sup>nd</sup> Boston: Artech House.
- [70] L. -H. Hsieh and K. Chang, "Dual-mode quasi-elliptic-function bandpass filters using ring resonators with enhanced-coupling tuning stubs," *IEEE Trans. Microwave Theory Tech.*, vol. 50, pp. 1340-1345, May 2002.
- [71] R. S. Kwok and J. F. Liang, "Characterization of high-Q resonators for microwave-filter applications," *IEEE Trans. Microwave Theory Tech.*, vol. 47, pp. 111-114, January 1999.
- [72] T.-Y. Yun and K. Chang, "A low loss time-delay phase shift controlled by piezoelectric transducer to perturb microstrip line," *IEEE Microwave and Guided Wave Lett.*, vol. 10, pp. 96-98, March 2000.

- [73] R. C. Buchanan, Editor, *Ceramic Material for Electronics*, New York: Marcel Dekker 1986.
- [74] T. -Y. Yun and K. Chang, "Analysis and optimization of a phase shifter controlled by a piezoelectric transducer," *IEEE Trans. Microwave Theory Tech.*, vol. 50, pp. 105-111, January 2002.
- [75] M. Matsuo, H. Yabuki and M. Makimoto, "Dual-mode stepped-impedance ring resonator for bandpass filter applications," *IEEE Trans. Microwave Theory Tech.*, vol. 49, pp. 1235-1240, July 2001.
- [76] J. S. Hong, M. Lancaster, D. Jedamzik and R. B. Greed, "On the development of superconducting microstrip filters for mobile communications applications," *IEEE Trans. Microwave Theory Tech.*, vol. 47, pp. 1656-1663, September 1999.
- [77] L. -H. Hsieh and K. Chang, "Slow-wave bandpass filters using ring or stepped-impedance hairpin resonators," *IEEE Trans. Microwave Theory Tech.*, vol. 50, pp. 1795 - 1800, July 2002.
- [78] D. K. Paul, P. Gardner and K. P. Tan, "Suppression of even modes in microstrip ring resonators," *Electron. Lett.*, vol. 30, pp. 1772-1774, October, 1994.
- [79] M. Kirschning, R. H. Jansen and N. H. L. Koster, "Measurement and computer-aided modeling of microstrip discontinuities by an improved resonator method," in *IEEE MTT-S Int. Microwave Symp. Dig.*, pp. 495-497, 1983.
- [80] E. Hammerstad, "Computer-aided design for microstrip couplers with accurate discontinuity models," *IEEE MTT-S Int. Microwave Symp. Dig.*, pp.54-56, 1981.
- [81] B. C. Wadell, *Transmission Line Design Handbook*, MA: Artech House, p. 321, 1991.
- [82] L. Zhu, H. Bu, and K. Wu, " Broadband and compact multi-pole microstrip bandpass filters using ground plane aperture technique, ", *IEE Proceedings, Microwaves, Antennas and Propagation*, vol. 149, pp. 71-77, February 2002.
- [83] J. -S. Park, J. -S. Yun and D. Ahn, " A design of the novel coupled-line bandpass filter using defected ground structure with wide stopband performance,

- ” *IEEE Trans. Microwave Theory Tech.*, vol. 50, pp. 2037- 2043, September 2002.
- [84] J. J. Yu, S. T. Chew, M. S. Leong and B. L. Ooi, “ New class of microstrip miniaturized filter using triangular stub,” *Electron. Lett.*, vol. 37, pp. 1169-1170, September 2001.
- [85] J. -R. Lee, J. -H. Cho, and S. -W. Yun, “ New compact bandpass filter using microstrip 1/4 resonators with open stub inverter,” *IEEE Wireless Compon. Lett.*, vol. 10, pp. 526 – 527, December 2000.
- [86] J. T. Kuo, M. J. Maa and P. H. Lu “A microstrip elliptic function filter with compact miniaturized hairpin resonator,” *IEEE Microwave and Guided Wave Lett.*, vol. 10, pp. 94-95, March 2000.
- [87] J. T. Kuo, M. J. Maa and P. H. Lu, “Microstrip elliptic function filters with compact miniaturized hairpin resonators,” in *Microwave Conference, 1999 Asia Pacific*, pp. 860-864, 1999.
- [88] A. Enokihara, K. Setsune, M. Sagawa, and M. Makimoto, “High-T/sub C/ bandpass filter using miniaturized microstrip hairpin resonator,” *Electron. Lett.*, vol. 28, pp. 1925-1927, September 1992.
- [89] I. Rumsey, M. Piket-May, and P. K. Kelly, “Photonic bandgap structure used as filters in microstrip circuits,” *IEEE Microwave and Guided Wave Lett.*, vol. 8, pp. 336-338, October 1998.
- [90] D. Ahn, J. S. Park, C. S. Kim, J. Kim, Y. Qian, and T. Itoh, “A design of the lowpass filter using the novel microstrip defected ground structure,” *IEEE Trans. Microwave Theory Tech.*, vol. 49, pp. 86-92, January 2001.
- [91] J. W. Sheen, “A compact semi-lumped low-pass filter for harmonics and spurious suppression,” *IEEE Microwave and Guided Wave Lett.*, vol. 10, pp. 92-93, March 2000.
- [92] L. -H. Hsieh and K. Chang, “Compact lowpass filter using stepped impedance hairpin resonator,” *Electron. Lett.*, vol. 37, pp. 899-900, July 2001.

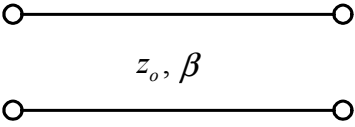
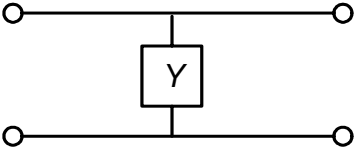
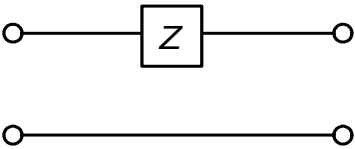
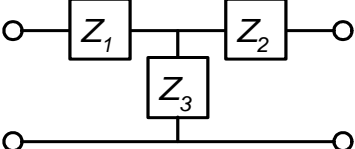
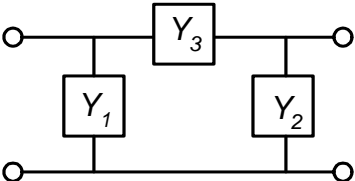


- [93] F. Giannini, M. Salerno and R. Sorrention, "Design of low-pass elliptic filters by means of cascaded microstrip rectangular elements," *IEEE Trans. Microwave Theory Tech.*, vol. 30, pp. 1348-1353, September 2000.
- [94] H. Yabuki, M. Sagawa, and M. Makimoto, "Voltage controlled push-push oscillators using miniaturized hairpin resonators," in *IEEE MTT-S Int. Microwave Symp. Dig.*, pp. 1175-1178, 1991.
- [95] P. R. Geffe, *Simplified Modern Filter Design*, New York: John F. Rider, 1963, Appendix 4.
- [96] G. Mazzarella, "CAD modeling of interdigitated structures," *IEEE Trans. Education*, vol. 42, pp. 81-87, February 1999.
- [97] A. M. Pavio and M. A. Smith, "A 20-40-GHz push –push dielectric resonator oscillator," *IEEE Trans. Microwave Theory Tech.*, vol. 33, pp. 1346-1349, December 1985.
- [98] J. Y. Lee and U. S. Hong, "Push-push subharmonically injection-locked oscillator," *Electron. Lett.*, vol. 32, pp. 1792-1793, September 1996.
- [99] F. X. Sinnesbichler, B. Hautz and G. R. Olbrich, "A Si/SiGe HBT dielectric resonator push-push oscillator at 58 GHz," *IEEE Microwave and Guided Wave Lett.*, vol. 10, pp. 145-147, April 2000.
- [100] N. Popovic, "Novel method of DRO frequency tuning with varactor diode," *Electron. Lett.*, vol. 26, p. 1162, July 1990.
- [101] Y. D. Lee, M. H. Lee, K. H. Lee, W. P. Hong and U. S. Hong, "Voltage-controlled hairpin resonator oscillator with new tuning mechanism," *Electron. Lett.*, vol. 36, pp. 1470-1471, August 2000.
- [102] J. H. Hwang, J. S. Cho, J. H. Kim, J. C. Lee, B. K. Kim, N. Y. Kim and U. S. Hong, "Effective structure of a push-push oscillator using a hairpin resonator for K-band application," in *IEEE MTT-S Int. Microwave Symp. Dig.*, pp. 452-455, 1999.

- [103] S. Qi, K. Wu and Z. Ou, "Hybrid integrated HEMT oscillator with a multiple-ring nonradiative dielectric (NRD) resonator feedback circuit," *IEEE Trans. Microwave Theory Tech.*, vol. 46, pp. 1552-1558, October 1998.
- [104] O. Ishihara, T. Mori, H. Sawano and M. Nakatani, "A highly stabilized GaAs FET oscillation using a dielectric resonator feedback circuit in 9-14 GHz," *IEEE Trans. Microwave Theory Tech.*, vol. 28, pp. 817-824, August 1980.
- [105] H. Yabuki, M. Sagawa, M. Matsuo, and M. Makimoto, "Stripline dual-mode ring resonators and their application to microwave devices," *IEEE Trans. Microwave Theory Tech.*, vol. 44, pp. 703-729, May 1996.
- [106] S. L. Lu and A. M. Ferendeci, "Varactor tuned ring resonator microwave oscillator," *Electron. Lett.*, vol. 32, pp. 46-47, January 1996.
- [107] M. Michael and D. K. Paul, "Microwave oscillators using ring resonators operating at higher modes," *Electron. Lett.*, vol. 34, pp. 1952-1953, October 1998.
- [108] T. -Y. Yun, K. Chang and R. S. Tahim, "A wideband voltage-tunable dielectric resonator oscillator controlled by a piezoelectric transducer," in *IEEE MTT-S Int. Microwave Symp. Dig.*, pp. 1435-1437, May 2001.
- [109] Y. M. Poplavko, Y. V. Prokopenko, V. I. Molchanov, and A. Dogan, "Frequency-tunable microwave dielectric resonator," *IEEE Trans. Microwave Theory Tech.*, vol. 49, pp. 1020-1026, June 2001.

## APPENDIX I

THE  $ABCD$  PARAMETERS FOR SOME USEFUL TWO-PORT CIRCUITS

Circuit	$ABCD$ parameters
 <p style="text-align: center;"><math>z_o, \beta</math></p>	$\begin{bmatrix} \cos \beta l & jz_o \sin \beta l \\ jy_o \sin \beta l & \cos \beta l \end{bmatrix}$
	$\begin{bmatrix} 1 & 0 \\ Y & 1 \end{bmatrix}$
	$\begin{bmatrix} 1 & Z \\ 0 & 1 \end{bmatrix}$
	$\begin{bmatrix} 1 + Z_1/Z_3 & Z_1 + Z_2 + Z_1 Z_2/Z_3 \\ 1/Z_3 & 1 + Z_2/Z_3 \end{bmatrix}$
	$\begin{bmatrix} 1 + Y_2/Y_3 & 1/Y_3 \\ Y_1 + Y_2 + Y_1 Y_2/Y_3 & 1 + Y_1/Y_3 \end{bmatrix}$

## APPENDIX II

## SOME USEFUL TWO-PORT NETWORK PARAMETER CONVERSIONS

$A$	$\frac{(1+S_{11})(1-S_{22})+S_{12}S_{21}}{2S_{21}}$	$Y_{11}$	$\frac{D}{B}$
$B$	$z_o \frac{(1+S_{11})(1+S_{22})-S_{12}S_{21}}{2S_{21}}$	$Y_{12}$	$\frac{BC-AD}{B}$
$C$	$\frac{(1-S_{11})(1-S_{22})-S_{12}S_{21}}{2z_o S_{21}}$	$Y_{21}$	$\frac{-1}{B}$
$D$	$\frac{(1-S_{11})(1+S_{22})+S_{12}S_{21}}{2S_{21}}$	$Y_{22}$	$\frac{A}{B}$
$S_{11}$	$\frac{A+B/z_o-Cz_o-D}{A+B/z_o+Cz_o+D}$	$Z_{11}$	$\frac{A}{C}$
$S_{12}$	$\frac{2(AD-BC)}{A+B/z_o+Cz_o+D}$	$Z_{12}$	$\frac{AD-BC}{C}$
$S_{21}$	$\frac{2}{A+B/z_o+Cz_o+D}$	$Z_{21}$	$\frac{1}{C}$
$S_{22}$	$\frac{-A+B/z_o-Cz_o+D}{A+B/z_o+Cz_o+D}$	$Z_{22}$	$\frac{D}{C}$

## VITA

Lung-Hwa Hsieh received his B.S. degree from Chung Yuan Christian University, Chungli, Taiwan in 1991, the M.S. degree from National Taiwan University of Science and Technology, Taipei, Taiwan in 1993 and his Ph.D. degree in electrical engineering from Texas A&M University in College Station, Texas.

From 1995 to 1998, he was a senior design engineer at General Instrument in Taipei, Taiwan and involved in RF video and audio circuit design. Since 2000, he has been a Research Assistant in the Department of Electrical Engineering at Texas A&M University in College Station. His research interests include microwave passive and active integrated circuits and devices. His current address is: 7411 Desert Eagle Rd. NE, Albuquerque NM 87113.